

**TECHNISCHE UNIVERSITÄT DRESDEN**

FACULTY OF COMPUTER SCIENCE  
INSTITUTE OF SOFTWARE AND MULTIMEDIA TECHNOLOGY  
CHAIR OF COMPUTER GRAPHICS AND VISUALIZATION  
PROF. DR. STEFAN GUMHOLD

**Master's Thesis**

for the acquisition of the academic degree  
Master of Science

**Development and Evaluation of an Amira Plug-In for  
Image Fusion of intraoperative Thermography with  
MRI in Neurosurgery**

Florian Weidner  
(Born November 5th, 1986 in Marktheidenfeld, Mat.-No.: 3573948)

Tutor: M.Sc. Peter Urban  
Tutor: Dipl.-Inf. Nico Hoffmann

Dresden, 4th of December, 2014



---

## Aufgabenstellung

**Motivation** Die Thermografie ist eine Technik, welche die von Körpern emittierte Wärmestrahlung örtlich aufgelöst sichtbar macht und deren zeitlichen Verlauf als auswertbare Sequenz von Wärmebildern zur Verfügung stellt. Jedes Element dieser Sequenz besteht aus einer Pixel-Matrix, bestehend aus gemessenen Temperaturen. Die Intensität sowie die zeitliche Variation der emittierten Wärmestrahlung hängen u.a. von der Gewebeart, Änderungen im kortikalen Blutfluss, neuronaler Aktivität wie auch genereller Hintergrundaktivität ab. Im intraoperativen neurochirurgischen Einsatz stellt die zeitaufgelöste Thermografie einen neuartigen Ansatz zur Identifikation und Abgrenzung kortikaler Pathologien dar, die auf perfusionsbedingten Störungen beruhen. Beispielsweise führt der veränderte Metabolismus von tumorösem Gewebe zu einer charakteristischen Wärmesignatur, welche eine Abgrenzung zu regelrechtem Gewebe möglich macht.

**Zielstellung** In dieser Arbeit soll eine Software entwickelt werden, die eine intraoperative dreidimensionale Darstellung des thermografisch abgebildeten trepanierten Kortex‘ ermöglicht. Hierzu wird ausgenutzt, dass im Rahmen von navigationsgestützten neurochirurgischen Eingriffen kalibrierte Objekte hinsichtlich ihrer Lage zu einem a priori registrierten Patientendatensatz (MRT) erfasst werden können. Insbesondere ermöglicht dies im Falle einer kalibrierten Wärmebildkamera die Erfassung deren Lage bezüglich des Patientendatensatzes. Vor dem intraoperativen Einsatz soll ein physikalisches Phantom erstellt werden, welches sowohl in der MRT-Bildgebung als auch in der Thermografie markante Charakteristika aufweist. Mit diesem Phantom soll die Registrationsgenauigkeit untersucht sowie mögliche Einflussgrößen analysiert werden. Im Anschluss erfolgt die Anwendung der Methode im Rahmen von neurochirurgischen Eingriffen. Hier sollen nun die aufgezeichneten Wärmebilder auf die Oberfläche dieses Datensatzes projiziert werden. Weiterhin soll die thermografisch abgebildete Oberfläche des Kortex‘ anhand des Patientendatensatzes dreidimensional dargestellt werden. Dadurch kann eine nachfolgende Untersuchung der Abhängigkeit der Signalgüte der erfassten Wärmebilder stattfinden.

### Schwerpunkte

1. Recherche und Bewertung von Verfahren zur Registration multimodaler Aufnahmen.
2. Entwicklung eines physikalischen Phantoms für die MRT- sowie Wärmebildgebung.
3. Intraoperative Registrierung und Projektion von Wärmebildern auf den entsprechenden Patientendatensatz (MRT).
4. Evaluation der Registrationsgenauigkeit



---

## **Statement of Authorship**

I hereby declare that the thesis, submitted today to the examination office of the Faculty of Computer Science, with the title:

*Development and Evaluation of an Amira Plug-In for Image Fusion of intraoperative Thermography  
with MRI in Neurosurgery*

has been composed solely by myself and describes my own work. I confirm that all aids and information which have been directly or indirectly taken from other sources have been marked as such.

Dresden, 4th of December, 2014

Florian Weidner



---

## Kurzfassung

**Hintergrund:** Die multimodale medizinische Bildfusion kombiniert die Informationen von einem oder mehreren Bildern um ihren diagnostischen Wert zu erhöhen. Bisherige Anwendungen fusionieren nur Bilder die mittels Computertomografie, Ultraschall, Einzelphotonentomografie und Magnetresonanztomografie (MRT) gewonnen werden, nicht aber durch Thermografie. **Methoden:** Diese Arbeit präsentiert eine Anwendung welche die Bildfusion von intraoperativen Thermographiebildern und einem präoperativen MRT-Bild ermöglicht. Dazu verbindet sich die Anwendung mit einem Neuronavigationssystem und einer Thermografiekamera. Ein kalibrierungsbasierter Registrierungsalgorithmus und ein Algorithmus zum Bildupdate verarbeiten die eingehenden Datenströme. Zu Testzwecken und für eine abschließende Evaluation wurde ein physikalisches Phantom entwickelt. Dieses besitzt sichtbare Merkmale in MRT, Thermografie und Weißlichtbildung. Es erlaubt die Simulation von Brain Shift, Perfusion und einer Trepanation. **Ergebnisse:** Die Evaluation mit dem Phantom ergab einen durchschnittlichen Fehler von 2,46 mm. Der gemessene maximale Fehler beträgt 10,06 mm. Die identifizierten Hauptfehlerquellen sind die Kalibrierungsparameter und die verwendete Hardware.

## Abstract

**Background:** Multimodal medical image fusion combines information of one or more images in order to improve the diagnostic value. Previous applications fuse mainly images of computed tomography, magnetic resonance imaging (MRI), ultra-sonic and single-photon emission computed tomography and not thermography. **Methods:** This thesis presents a set of tools to perform image fusion of intraoperative infrared images with a preoperative 3D MR image. To do this, the application connects to a neuronavigation system and an infrared camera. The neuronavigation system tracks the position of the infrared camera. A calibration-based image registration algorithm and an image update algorithm process the incoming data streams. To evaluate and test the application an imaging phantom is developed. The phantom has visible features in MRI, white-light imaging and thermography. It allows simulation of perfusion, brain shift and trepanation. **Results:** The developed application performs image fusion with a mean error of 2.46 mm and a maximum error of 10.06 mm. Main cause of error are the determination of the calibration parameters and hardware components.



---

Resistance is futile.

—THE BORG (Stardate 43989.1)



# Contents

|          |   |           |
|----------|---|-----------|
| <b>1</b> | <b>Introduction</b>                                 | <b>3</b>  |
| <b>2</b> | <b>Background Information</b>                       | <b>5</b>  |
| 2.1      | Medical Imaging . . . . .                           | 5         |
| 2.1.1    | Magnetic Resonance Imaging (MRI) . . . . .          | 5         |
| 2.1.2    | Thermographic Imaging (TI) . . . . .                | 7         |
| 2.2      | Brain Shift . . . . .                               | 9         |
| 2.3      | Hardware . . . . .                                  | 9         |
| 2.3.1    | Neuronavigation System . . . . .                    | 9         |
| 2.3.2    | Thermographic Camera . . . . .                      | 11        |
| 2.4      | Software . . . . .                                  | 12        |
| 2.4.1    | Amira . . . . .                                     | 12        |
| 2.4.2    | BrainLab . . . . .                                  | 13        |
| 2.4.3    | OpenIGTLINK . . . . .                               | 14        |
| <b>3</b> | <b>Related Work</b>                                 | <b>15</b> |
| 3.1      | Phantom Development . . . . .                       | 15        |
| 3.2      | Image Processing . . . . .                          | 17        |
| 3.2.1    | Features and Feature Extraction . . . . .           | 18        |
| 3.2.1.1  | Intensity-Based Features . . . . .                  | 18        |
| 3.2.1.2  | Shape-Based Features . . . . .                      | 20        |
| 3.2.2    | Image Registration . . . . .                        | 23        |
| 3.2.2.1  | Taxonomy . . . . .                                  | 23        |
| 3.2.2.2  | Feature-Based Image Registration . . . . .          | 26        |
| 3.2.2.3  | Calibration-Based Image Registration . . . . .      | 29        |
| 3.2.3    | Image Fusion . . . . .                              | 32        |
| 3.3      | Examples of Multimodal 2D/3D Image Fusion . . . . . | 36        |
| 3.4      | Assessment of Registration Techniques . . . . .     | 39        |

|   |            |
|---|------------|
| <b>4 Design and Implementation</b>                                  | <b>43</b>  |
| 4.1 Phantom Development . . . . .                                   | 43         |
| 4.2 Amira Plug-In Development . . . . .                             | 47         |
| 4.2.1 Architecture and Connection . . . . .                         | 48         |
| 4.2.2 Image Registration . . . . .                                  | 53         |
| 4.2.3 Image Update . . . . .  | 59         |
| 4.2.4 Image Fusion . . . . .  | 61         |
| 4.2.5 Additional Functionality . . . . .                            | 65         |
| 4.2.5.1 Record and Replay . . . . .                                 | 65         |
| 4.2.5.2 Pointer Tracking . . . . .                                  | 66         |
| 4.2.5.3 Camera Configuration . . . . .                              | 66         |
| 4.2.5.4 Heightmap . . . . .   | 67         |
| 4.2.6 User Interface . . . . .                                      | 69         |
| 4.3 Scenario for Intraoperative Application of the System . . . . . | 72         |
| <b>5 Evaluation</b>   | <b>77</b>  |
| <b>6 Summary</b>  | <b>87</b>  |
| <b>7 Future Work</b>  | <b>89</b>  |
| 7.1 Phantom . . . . .   | 89         |
| 7.2 Image Processing . . . . .                                      | 89         |
| <b>8 Appendix</b>   | <b>91</b>  |
| <b>Bibliography</b>   | <b>97</b>  |
| <b>List of Figures</b>  | <b>105</b> |
| <b>List of Tables</b>   | <b>109</b> |

# 1 Introduction

“The worldwide cancer incidence of a malignant brain tumour is 3.4 per 100,000 people (men: 3.9 per 100,000, women: 3.0 per 100,000). In 2012, there were a total of 256,213 affected worldwide (139,608 men and 116,605 women). The trend of new cases is rising. In 2002, there were 189,582 sufferers worldwide.”<sup>1</sup>

Radiation therapy, chemotherapy, observation, surgery and their combinations are possible treatments for these patients ([UK14]). During treatment, it is important to remove all cancer cells to prevent the tumour from spreading again. If medical personnel fails to remove some cancer cells, the tumour will reappear. For example, a neurosurgeon has to differentiate between healthy and pathological tissue in order to extirpate as much of the tumour as possible. However, this differentiation is not easy because the tumour has no clear margins but infiltrates the surrounding tissue. In addition, the surgeon must not remove too much tissue. If this happens, the patient’s outcome may be affected negatively. As mentioned before, it is nearly impossible for the human eye to differentiate between tumour and healthy tissue. Advanced techniques in medical imaging can help to facilitate a complete resection of tumour tissue. Intraoperative magnetic resonance imaging (MRI) is the best way to provide information about the tumour [KYY<sup>+</sup>09]. However, these facilities are very bulky and expensive. They require larger operating rooms and additional time for image acquisition.

A promising alternative is *Thermographic Imaging* (TI) or *Thermography*. TI is “...non-invasive, non-ionizing, risk-free, patient-friendly, and cost is considerably low.” [RA12]. It measures intensity of infrared light emitted by a body which correlates with the temperature of the body’s surface. This correlation is defined by the Stefan-Boltzmann law (see [Ste79] and [Bol84]). During neurosurgery, a thermographic camera can acquire infrared images of the patient’s brain. They can help to differentiate between healthy and tumour tissue because “... the cortex overlying the tumor [is] either colder or warmer than the surrounding cortex” [GHKO04]. In addition, TI is a promising non-invasive technique to analyse “...neuronal activity related heat transfers” [HHS<sup>+</sup>14]. This is called *functional Thermography* (fTI) and was first used by Okudera et al. [OKT94] in 1994. The acquired information could provide additional

---

<sup>1</sup><http://www.hirntumorhilfe.org/hirntumor/statistiken/zahlen-weltweit/>,  
last accessed: 2014-11-19

diagnostic information to medical personnel [GHK<sup>+</sup>03].

Because TI operates in a different spectrum than human visual perception, additional mental effort is necessary to relate measured temperature distributions to the observed area. A preoperative acquired 3D magnetic resonance image of the brain, also called 3D MR model, might help to solve this problem. A software can project the thermographic image onto the 3D image and ease data analysis. To provide this enriched visualization, *Image Fusion* is necessary. Image fusion is the process of merging information of two or more images. In the described case, the result is a 3D MR model of the brain enriched with temperature information. The thermographic image is mapped to the very place where it has been measured at the real subject. To do this, *Image Registration* is necessary. Image registration is the process of aligning the 3D model and the infrared image so that structures like vessels and gyri overlay perfectly. However, the preoperative 3D model does not represent the shape of the brain during surgery. This is because of intraoperative brain deformation, called *Brain Shift*. According to Hill et al. [HMM<sup>+</sup>98], is “... intraoperative brain deformation [...] an important source of error that needs to be considered”. Brain shift invalidates preoperative 3D models. An invalid model leads to an incorrect projection and an invalid projection provides invalid information to neurosurgeons. Brain shift and other inaccuracies like errors in image registration make it necessary to evaluate the resulting image with respect to accuracy. An imaging phantom supports evaluation of accuracy. Imaging phantoms are objects which have visible and measurable features in all necessary imaging modalities. In our case, MRI and TI. With these features, repeatable and consistent measurements and with it an evaluation and testing of image registration and image fusion is possible.

In this thesis, a complete set of tools to fuse an intraoperatively acquired stream of thermographic images of the brain with a preoperatively acquired 3D MR image of the brain is presented. For this, the software solution performs a calibration-based image registration with the help of a neuronavigation system. All algorithms are developed for Amira, a commercially available software for visualization of medical data. The accuracy of the application is evaluated with an especially developed imaging phantom. The objective is to provide a software which supports medical personnel during surgeries and analysis of intraoperative thermographic images of the brain.

This thesis is organized as follows: Chapter 2 provides background information about medical imaging techniques, brain shift and involved soft- and hardware. In chapter 3, related work concerning phantom development and image processing is elaborated. After this introductory part, design and implementation of the phantom as well as the image processing algorithms are described (chapter 4). Chapter 5 is devoted to the evaluation of the application. This thesis finishes with a summary (chapter 6) and an outlook (chapter 7).

## 2 Background Information

This chapter begins with the description of important medical imaging techniques. Namely, MRI and TI because the images used by the presented application are acquired with these techniques. Then, a short overview about involved soft- and hardware is provided. First, the infrared camera used for image acquisition and the neuronavigation system are presented. Second, Amira as well as OpenIGTLINK are described in detail because the here presented software is an extension for Amira and uses OpenIGTLINK for communication between hardware components.

### 2.1 Medical Imaging

Medical Imaging refers to a set of techniques which visualize visible and hidden structures and processes of the human body. The goal of all medical imaging techniques is to support medical personnel during examination of patients and treatment of medical conditions. Due to the fact that there exist a lot of different techniques, the following sections only describe the ones which are directly related to the topic:

- Magnetic Resonance Imaging (MRI)
- Thermographic Imaging (TI)

The following sections outline core concepts of these techniques as well as common application domains. Furthermore, the techniques are shortly evaluated in order to provide a distinction between them.

#### 2.1.1 Magnetic Resonance Imaging (MRI)

Magnetic Resonance Imaging utilizes the spin of the nucleus. To understand nuclear spin, it is necessary to know that the nucleus of an atom consists of protons and neutrons. Protons have an electrical charge of plus one. Neutrons do not have an electrical charge. The nuclear spin depends on the number of protons and neutrons, the so-called atomic weight. Each atom with a spin behaves like a tiny magnet, meaning that it adjusts its orientation along the lines of a magnetic field (see figure 2.1).

The chemical element protium, an isotope of hydrogen, has a spin. This is important, because a human body contains a lot of water molecules and with it protium. Therefore, a lot of atoms in the human body

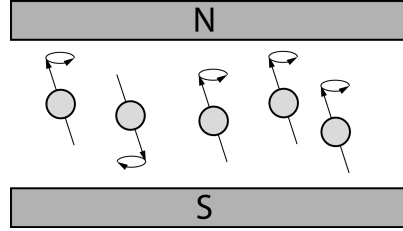


Figure 2.1: Illustration of the nuclear spin showing protons aligned parallel and anti-parallel to a magnetic field

have a spin. In fact, it is the “most abundant atom in the human body” [Ec12].

When an MRI image is taken, a strong magnetic field is applied. As mentioned before, atoms with a spin align along these field lines. This process is comparable to the movement of a compass needle. Right after the magnetic field is applied, the atoms start precessing with the *Larmor frequency*. This movement is called *Larmor precession*. It is comparable to the movement of a toy top. In this state, protons do not produce any measurable signal because of absence of a longitudinal movement. Because of this, another short magnetic impulse is applied. This impulse deflects the axis by an angle of  $90^\circ$ . After the tilting impulse, the atoms return to their original position. Here, two parameters, the  $T_1$  and  $T_2$  relaxation times, are very important.

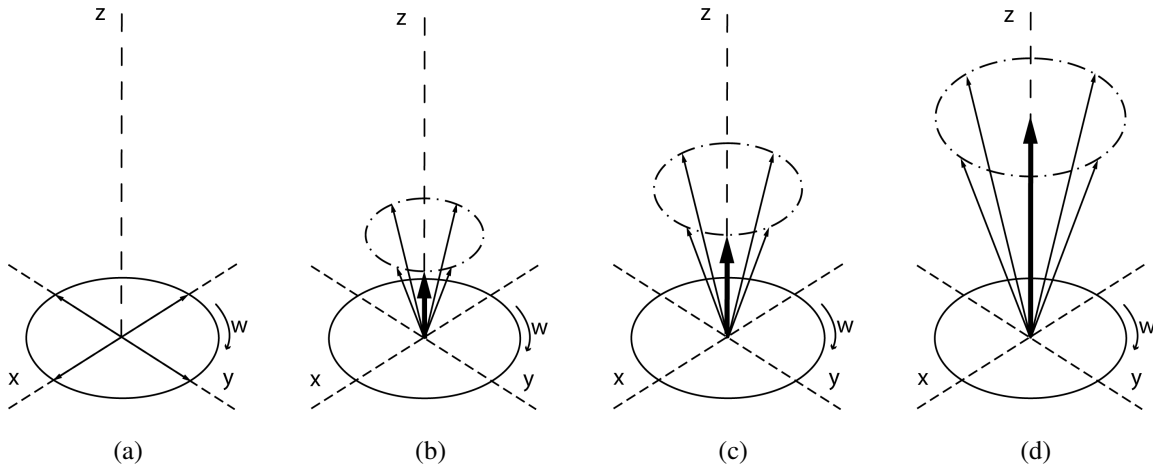


Figure 2.2: Illustration of the spin-lattice relaxation. 2.2a: Spin after the tilting impulse. 2.2b, 2.2c and 2.2d: magnetization in the original state

Spin-lattice relaxation refers to the time  $T_1$  protons need to return to their original longitudinal magnetization (see figure 2.2). Spin-spin relaxation time  $T_2$  is the time in which the protons lose 63% of their coherence in movement and their transversal magnetization (see figure 2.3). Different physical materials have different relaxation times. Different relaxation times lead to different signal strengths. A single measurement results in one image which shows one layer of the measured object. This image is called

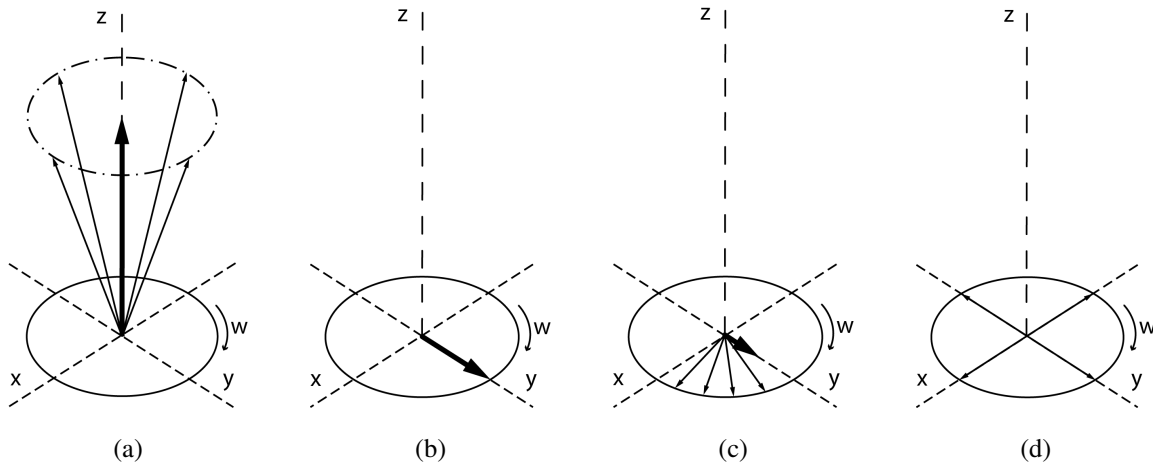


Figure 2.3: Illustration of the spin-spin relaxation. 2.3a: Spin before the tilting impulse. 2.3b: spin after the tilting impulse. 2.3c: de-phasing 2.3d: re-phased spin

a slice. To get a 3D image, several slices are necessary. In order to get all slices with one measurement, the strength of the applied magnetic fields is spatially dependent. With this spatial dependent magnetic fields, the resulting signal is encoded. Decoding results in a uniform 3D scalar grid with values representing the signal. This grid contains a lot of information, however they are not visible to the human eye. An inverse Fourier transformation is necessary to transform data from frequency space to time or MR image space.

Images obtained via MRI show internal organs and soft tissue very clear. It is very suited for brain imaging. Hard bones do not give an MR signal. The technique is non-invasive and radiation free. However, compared to other techniques like a computed tomography, it is more expensive. Nevertheless, no harm is done to the body of the patient because no dangerous or harmful radiation is emitted by the tomograph. MRI will not be applicable, if the patient has metallic objects like pacemakers or prostheses which can not be removed. These objects are attracted and heated by the magnetic fields and might hurt the patient during the imaging.

### 2.1.2 Thermographic Imaging (TI)

Thermographic imaging is similar to conventional imaging with a custom camera. However, the sensor array measures light of a different spectrum. Infrared radiation is located between the visible light and microwaves. Infrared light can be divided further into near IR, short-wavelength IR, mid-wavelength IR, long-wavelength IR and far IR according to the wavelength. Figure 2.4 depicts the spectrum and the single types of IR light.

Contrary to MRI, TI visualizes only the surface of an object. Radiation impinges on the imaging sensor

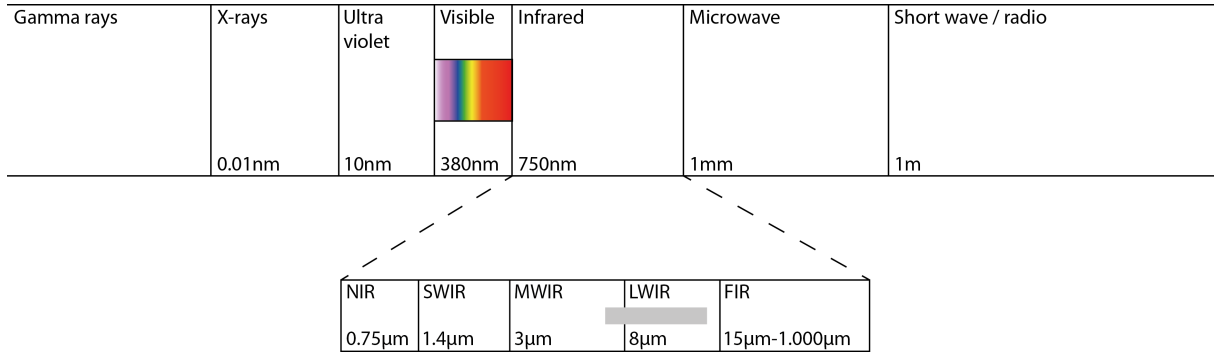


Figure 2.4: Electromagnetic spectrum with outlined infrared spectra

and is transformed into a signal. For example, an electrical current or a change in an electrical resistor (which results in the change of an electrical current). For each pixel of the resulting image, a separate sensor is necessary. These sensors form a sensor array. Incoming radiation stimulates these sensors on the sensor array. The resulting signals are spatially encoded. Decoding leads to a two-dimensional image which represents the measured infrared radiation of all objects in observed space.

Today's cameras have a high spatial and temporal resolution up to 30 mK and 50 HZ ([HSH<sup>+</sup>14]). The measured values are related to the metabolism of the brain. This is because the “IR radiation emitted by the head and cortex is influenced by vasodilatation, hyperthermia, hyperperfusion, hypermetabolism and hypervasculartization” [RA12]. TI can be active or passive. When applying active thermography, an external energy source is used to change the temperature of the subject. Passive thermography measures the natural temperature without an external influence. Variations of conventional TI are “Digital Subtraction Thermography (DSA) and sequential thermography” [RA12]. It is possible to apply a “Human thermal model[s] in order to eliminate varying thermal environmental conditions” like air conditioning, flushings during surgery, fluid films as a result of flushings or breathing of the neurosurgeon [RA12] to improve the result.

TI is non-invasive. The patient is not exposed to any additional energy. It can support medical personnel distinguishing between different tissues and making assertions about the brain's activity. However, as mentioned before, it can be hard to correlate the resulting image with the observed body without additional information.

Besides the two mentioned imaging techniques, many others exist. Techniques like computed tomography (CT, [Hsi09]), single-photon emission computed tomography (SPECT, [FSTL05]), ultrasound imaging ([SSS14]), optical coherence tomography (OCT, [DF08]), optical imaging ([IBH11]) and others help medical personnel to treat the patient as good as possible. MRI and TI, are important for the following chapters. The initial 3D model is acquired via MRI and fused with the 2D thermographic image.

## 2.2 Brain Shift

Brain shift describes the brain's deformation after performing a trepanation or extirpating tissue. This deformation invalidates the preoperative acquired 3D image of the brain. Brain shift is caused by a variety of factors. Dumpuri et al. [DTSM06] mention surgical manipulation, gravitational forces and pharmacological responses. Besides that, mechanical tissue properties, loss of brain-spinal fluid, anatomical constraints, intracranial pressure and patient variability are, according to Valencia et al. [VBO12], factors which can cause Brain shift. Furthermore, Bucholz et al. [BYTM97] mention tumour resection, hyperventilation, edema and haemorrhage as additional influencing factors. Even more factors are mentioned by Reinges and colleagues [RNK<sup>+</sup>04]. They add brain swelling and a debunking of the tumour with re-expansion of the formerly compressed brain and the conventional mechanical ventilation.

Brain shift is a non-linear phenomenon, meaning that different parts of the brain deform with different velocities in different directions. According to Reinges et al. [RNK<sup>+</sup>04], "...studies analysed intraoperative brain shift and reported a mean displacement of up to 1 cm". Dorward et al. [DAV<sup>+</sup>98] found a mean shift of the cortex after dura mater opening of 4.6 mm and at completion of the surgical procedure of 6.7 mm".

Brain shift is a crucial problem in brain imaging. The preoperative acquired images of the brain, regardless whether CT or MR images, do not represent the deformed brain. The presented imaging phantom is able to simulate brain shift. It helps with evaluation of the image fusion applications and allows testing of the influence of brain shift during medical imaging.

## 2.3 Hardware

The following section outlines the hardware components used during this work. The neuronavigation system, the thermographic camera and other important components. Please note that our application is not limited to those components but will work with every other thermographic camera and navigation system which implement the transmission protocol.

### 2.3.1 Neuronavigation System

Neuronavigation systems are used during image-guided surgery to provide medical personnel with additional medical images and data. They consist of two essential parts: First, a tracking device (fig. 2.5) consisting of a stereo camera, a display and a computer. Second, objects which are recognized by the stereo cameras. For example, fiducial markers glued to the patient's skull as shown in figure 2.8 or small

silver spheres attached to instruments (see fig. 2.6 and 2.7). A neuronavigation system works with image data acquired preoperatively. For example, MR or CT images. It visualizes images depending on the position and orientation of these markers. The neuronavigation system used for the presented algorithm and software is a BrainLab VectorVision<sup>1</sup>. Imagine a patient with a brain tumour. The patient arrives at



Figure 2.5: Neuronavigation system *BrainLab VectorVision* showing the computer, the view screen and the infrared cameras

the hospital and needs surgery. A preoperative MR is acquired. Here, several fiducial markers are placed on the head of the patient which are then visible in the 3D MR image. Those markers stay on the head of the patient until he is in the operating room. After the patient is prepared for surgery, the neurosurgeon registers the patient's head to the acquired MR model with the help of the neuronavigation system. To do this, the surgeon touches each physical marker with a pointing device (see fig. 2.6) slightly. The neuronavigation system calculates the position of the markers through the position and direction of the pointing device and relates it to the markers in the MR model. After a successful registration process, the neurosurgeon has the possibility to point with the pointing device at any position of the patients head or brain. The neuronavigation system shows the corresponding view of the MR model according to the position and direction of the pointing device. Besides the mentioned application, many more use cases for neuronavigation systems exist but tracking is the most important for this work.

For the presented work, not only the patients head and the pointing device are tracked, but also the infrared camera. For this, special superstructures are available which have an individual and unambiguous

<sup>1</sup>[www.brainlab.com](http://www.brainlab.com), last accessed: 2014-10-02

marker set-up. The presented application uses the instrument adapter (IA) shown in figure 2.7. This adapter is attached to the thermographic camera. A marker set-up is detected by the neuronavigation system which offers the orientation and position via an interface. Summarizing, the total set-up consists of the following components: The neuronavigation system, fiducial markers which are attached to the skull of the patient, the IA which is attached to the thermographic camera and a pointer.

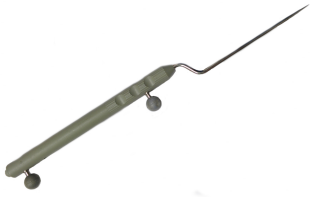


Figure 2.6: Pointer



Figure 2.7: Instrument adapter



Figure 2.8: Fiducial marker

### 2.3.2 Thermographic Camera

The thermographic camera used during the presented work is the InfraTec<sup>2</sup> *VarioCAM HD head 680 S / 30mm \*\*\*MEDICAL \*\*\** (see figure 2.9). The detector is an uncooled micro-bolometer focal plane array with a resolution of  $640 \times 480$  pixels. When using the default lens, it has a field of view (FOV) of  $29.9^\circ \times 22.6^\circ$  and a focal length of 30 mm. The focus plane is adjustable through a stepping motor. Its position correlates with a focus value. This focus value is provided to developers via an interface. The spatial resolution is 0.42 mm when using an object distance of 0.5 m and the temperature resolution is 0.03 K when measuring 30°C.

Figure 2.9: InfraTec *VarioCAM HD head 680 S / 30mm \*\*\*MEDICAL \*\*\**

In the clinical set-up, the camera is attached to a portable stand. Furthermore, the mentioned IA is attached to the camera in order to enable tracking via the neuronavigation system. The complete set-up is shown in figure 2.10

<sup>2</sup>[www.infratec.de](http://www.infratec.de), last accessed: 2014-10-02

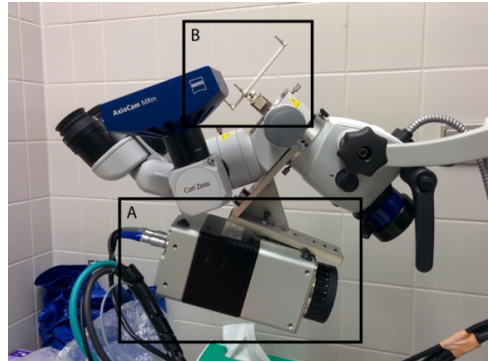


Figure 2.10: Thermographic camera (A) with the attached IA (B)

## 2.4 Software

During implementation of the presented work, several open source and commercial frameworks were used. The following section outlines especially *Amira* and *OpenIGTLINK* because they are core components of the presented application. Furthermore, *BrainLab VectorVision 2.1.1 cranial* and *BrainLab iPlanNet 3.0* are mentioned briefly because they play an important role during image registration.

### 2.4.1 Amira

Amira<sup>3</sup> is a software for scientific visualization in the medical field. According to the manufacturer, it “is a powerful, multifaceted 3D software platform for visualizing, manipulating, and understanding data from computed tomography, microscopy, MRI, and many other imaging modalities”. It is based on Qt<sup>4</sup>, OpenInventor<sup>5</sup> and OpenGL<sup>6</sup>. A developer option allows it to extend the functionality.

Figure 2.11 shows the user interface of Amira. It is divided into three main areas. The upper left area shows the *pool*. It contains *modules*. Below the pool, properties of the selected module are presented. On the right side, a viewer shows images. A console window in the lower right corner presents textural information to the user.

The main data object of Amira are so-called meshes. Meshes are located in the pool. A mesh consists of connected modules. A module is an atomic unit of a mesh and represents one of the following three units: input data (green), output data (yellow) or a processing element (red). These modules can be connected via so-called ports. A connection between two ports is represented by a black line. Each module can have several input ports and output ports. Input ports consume data. Output ports provide data and

<sup>3</sup>[www.vsg3d.com/amira/](http://www.vsg3d.com/amira/), last accessed: 2014-10-02

<sup>4</sup>[www.qt-project.org/](http://www.qt-project.org/), last accessed: 2014-10-20

<sup>5</sup>[www.vsg3d.com/open-inventor/](http://www.vsg3d.com/open-inventor/), last accessed: 2014-10-20

<sup>6</sup>[www.opengl.org/](http://www.opengl.org/), last accessed: 2014-10-02

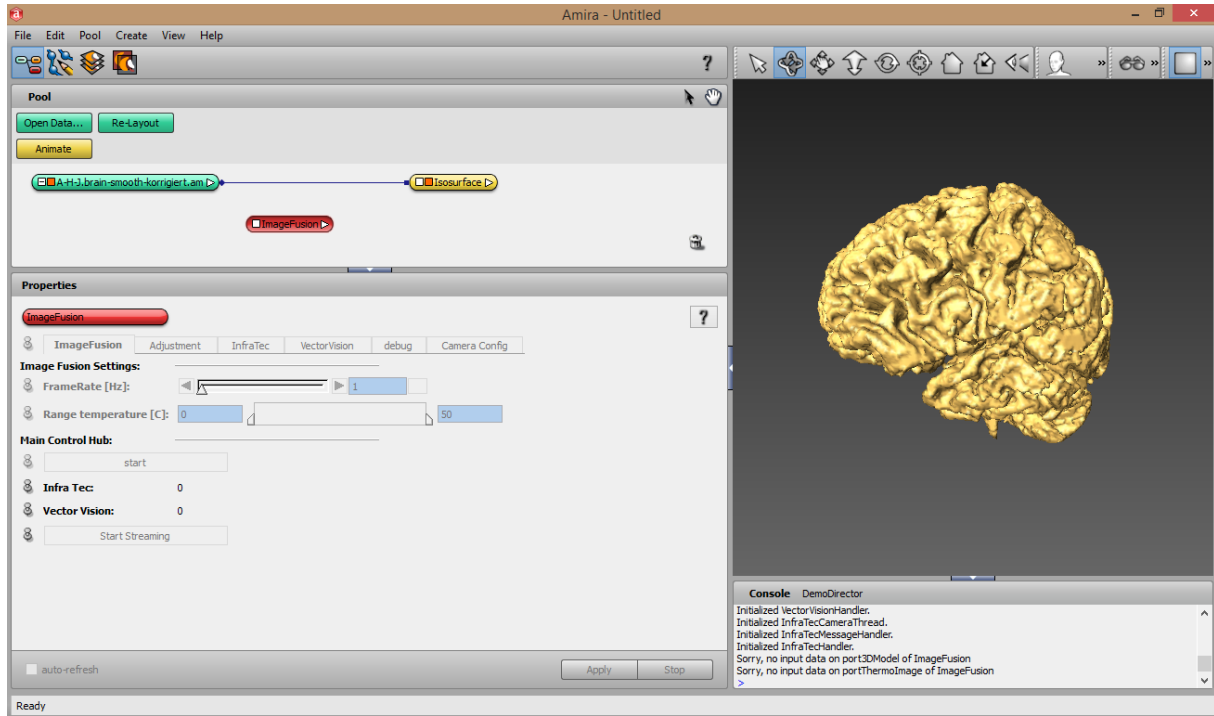


Figure 2.11: Screenshot of the Amira user interface showing a mesh with three modules and one connection

are so-called downstream ports. When the data on a downstream port changes, Amira provides the possibility to update all modules which work with this data. For displaying data, Amira provides several possibilities like *Isosurfaces*, *Vortex*, *Volren*, *SurfaceView* and others. Besides that, Amira provides basic image processing modules. Most important for our work is the *BrainSegmentation* module, developed by Wagner et al. [WKM<sup>+</sup>09]. It segments the brain from a MR image of the patient or subject respectively.

The here presented algorithms are encapsulated in an Amira module called *Image Fusion*. The module is connected with the existing modules *Isosurface* and *SurfaceView* and work with data provided by *BrainSegmentation*. Together, they are responsible for image fusion.

## 2.4.2 BrainLab

The image fusion uses a neuronavigation system from BrainLab and associated software. Namely, BrainLab iPlanNet 3.0<sup>7</sup> and BrainLab VectorVision 2.1.1 cranial<sup>8</sup>.

*VectorVision iPlanNet 3.0 cranial* is a planning tool for surgeries. Before acquiring the MR image,

<sup>7</sup>[www.brainlab.com/radiosurgery-products/iplan-rt-treatment-planning-software/](http://www.brainlab.com/radiosurgery-products/iplan-rt-treatment-planning-software/),

last accessed: 2014-10-02

<sup>8</sup>[www.brainlab.com/surgery-products/overview-neurosurgery-products/cranial-navigation-application/](http://www.brainlab.com/surgery-products/overview-neurosurgery-products/cranial-navigation-application/), last accessed: 2014-10-02

fiducial markers are glued onto the subject. In order to perform a correct registration of the subject to the neuronavigation system, the position of these fiducial markers has to be defined. This is performed manually by medical personnel. For this, the dataset of the MR image has to be imported into this software. Then, the user searches the fiducial markers in the image and marks them. After every marker has been marked, the registration is possible.

*VectorVision 2.1.1 cranial* is a visualization software used by medical personnel during surgeries to explore and navigate through preoperative data. The software is able to show data acquired preoperatively and allows surgeons to register the subject to the neuronavigation system. For example, they can use a pointing device (shown in figure 2.6) to tip on any location of the patients head. VectorVision cranial updates the view of the preoperative acquired image according to the position and direction of the pointing device and shows the touched part of the brain. Furthermore, it is able to send the acquired tracking data to other clients which is why it is mentioned here. The presented application connects to VectorVision 2.1.1. cranial via OpenIGTLink which is described in the next section.

### 2.4.3 OpenIGTLink

OpenIGTLink<sup>9</sup> is a framework which “...provides a standardized mechanism for communication among computers and devices in operating rooms and other medical purposes for wide variety of image-guided therapy (IGT) applications.” It supports the socket-based streaming of tracking data as well as image data. For this, it provides means for data transfer as well as message types. It is extensible, meaning that own message types can be implemented. With the provided software development kit, communication between the neuronavigation system and Amira as well as communication between the thermographic camera and Amira is realized. It is important to know, that VectorVision cranial provides an interface for connecting to OpenIGTLink.

---

<sup>9</sup>[www.openigtlink.org](http://www.openigtlink.org), last accessed: 2014-10-02

## 3 Related Work

The following sections present information about image fusion and imaging phantoms. In detail, this chapter presents previous developed imaging phantoms of the brain. Furthermore, research regarding image processing and especially feature extraction, image registration and image fusion is outlined. Finally, related applications and algorithms performing multimodal 2D/3D image fusion are presented. A brief assessment checks if the presented approaches are suitable for the use case of this thesis.

### 3.1 Phantom Development

Simulation of the brain, the brain surface and its movements is a very active and complex field in the research community. According to Pogue et al. [PP14], imaging phantoms are used for the initial testing of system designs, optimizing signal to noise ratio in existing systems, performing routine quality control and comparing performance between systems. The authors refine these categories for tissue optical phantoms:

- Validate models and simulations
- Test and optimize performance
- Calibrate instruments
- Test stability and reproducibility

Those refined tasks apply also to the phantom and task of this thesis. In general, a phantom should model the object it mimics as best as possible. In the medical domain of brain imaging, it should be shaped like a brain. The surface should resemble the brain surface. The material of the imaging phantom should have similar properties like the brain tissue. An imaging phantom should allow repeatable tests and deliver reproducible results. Imaging phantoms for MRI and TI need to have distinguishable features, visible in both modalities. In order to use the imaging phantom with MRI, no ferromagnetic parts are allowed. The design of the imaging phantom has to provide distinct temperature gradients in order to be useful for thermographic imaging.

Chen et al. [CHG<sup>+</sup>10] developed an imaging phantom with measurable features in CT, MRI and ultrasonic imaging (figure 3.1). Shape and form of their phantom is based on the left hemisphere of the Colin27 dataset (Holmes et al. [HHC<sup>+</sup>98]). It is cast in TangoPlus Polyjet Resin FC-930 (RedEye, [Red14]). This material was chosen because it is similar to human brain tissue. The phantom has integrated fiducial markers which are visible in the mentioned imaging modalities. Additionally, their imaging phantom has a built-in polyvinyl acetate (PVA-C) tumour which lies not on the border of the brain but below the surface. The structure and form of the imaging phantom is malleable because of an integrated catheter. This catheter can be filled with 10 ml of liquid using a syringe to simulate brain shift. It has no visible features targeted at TI and does not allow a simulation of perfusion. Furthermore, it does not take into account the trepanation during the surgery which restricts and steers the movement of the brain.

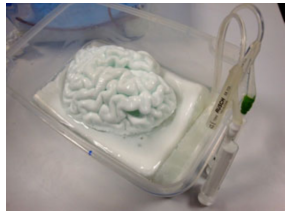


Figure 3.1: Imaging Phantom by Chen et al. [CHG<sup>+</sup>10]



al. [RC06]

Figure 3.2 shows an imaging phantom presented by Reinertsen et al. [RC06]. It has visible features in MRI and ultrasonic imaging. The phantom is able to simulate brain shift. It is cast in a PVA-C solution. Additionally, small plastic tubes are integrated into the imaging phantom. With them, it is possible to simulate perfusion. A catheter with an attached syringe allows simulation of brain shift and with it, evaluation of non-linear image registration algorithms. Shape and surface of the phantom are based on a form delivered by SKS Sibley Co. ([Co.14]). There are no features for TI. As the mentioned imaging phantom developed by Chen et al., their phantom does not take into account the restrictions and changes introduced by the trepanation.

Because TI is a modality which has not yet been established in the field of medical brain imaging, no phantoms which use both, MRI and TI, have been developed. The imaging phantom presented in section 3.1 is the first which combines trepanation, brain shift and perfusion. Additionally, it is built to work with computed tomography and white-light imaging.

## 3.2 Image Processing

The second part of this chapter deals with various image processing operations during image fusion. Here, techniques of several fields of computer vision and computer graphics are important. Figure 3.3, depicts the basic steps necessary for image fusion.

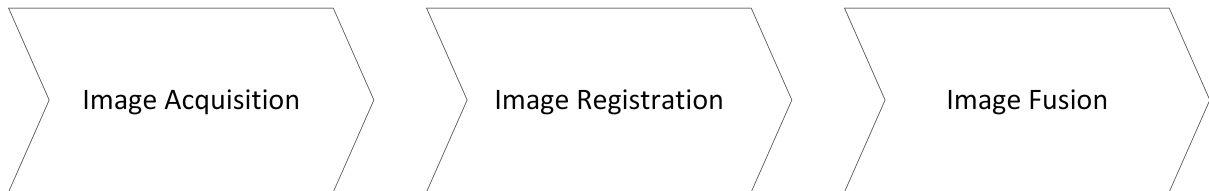


Figure 3.3: Basic steps during image fusion

To create a synthesized image, two or more images are combined. The step of *Image Acquisition* is described mainly in section 2.3 (Hardware) and section 2.1 which describe TI and MRI. The next sections elucidate related work concerning image registration and image fusion.

As mentioned before, image fusion is the process of combining two or more images to one image. The input images show either exactly the same scene but imaged with different modalities or they show different, maybe overlapping parts of the same scene in the same or different modality. To fuse the input, the images need to be aligned in order to gain a correct and precise overlay. Aligning images means to transform the images in such a way, that an observer who looks at the resulting scene, sees a perfect overlay of the images. The overlay of two input images is perfect when structures, which are visible in both images, appear in the output image at the same location. Some basic transformations are translation, rotation and scaling. More transformations are described in section 3.2.2.1. The second step, shown in figure 3.3, called *Image Registration*, tries to find this transformation with the help of features and similarity measures or with calibration parameters. A feature is a distinct and identifiable property of an image. When a feature is identifiable and describable in both images, an algorithm can calculate the transformation by minimizing a similarity measure. Possible features are described in section 3.2.1. A thorough description of similarity measures and their examples exceeds the scope of this thesis. For more information on similarity measures, please refer to Mani et al. [MA13], Razlighi et al. [RKY13] or Goshtasby et al. [Gos12]. Calibration-based image registration methods rely on external tracking systems, pre-calibrated instruments or other manual measurements. Image registration is described in detail in section 3.2.2. After the process of image registration is complete, image fusion is performed. This process is described in section 3.2.3.

### 3.2.1 Features and Feature Extraction

Feature Extraction is an important step during image registration. The description and extraction of features is a wide and well-known field in the computer vision and computer graphics community. As mentioned before, image registration tries to find a transformation between a moving image  $I_m$  and a reference image  $I_{ref}$  so that pixels with corresponding intensities are aligned perfectly. To calculate the transformation, certain properties are necessary. These properties are called features. The overall process is comparable to the one, a human would do: to look at both images, find some pixels which are visible and identifiable in both images and align the images so that these pixels overlap. Here, the pixel's intensities are so-called point-features. Besides points, many other features exist. Figure 3.4 and 3.5 depict some of them. Please note that both figures show only the most common features. Objects which are located in an ellipse represent a category. Objects which are underlined represent specific examples.

#### 3.2.1.1 Intensity-Based Features

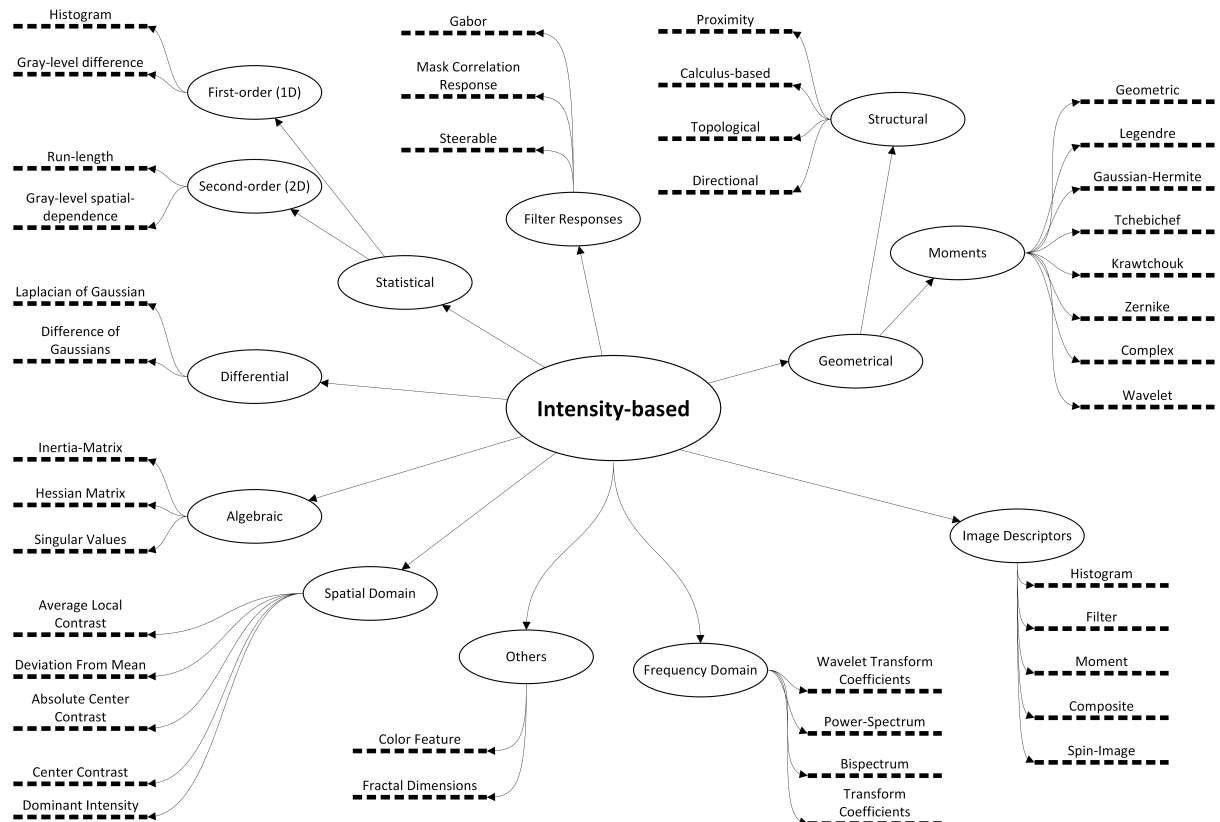


Figure 3.4: Features based on pixel intensities

Figure 3.4 lists features based on pixel intensities. These features do not work with shapes. On the contrary, they are based only on intensities of single pixels or groups of them. The following chapter will

outline some fundamental and important intensity-based features.

*Spatial-Domain Features* are calculated from the raw image intensities. For example, deviation from mean represents the mean difference between image intensities of two images. Another example is the dominant intensity. Here, the number of pixels which have this very intensity are counted and used as a feature. Spatial-Domain features are usually calculated for a small region of an image. [Gos12]

*Algebraic Features* unite features which represent intrinsic attributes of images. For example, Eigenvalues, Singular values or values based on the Hessian or inertia matrix. They are often calculated for the whole image. However, it is possible to calculate them for smaller regions. Both matrices can be used to analyse and extract features in a local neighbourhood. The inertia matrix utilizes Eigenvectors and Eigenvalues to determine changes in image intensity in the neighbourhood of pixels. The Hessian matrix is based on the curvature in the local neighbourhood of a pixel. [Gos12]

*Statistical Features* describe images regarding their distribution of pixel intensities. They can be differentiated in first-order and second-order statistical features. The former work with the probability that an image will have a pixel with a certain intensity. The latter work with the probability, that two pixels at a specific position will have the same intensity. Basic examples for statistical features are the peaks in a histogram, the standard deviation of image intensities and the mean intensity. [Gos12]

*Geometric Features* work with the layout of pixel or voxel intensities. Two main categories are identifiable: structural features and moments. The former uses relationships like the total number of a certain geometric element (i.e. line or circle with a distinct radius), topology (adjacent, overlap, ...), direction (north-of, east-of, ...) or proximity (close, far, ...) to describe an image. The latter is a category which represents, a region of interest as a scalar value. Examples are the centre of mass as a first-order moment. Second order moments are called moments of inertia. [PR92]

Despite the fact, that Spatial-Domain features are a very own category, all the mentioned features are calculated in the spatial domain. *Frequency Domain Features* break with this form of feature extraction. The calculation of transformations like Discrete Cosine Transform (DCT), the Discrete Fourier Transform (DFT) and with it, the calculation of transform coefficients leads to features which are able to describe the image.

*Differential Features* are very similar to simple image filters. According to Koenderink and van Doorn [KvD87], are “...certain filter operations [...] equivalent to partial derivatives of image intensities after smoothing”. Furthermore, the concatenation of filters is similar to higher order derivatives after even more smoothing. With this finding, several features based on filters were developed. For example, smoothed intensity, gradient magnitude or Laplacian isophote curvature (Haar-Romeny et al. [tFSV94]).

According to Goshtasby et al. "...the Laplacian of Gaussian has received the most attention" because it can detect dark and bright blobs of different sizes.

*Descriptors or Image Descriptors* combine the power of several features. In general, an image descriptor is a vector of features. Descriptors can be divided into two classes: window and global. Global descriptors describe the whole image whereas window descriptors are only valid for a certain region of an image. This region can be a square, a rectangle but also a circle. However, many descriptors are applicable in global and window scale. Prominent examples for descriptors are the Scale-Invariant Feature Transform (SIFT, [Low99]) which is able to identify blobs in images.

Summarizing, a wide field of features based on image intensities was mentioned without taking into account shapes in an image. They are also referred to as low-level features. Besides the mentioned and listed features, many more exist. Intensity-based features work best if both, the moving and reference images, show similar structures with similar gradients and image contrast. In other words, they are not very suited for multimodal image registration of infrared images and MR images. The following section outlines shape-based features which take into account the spatial relationships.

### 3.2.1.2 Shape-Based Features

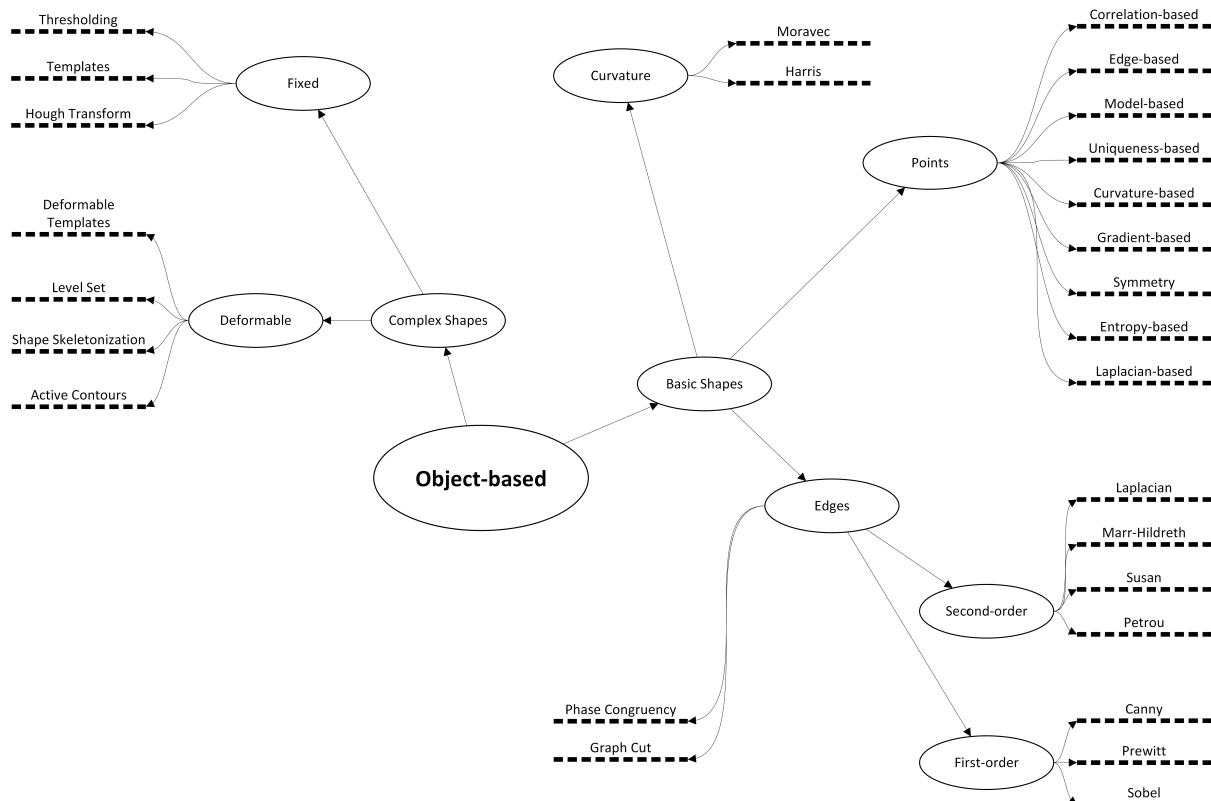


Figure 3.5: Features based on shapes

Figure 3.5 lists shape-based features. Here, spatial relationships are important. They are also called high-level features. Shape-based features can be divided into categories: basic shapes and complex shapes. Starting with basic shapes, three types are identifiable: *points*, *edges* and *curvature*. The following sections describe those categories.

A *point* is a single pixel or voxel which fulfils certain criteria. There are many detectors for points based on different strategies. A simple strategy is the intensity-based detector. Here, a pixel is marked as a feature point when its value exceeds a threshold. For example, this strategy is very useful when dealing with height maps where the intensity of a pixel represents the elevation. [NA12] The nodes of the vessel structure visible in TI could act as feature points.

An *edge* is another prominent type of feature. An edge is a connected line of pixels which fulfil certain criteria. One rather often used criteria is that pixels on an edge differ from their neighbourhood regarding image intensity. In other words, the contrast between the edge and its surrounding exceeds a threshold. Edge detectors can be classified into first-order and second-order detectors. First-order detectors will mark each pixel as an edge pixel if the difference of image intensity between the edge pixel and its neighbour is big enough. Well-known representatives of first-order edge detectors are the Sobel ([Sob70]) or Canny ([Can86]) edge detectors. Second-order detection algorithms will mark pixels as edges if the second-order derivative is zero. The vessel structure as well as the gyri could be represented by edges. An example for a second-order edge detector is the Marr-Hildreth operator ([MH80]).

Besides edges and points, *Curvature* is another important feature. In general, curvature describes the change in edge direction. A basic approach to calculate curvature is to connect pixels marked as edges and calculate a parametric curve. It is noteworthy, that curvature can also be used to detect corner points. An example for a curvature detector is the Harris detector ([HS88]). [NA12] The curvature of the brain surface could deliver curvature features.

Complex Shapes are, compared with basic shapes, more sophisticated and powerful. They enable algorithms to describe and extract features of arbitrary shape. They can be classified into two basic classes: fixed shapes and deformable shapes. Fixed shapes refer to all complex shapes which do not evolve or deform whereas deformable shapes change their appearance during execution. The following section outlines features based on complex shapes.

One general method for complex shapes are *templates*. With the use of templates, an algorithm tries to locate the shape of the template in the images. An easy approach is to place the template somewhere and count the pixels in the image matching the template. If not all or not enough pixel match, the template is moved and counting starts again.

The *Hough Transform* (HT) allows algorithms to generate arbitrary parametric shapes for template matching. It was introduced by Hough in 1962 (see [Hou62]) and was initially targeted on detecting straight lines. Various improvements extended the HT to detect circles, ellipses and various shapes. The latter one is called *Generalized Hough Transform* (GHT). Applied correctly, it delivers the same results as template matching but in a faster way (see. Princen et al. [PIK92]).

Contrary to fixed shape models, deformable shapes do not search for shapes, but rather evolve. Deformable templates, active contours and shape skeletonization are three techniques which are able to detect shapes which can not be defined exactly or at all.

*Deformable templates* work with constraints that describe a specific shape. For example, Yulli et al. [Yui91] describe a technique for detecting eyes. They extract two basic shapes, an ellipse and a parabola. The ellipse represents the pupil and the parabola the shape of the eye. While size and position of both shapes can vary, the condition that the ellipse has to be inside the parabola, must be fulfilled because the pupil is always located inside the eye. If the algorithm finds the specific constrained shape in both images, it will be considered as a feature.

*Active contours* work in the way, that a set of points is placed around the possible feature. The algorithm then moves the points closer to the shape until a criterion is fulfilled. The contour then encloses and therefore represents the shape [KWT88]. In TI, the boundary of the tumour might be visible and found by active contours.

*Shape skeletonization* is a concept which reduces the complexity of an image dramatically. For example, a hand can either be described through its border consisting of many pixels, or with six lines. One for the heel of the hand and five for the fingers. The latter is called a skeleton. The skeleton is the feature. A simple skeletonization approach is Thinning [Dav12]. The structure of vessels or gyri visible in MRI and TI could be represented by a skeleton.

Summarizing, a huge amount of features exist. The mentioned features are some of the most prominent as well as basic ones. Intensity-based features can be applied to extract features globally and locally but they do not incorporate spatial relationships. In contrary, shape-based features often rely on spatial relationships. Moreover, they do work with objects or shapes like points, edges or arbitrary shapes. Features do not only enable image registration but are also helpful for the evaluation of image registration algorithms. For example, the geometric distance between two point features can act as a measure for registration accuracy. However, extracting features is a process which takes a considerable amount of time. If the application needs to perform in real time or near real time, it is necessary to use features which can be calculated fast. Furthermore, feature extraction will only work if both images show the same objects or have similar structures. Working with infrared images and MR images, this can be the

case, but not necessarily. This makes it in general hard to identify corresponding features in both images. The following sections outline the overall procedure of image registration using features but also with calibration parameters.

### 3.2.2 Image Registration

“Image registration is the process of spatially aligning two images of a scene so that corresponding points assume the same coordinates. This process enables finding, for each point in the first image, the corresponding point in the second image” [Gos12]. The first image is the *reference image* and the second image is the *moving image*. In general, “Registration ... is the process of aligning two or more images that capture the geometric structure of the same scene, but in their own relative coordinate frames, into a common coordinate frame” [SKS13]. To achieve this, “... image registration [tries] to find a geometric transformation between corresponding image data” [Mod04]. Modersitzki et al. add [Mod04] that it is important to know, that the terms optimal and corresponding can differ throughout the application domains. Sometimes, the overlap of both images has to be very precise, sometimes a small error is tolerable. In general, this transformation is found by minimizing a similarity metric. For example, an algorithm identifies a unique structure in both images and tries to minimize the distance between both structures. An alternative approach utilizes calibration parameters which specify the transformation.

In this thesis, registration means the alignment of the acquired thermographic image with a pre-operative acquired 3D model. The following sections describe common taxonomies, algorithms and measurements for image registration. For more detailed information about and further research on image registration, please refer to [SKS13], [Mod04] and [Gos12].

#### 3.2.2.1 Taxonomy

A well-known taxonomy for medical image registration was introduced in 1998 by Maintz et al. [MV98]. Figure 3.6 outlines the nine distinct categories the authors have used to classify medical image registration techniques.

*Dimensionality* refers to the dimensions of the reference and moving image. If registration is not time-dependent, meaning that both  $I_m$  and  $I_{ref}$  are static images, it will only be necessary to find the geometric transformation once. Here, involved pairs of dimensions are 2D to 2D, 2D to 3D and vice versa as well as 3D to 3D. If registration is time-dependent, meaning that the application has to deal with a moving image which size, orientation and position change over time, a fourth dimension has to be considered: time. Time can have two distinct meanings: first, algorithms might have to deal with a (near) real-time

| Registration Methods |                              |                          |                          |                |                         |                     |              |                     |
|----------------------|------------------------------|--------------------------|--------------------------|----------------|-------------------------|---------------------|--------------|---------------------|
| Dimension            | Nature of Registration Basis | Nature of Transformation | Domain of Transformation | Interaction    | Optimization Procedure  | Involved Modalities | Subject      | Object              |
| Spatial and temporal | Extrinsic                    | Rigid                    | Local                    | Interactive    | Parameters computed     | Monomodal           | Intrasubject | Head                |
| Spatial only         | Intrinsic                    | Affine                   | Global                   | Semi-automatic | Parameters searched for | Multimodal          | Intersubject | Thorax              |
|                      | Non-image based              | Projective               |                          | Automatic      |                         | Modality to model   | Atlas        | Abdomen             |
|                      |                              | Curved                   |                          |                |                         | Patient to model    |              | Pelvis and perineum |
|                      |                              | Non-rigid                |                          |                |                         |                     |              | Limbs               |
|                      |                              |                          |                          |                |                         |                     |              | Spine and vertebrea |

Figure 3.6: Taxonomy of medical image registration according to Maintz et al. [MV98]

data stream which requires them to work fast. Second, the data stream can be a recording of two video sequences. Here, the execution time is not as important as in the first case.

*Nature of Registration Basis* knows three classes. Medical image registration applications based on *extrinsic* methods rely on foreign objects like implanted or glued fiducial markers. Applications using *intrinsic* methods perform image registration with non-foreign objects. For example, landmarks like the nose or the ear of a patient. Finally, *non-image based* registration methods use pre-calibrated coordinate systems. Here, the reference image is in the same coordinate system as the moving image and the geometric transformation is provided by a calibration.

The *Nature of the Transformation* describes the way, how the moving image is transformed to align perfectly with the reference image. Mani et al. mention [MA13] five general types which are named with their invariants in table 3.1. *Rigid* transformations are made of translations and rotations. They preserve the length of lines, parallelism, and angles. When a transformation is *affine*, each dimension can be scaled in addition to rotation and translation. A *projective* transformation “...has no physical basis in image registration” except in 2D to 3D registration. Imagine an x-ray image. This image is a two-dimensional view of a three-dimensional object. Projective transformations are necessary because objects which are farther away in the real world, appear smaller in the 2D image. The same goes for images acquired via an infrared camera. This kind of transformation does not preserve the length of lines, parallelism, and angles. However, straight lines remain straight. *Curved* transformations are, in general, not represented by matrices as the previously mentioned transformations. Instead, they are often represented in terms of local vector displacements or disparity fields. In other words, to each position a certain distortion is added according to the vector field. They do not preserve the length of lines,

parallelism or angles and straight lines do not remain straight. *Non-rigid* transformations try to tackle the fact that the human body certainly does not behave rigid and not even affine. In order to cope with the non-linearity of the human body, non-rigid registration techniques are part of the most interesting work in image registration [MA13]. According to Mani et al., “they require a great deal of computation time”. In their work they mention splines, elastic models, fluid registration, the demon’s algorithm as examples. They have the same invariance properties as curved transformations.

|            | Straight lines | Parallelism | Lengths | Angles |
|------------|----------------|-------------|---------|--------|
| Rigid      | yes            | yes         | yes     | yes    |
| Affine     | yes            | yes         | no      | no     |
| Projective | yes            | no          | no      | no     |
| Curved     | no             | no          | no      | no     |
| Non-rigid  | no             | no          | no      | no     |

Table 3.1: Natures of the Transformation

The next category in the taxonomy of Maintz et al. is *Domain of the Transformation*. Here the two mentioned categories are *local* and *global*. Global transformations are applied to the whole image. Local transformations are only applied to a certain part or region of interest of the image. It is possible to apply several local transformation to different parts of the image.

*Interaction* refers to the amount of user interaction which is necessary in order to perform registration. *Automatic* registration algorithms do all the work after they have been started and the data has been provided. *Semi-automatic* algorithms need a certain part of human interaction. For example, the user selects a region of interest or steers the algorithm otherwise. When using *interactive* algorithms, registration is performed by the user. The application acts only supportive.

The *optimization procedure* describes the method how parameters for the transformation are acquired. They can either be *computed* from available data or *searched for*. Applications which compute parameters do this with calibration parameters. Applications which search for parameters try to optimize some function defined on parameter space [MV98]. Examples for those functions are mentioned in section 3.2.2.2.

Medical image registration techniques are divided into two categories according to their *involved modalities*: *monomodal* and *multimodal*. Monomodal applications use images from only one modality, i.e. images from several CT scans. Multimodal image registration works with data acquired from two or more different sources. For example, the registration of MR and CT images. Multimodal image registration without a-priori knowledge is often “...very difficult as images acquired from different modalities

can have very different intensity mappings”. And with these different intensity mappings, no common features can be extracted.

The term *subject* describes the object from which images are taken. In the domain of medical image registration this is the patient. *Intrasubject* refers to applications which register various images from one patient. *Intersubject* refers to applications which registers images from different patients. In applications based on *atlases* only  $I_m$  is an image of the subject. The other images are obtained from a database. This database is called atlas.

Finally, the term *object* describes the specific part of the patient which is imaged. The six categories identified by Maintz et al. are coarse but complete. Mani et al. have added the for us important brain and several other internal organs.

With this last category, the taxonomy of medical image registration presented by Maintz et al. is complete. However, image registration algorithms can be organized in many ways. Another differentiation of image registration techniques is the division into *high-level* and *low-level* algorithms. Low-level algorithms use features calculated without information about spatial relationships, meaning shape information. High-level features however work with features based on certain spatial relationships.

Laliberte et al. [FG06] propose another characterization of image registration techniques. They divide algorithms according to *feature space*, *similarity metric*, *search space* and *search strategy*. The first two describe the type of image information and the method of comparison used during alignment. Search space describes the type of this transformation. For example, it can be an affine or a projective transformation as it is described in *Nature of Transformation*. Search strategy is part of the algorithm which finds the scale, rotation, and translation parameters. This means that they only deal with image registration techniques categorized under *searched for*. Calibration-based image registration techniques are not incorporated in this classification.

After describing different characteristics of medical image registration, the general procedure of image registration algorithms is elucidated. The following section describes feature-based image registration. After that, an explanation of calibration-based image registration follows.

### **3.2.2.2 Feature-Based Image Registration**

As mentioned in section 3.2.2.1, intrinsic and extrinsic image registration are based on features. The general procedure for an image registration algorithms using features is depicted in figure 3.7.

*Preprocessing* deals with raw images delivered by the imaging devices. Smoothing or segmentation are typical operations applied to these images in order to get the best results possible. Furthermore, this step

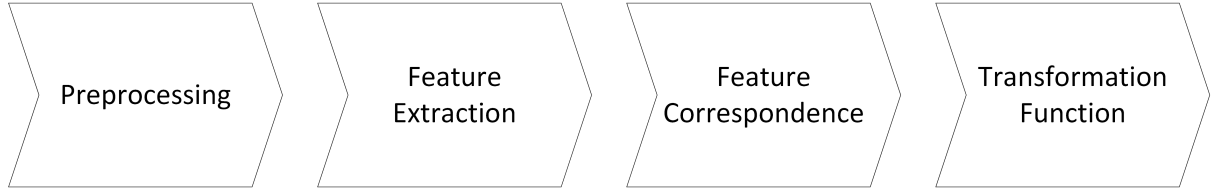


Figure 3.7: Pipeline of image registration using features

is necessary to provide the best result during feature extraction. However, preprocessing is not part of this thesis. *Feature Extraction* is step two. Possible features were described in section 3.2.1. Please note that features have to be extracted in the moving and the reference image. Step three tries to find *Feature Correspondences* between both images. Correspondences can either be defined manually by the user, i.e. by selecting pairs via the user interface of the application or automatically by an algorithm. The latter can be divided into three general methods. First, the user can select features in the reference image and the algorithm searches for their counterpart in the moving image. Second, the user can select several features in the reference and the moving image and an algorithm searches for corresponding pairs. Third, the algorithm can find and match features on its own. To select feature pairs which correspond best, a registration algorithm has to solve an optimization problem. Here, the objective is to minimize the difference between the two images. For this, numerous measures or metrics exist. A metric is a computation which produces a higher value as correspondence between two values in a series increases [KT09]. The metric produces a numeric value for the quality of a feature correspondence or set of transformation parameters [BL06]. Goshtasby et al. [Gos05] names the following five general strategies: (1) point pattern matching, (2) line matching, (3) region matching, (4) chamfer matching and (5) template matching.

(1) *Point Pattern Matching* takes three pairs of corresponding point pairs randomly and computes the transformation.

$$H(I_{ref}, I_m) = \max_{p \in I_{ref}} \min_{q \in I_m} \|p - q\| \quad (3.1)$$

In order to check the transformation, the *Hausdorff Distance*  $H$  (maximum of all minimum distances) is computed using equation 3.1.  $p$  and  $q$  are points of  $I_m$  and  $I_{ref}$ . If  $H(I_{ref}, I_m)$  is below a certain threshold, an acceptable transformation is found.

(2) *Line Matching* compares two lines which might correspond according to their properties like orientation, length or position. If these properties are the same, the transformation will be computed.

(3) *Region Matching* will be an appropriate strategy if the registration process relies on image regions. If the algorithm just operates on centroids, it will be similar to point pattern matching. However, a region also provides information about size and shape. This information can be utilized for improving

the overlap.

(4) *Chamfer Matching* calculates the sum of all distances  $CH(I_{ref}, I_m)$  between corresponding edge point pairs as shown in equation 3.2. If the sum is above a threshold, the moving image will be translated until the sum is below a threshold. For this, the image is transformed into an approximate distance.

$$CH(I_{ref}, I_m) = \min \{DT(I_{ref}, I_m)\} \quad (3.2)$$

“The process of conversing an [...] image to an approximate distance is called distance transform DT” [GIK03]. Examples for distance transforms are the Euclidean distance or the Manhattan distance.

(5) *Template Matching* utilizes not only geometrical properties like position or shape, but also image intensities or statistical properties of the template. An example for the former is the sum of absolute differences  $SAD$  (or, according to [DK82], Minkowski metric).

$$SAD[x, y] = \sum_{i=0}^{b-1} \sum_{j=0}^{w-1} |I_{I_{ref}}[i, j] - I_{I_m}[i, j]| \quad (3.3)$$

Equation 3.3 adds up the differences of image intensities  $I$  for corresponding pixels of the reference image  $I_{ref}$  and the moving image  $I_m$ . Both images have a size of  $b \times w$  pixel. “The smaller [the Difference], the more similar will be the template and the image” [Gos05]. An example for the latter, a statistical property, is *Mutual Information* (MI) or *transinformation*. The origin of MI lies in information theory. It measures the entropy of the joint density and is therefore based on joint probabilities. The general assumption is that images which correspond have highly dependent image intensities. Therefore, the joint probabilities should also be high and with it MI.

$$MI(I_{ref}, I_m) = \sum_i \sum_j P_{I_{ref}, I_m}(i, j) \log_2 \frac{P_{I_{ref}, I_m}(i, j)}{P_{I_{ref}}(i) P_{I_m}(j)} \quad (3.4)$$

Equation 3.4 shows the calculation of MI.  $P_{I_{ref}}(i)$  is the probability, that the image intensity  $i$  will appear in  $I_{ref}$ .  $P_{I_m}(j)$  is the probability, that the image intensity  $j$  will appear in  $I_m$ .  $P_{I_{ref}, I_m}(i, j)$  the probability that corresponding pixels of both images have the intensities  $i$  and  $j$ . The higher  $MI(I_{ref}, I_m)$  is, the more dependent are the intensities. MI is, according to Mani et al. [MA13] the most common used measure. Collet et al. [CCC10] say that MI “provides a robust and efficient tool for statistical image comparison”

Besides the mentioned measures, many more based on spatial, statistical and geometrical properties exist. More similarity and dissimilarity metrics are mentioned and evaluated extensively in [Gos12]. Despite all mentioned work, rapid computation of image feature correspondences is still an open problem. [Sze06]. When step three of figure 3.7 has been executed successfully, meaning corresponding feature pairs have been found, the transformation function can be calculated. In general, the algorithm looks for

a transformation

$$T : I_m \mapsto I_m \quad (3.5)$$

which transforms the moving image in a way that the distance measure is minimized. Assuming a linear registration problem which deals with three dimensional data, the transformation can be written as

$$P = SRp + T \quad (3.6)$$

where  $P$  and  $p$  are the new and old points of the image and  $R$  is a matrix representing the rotational difference.  $S$  is a vector which defines the difference in scale while  $T$  is a vector which defines the translational difference. In general, the scaling parameter is determined first. Then the rotational difference followed by the translational difference is calculated. The different natures of transformation functions were described in section 3.2.2.1. The rather simple equation is only applicable, if the transformation is linear. Depending on the involved modalities and the mentioned nature of transformation, a different number of corresponding point pairs is necessary (3,4 or 6). If a non-linear transformation is applied, the equation from 3.6 is not applicable any more. Non-linear transformations require more sophisticated mathematical tools. The description of these tools would exceed the scope of this thesis. For more information, please refer to Sotiras et al. [SDP13], Klein et al. [KAA<sup>+</sup>09] and Scherzer et al. [Sch06].

Summarizing, feature-based image registration has to extract features in both images, find corresponding feature pairs and calculate the transformation function. The correspondences are acquired using a metric. With the help of corresponding features, a transformation function can be calculated. In general, feature-based image registration can be applied to a wide variety of input data. Due to the fact, that feature extraction and matching is a computational expensive task, it is not well-suited for real-time or near real-time processing. Despite the wide range of features and metrics, it is hard to find corresponding features when trying to register multimodal images.

### 3.2.2.3 Calibration-Based Image Registration

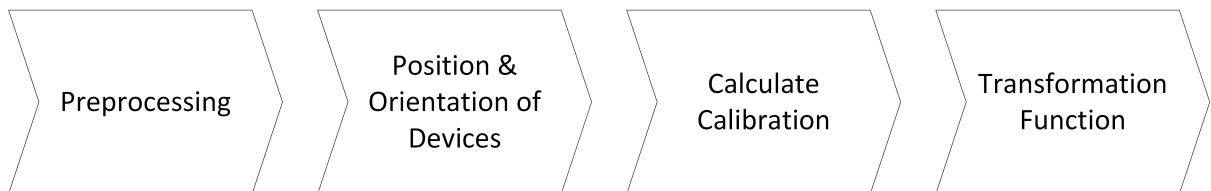


Figure 3.8: Calibration-based image registration

Calibration-based image registration is “...based on carefully pre-calibrated imaging devices and establishment of the position of the operation table with respect to the imaging device during imaging

acquisition” [MTLP12]. The pipeline shown in figure 3.8 depicts the general steps during calibration-based image registration. The first and last step are the same as in the feature-based image registration. However, the steps concerning feature extraction and feature correspondence are replaced. Instead of calculating features, it is necessary to acquire spatial information about the involved objects. Additionally, a calibration is necessary. The calibration represents the displacement in orientation, position and scaling of  $I_m$  and  $I_{ref}$  in the world coordinate system ( $cs_w$ ). With this calibration, it is possible to calculate the transformation function which aligns  $I_m$  with  $I_{ref}$ . Calibration-based image registration can be considered static when the imaging devices or subjects do not move. It can be called dynamic when the position and orientation of objects can change. In the dynamic case, the transformation function has to be recalculated every time the spatial data changes.

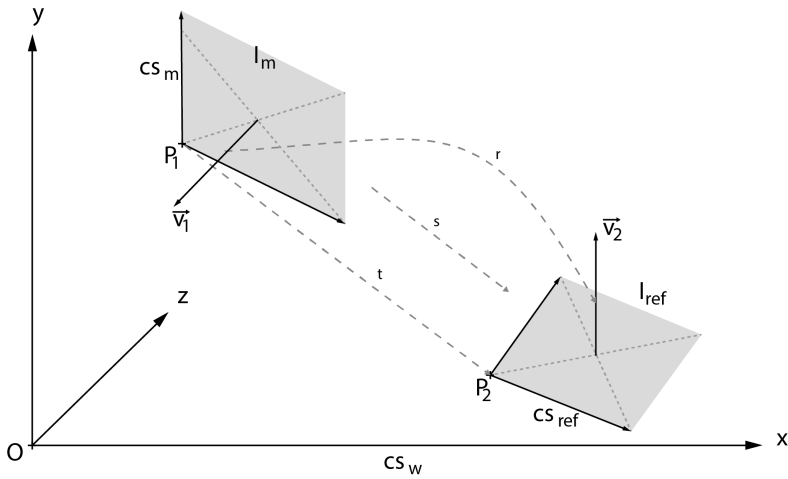


Figure 3.9: Coordinate system with two objects  $I_m$  and  $I_{ref}$  in the world coordinate system  $cs_w$

Figure 3.9 illustrates the problem. In general, calibration-based image registration relies on information about the difference in scale, orientation and position between  $I_m$  and  $I_{ref}$  in  $cs_w$ . The application needs to know the difference between  $P_1$  and  $P_2$ . This information is represented by the translation  $t$ . The difference between the surface normals  $v_1$  and  $v_2$  is represented by the rotation  $r$ . Finally, the dimensions of both images need to be the same size. It is not always the case, that the moving image has the same dimensions than the reference image. For this, scaling  $s$  is necessary:

$$s = \frac{\text{size}_{\text{moving}}}{\text{size}_{\text{reference}}} \quad (3.7)$$

where  $\text{size}_{\text{moving}}$  is the length (or height) of the moving image in one dimension and  $\text{size}_{\text{reference}}$  is the length (or height) of the reference image. Besides length or height, the scale factor can also be calculated with a distance between or the size of two objects visible in both images. Scaling can be uniform or non-uniform. When using non-uniform scaling, the scale factor can differ for each dimension. Scaling

as well as translation and rotation are represented by a matrix. With  $s$ ,  $t$  and  $r$ , an affine calibration-based registration is possible.

$$I'_m = s \cdot r \cdot I_m + t \quad (3.8)$$

$s$ ,  $t$  and  $r$  represent the calibration parameters. Using homogeneous coordinates, these transformations can be combined into one single calibration matrix  $M_c = M_r \cdot M_s \cdot M_t$  where  $M_r$ ,  $M_s$  and  $M_t$  are matrix representations of the rotation, scaling and translation. It is possible that additional rotations, translations and scalings are necessary. For example, to translate the origin of  $cs_m$  so that it is at the centre of the image. This makes rotations more intuitive. Those transformations are combined in an additional matrix  $M_a$ . With  $M_a$  and the calibration matrix  $M_c$ , the final transformation  $T = M_a \cdot M_c$  can be calculated. This results in

$$I'_m = T \cdot I_m \quad (3.9)$$

The image  $I'_m$  is then aligned with the reference image  $I_{ref}$  in the patient coordinate system. The overall process is called coordinate transformation. The application has transformed the coordinate system of the moving image ( $cs_m$ ) to overlap with the coordinate system of the reference image ( $cs_{ref}$ ). At the end of the calibration-based image registration, both images are registered. They overlay.

2D-3D and 3D-3D image registration require a rotation, translation and maybe a scaling. In addition, 2D-2D image registration might require a homography  $H$  [Dub09]. A homography will be necessary if the normal vectors of the imaging devices' sensors have not the same orientation. If this happens, the acquired images will show the object from different perspectives. The homography  $H$  corrects this difference. In the 2D-3D case, the moving image in the virtual world is placed on a position which correlates with the position of the imaging sensor in the real world. An additional projection step is necessary. More details regarding the projection step are provided in section 3.2.3.

Ruijters et al. [Rui10] use a mobile CT scanner to track instruments. The CT scanner acts as an imaging and tracking device. However, the general procedure is the same: The calibration  $M_c$  is represented by scanner's dimensions and geometry. With the knowledge of the dimensions of the imaging device and the location of the patient, the transformation  $T$  is calculated and applied to the moving image  $I_m$ . Neither the patient, nor the imaging device is allowed to move.

Sergeeva et al. [SUS<sup>+</sup>06] perform a calibration-based image registration for 3D ultrasonic images and 3D images acquired via CT. They do not rely on specifications of the imaging devices but use a neuron-navigation system. They register the patient to the neuronavigation system which also tracks the ultrasonic probe.  $M_c$  is calculated from spatial data delivered by the neuronavigation system. Additionally, a rotation and translation is applied. The result is the transformation  $T$ . The patient is not tracked. Therefore, the patient is not allowed to move. This would invalidate the calibration. The transformation is affine

and the overall registration error is  $1.9 \pm 0.97$  mm.

The calibration procedure has to be performed regularly [MML<sup>+</sup>11]. The regular repetition of the calibration procedure is not only important for real time applications, but is also necessary when the patient moves. Therefore, it is important to develop and design a simple calibration procedure.

Calibration-based image registration is a fast way to register images. It is faster than feature-based image registration, because no features need to be extracted and matched. The absence of feature extraction and matching also makes it easier to register multimodal images. This is because there is no need to find corresponding features in images which do not show the same structures. However, spatial information about involved imaging devices and subject is necessary.

### 3.2.3 Image Fusion

After the successful image registration, the images are aligned and overlay. In 2D-2D image fusion, the combination of both images can be done either by using transparency on one image or with contrast enhancement according to the colours of both images. The same goes for 3D-3D image fusion. However, when combining 2D and 3D images, some additional steps are necessary. As described in chapter 3.2.2, the transformation parameters for aligning the 2D image with the 3D image are available. In the affine case covered in this thesis, they consist of a translation, rotation and a scaling. The position of the virtual 2D image with respect to the 3D MR model is the same as the position of the infrared camera's sensor with respect to the subject. In order to combine both images, a projection step is necessary. Projection finds for each pixel of the 2D thermographic image the corresponding voxel of the 3D image and fuses image information.

To understand the process of image fusion, a short explanation about cameras and their nature is necessary. An IR camera can be modelled as a pinhole camera as shown in figure 3.10a. The camera performs the projection of the 3D object's voxels, meaning objects seen by the infrared camera, into 2D space of the sensor array. Objects which are farther away from the centre of projection appear smaller on the image plane. The size of objects depends on the *focal length*  $f$  and the distance from the projection plane. Assuming that  $f$  is infinite, then the application works with the model of an orthogonal camera. The principle of this camera is shown in figure 3.10b. Here, the centre of projection is infinitely far away. This results in parallel lines of projection. Hence, objects of the same size appear as objects of the same size on the image plane regardless of where they are in object space. Algorithms which describe the parallel camera model are more stable than projection algorithms [NA12].

Assuming the 2D image is acquired via an imaging device based on the model of a pinhole camera.

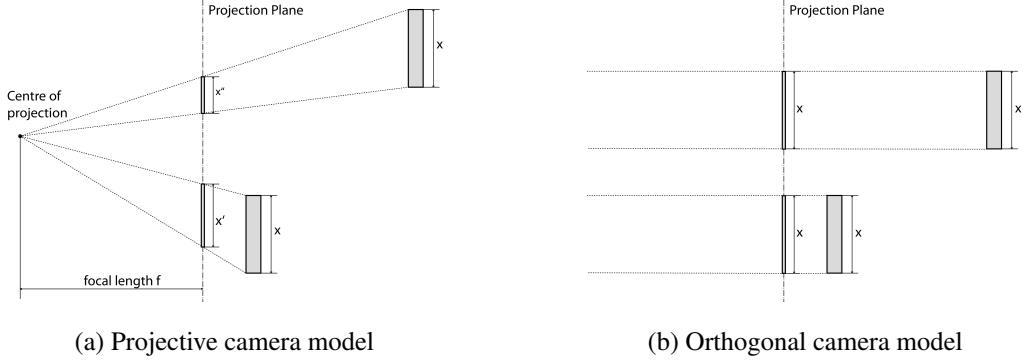


Figure 3.10: Comparison of both camera models. Using the projective model, the size of the objects  $x$  on the projection plane depends on the focal length  $f$ .

Projection of this 2D image onto the 3D surface will not be correct if the application does not consider perspective projection. An inverse projection mapping is necessary. In other words, the application needs to find the corresponding voxel of the 3D image for each pixel of the 2D image. When the voxel has been found, the application can fuse the colour information of the voxel and the pixel. This process can be represented by a  $4 \times 4$  matrix  $M_p$ . Equation 3.10 depicts the transformation for one pixel-voxel pair.

$$\vec{p} = M_p \cdot \vec{v} \quad (3.10)$$

$\vec{p}$  represents a point on the 2D image sensor. Vector  $\vec{v}$  is a coordinate of the 3D model. Both are located in the three-dimensional world coordinate system and are homogeneous coordinates. Matrix  $M_p$  can be decomposed into two matrices  $M_p = P \cdot T$  where  $P$  represents perspective transformation and  $T$  is an affine transformation matrix.  $P$  is determined by the focal spot  $f(f_x, f_y, f_z)$ , the centre of the image sensor  $c(c_x, c_y, c_z)$  and the size of the image sensor  $d(d_x, d_y)$ . Using these parameters, leads to

$$P = \begin{pmatrix} \frac{2}{d_x} & 0 & 0 & \frac{2(f_x - c_x)}{d_x} \\ 0 & \frac{2}{d_y} & 0 & \frac{2(f_y - c_y)}{d_y} \\ 0 & 0 & 1 & 0 \\ 0 & 0 & \frac{1}{f_z - c_z} & 1 \end{pmatrix} \quad (3.11)$$

With the help of this matrix it is possible to project every voxel of the 3D space onto the sensor array or virtual image, respectively. To do the inverse operation,  $P^{-1}$  is necessary. This operation is called *projective mapping*. However, "...the mechanisms that govern the projection of a 3D scene onto a 2D surface render the extraction of useful 3D information difficult" [TDAJ06]. In other words, the 2D image does not provide enough information to recreate the 3D image. One information which is often available, is the focal distance. However, using this information, only the position of those objects which are located on the focal plane can be calculated correctly. The position of objects which are behind or in front of the focal plane can not be calculated without further means. Literature mentions the usage

of stereo camera systems [SSN07] or light field camera systems [THMR13] to overcome this problem. Besides these techniques, algorithms based on Shape-From-Shading, Time-of-Flight, Shape-From-Focus and others can provide depth information [Moo08].

*Ray casting* is another possibility to find pixel-voxel pairs. It mimics central projection. For each pixel of the thermographic image, a virtual ray is cast starting from the centre of projection and going through each pixel. The ray is traced until it hits a voxel which belongs to the 3D model. This voxel gets a new colour according to the IR image. Using this technique, ray casting calculates depth information and enables a correct projection.

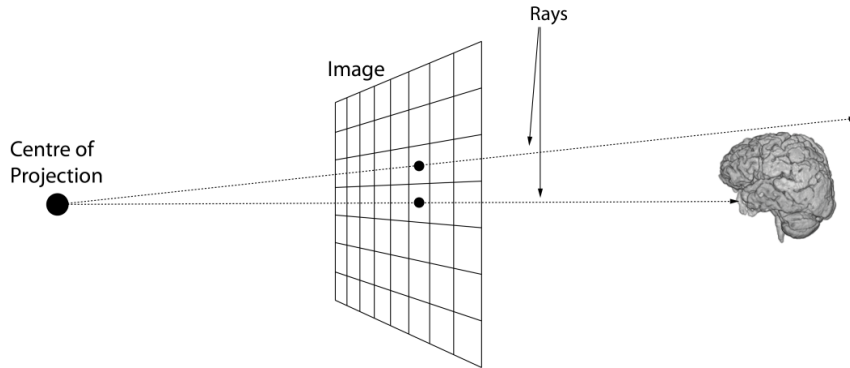


Figure 3.11: Rays, starting at the eye, going through pixels of an image and hitting an object or not.

As shown in figure 3.11, ray casting inverts projection done by the pinhole camera. If the ray starts at the centre of a pixel and the direction is orthogonal to the image plane, projection done by an orthogonal camera will be inverted. Ray casting has the inherent advantage that occluded voxels do not get assigned a colour value because no rays hit them. However, ray casting is a computational expensive operation. Parker et al. mention a time complexity of  $O(n^2)$  for a grid with size  $n \times n \times n$  pixels. Furthermore, the visualization has to be recomputed every time the thermographic image or the model change position or orientation because the centre of projection changes position.

*Texture mapping* is another image fusion approach. It is based on the work of Catmull et al. [Cat74]. In texture mapping, a 2D image is mapped onto a 3D surface. The 2D image is called texture. One pixel of a texture is also called *texel*. A corner mapping defines the relationship between texture and 3D object [Wol94].

Texture mapping translates the 3D coordinates  $(x, y, z)$  of a surface patch in object space (fig. 3.12, left) to 2D coordinates  $(u, v)$  of texture or image space (figure 3.12, middle). Here, the colour information of each texel is acquired. Then, colour and transparency are applied to the surface patch as the right image of figure 3.12 indicates. The mapping is performed for each pixel of the surface patch.

According to Oswald et al. [OT12], a "...texture mapping approach is more efficient" than pixel level

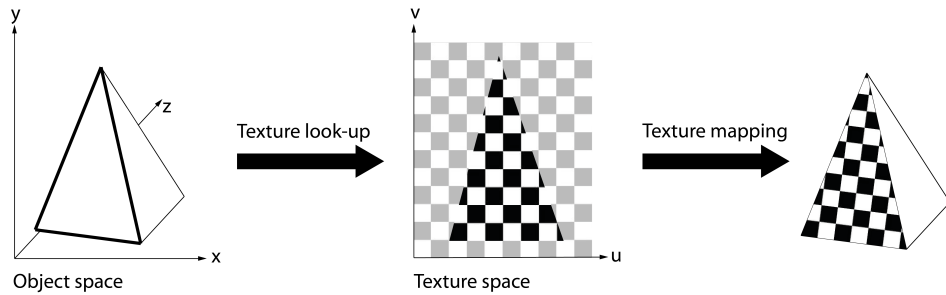


Figure 3.12: Texture mapping described for one face of a tetrahedron

image fusion. Verney et al. [VAA14] also use a texture mapping approach for image fusion of thermographic images with 3D models. Texture mapping however also needs re-computation but is considerably faster and can be used “...with only a modest increase in the complexity” [HS93]. Contrary to ray casting, occluded pixels get assigned a colour. Therefore, the 3D model is enriched with interpolated information which has not been measured by the IR camera. As long the viewing direction is the same as the camera direction, this error can be neglected. If the viewing direction however changes, this will be an issue. Texture mapping can either be affine or corrected perspectively.

The previous sections show that image fusion of 2D and 3D images is a complex task. The correct calculation or estimation of depth information is necessary in order to get a correct projection. Devices like stereo or light field cameras could provide depth information. However, additional devices are necessary and complicate the set-up. Ray casting, as another solution, is computational expensive. Texture mapping is a fast approach and promises good results.

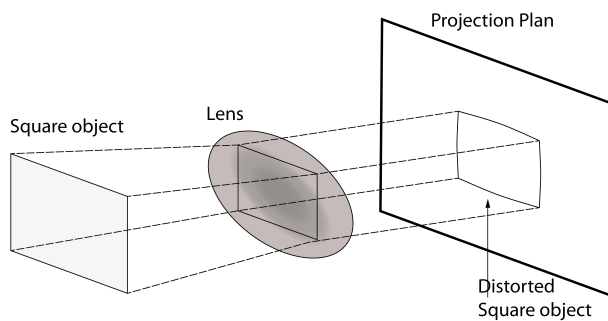


Figure 3.13: Example for lens distortion. The lens distorts the square object slightly

When the lenses of a camera are perfect, everything works fine with the mentioned approaches. However, common lenses introduce a distortion because of light refraction. It is possible to compensate this distortion. Szeliski et al. [Sze06] distinguish between radial and tangential distortions. According to Hartley et al. [HZ03], radial distortion is most important (see figure 3.13). Cheaper lenses with a smaller focal length as well as wide-angle lenses are more prone to radial distortion. A simple solution is to

correct the spatial information of the acquired 2D image with

$$\begin{aligned}x' &= x(1 + k_1 * r^2 + k_2 * r^4) \\y' &= y(1 + k_1 * r^2 + k_2 * r^4)\end{aligned}\tag{3.12}$$

where  $x$  and  $y$  are the original values,  $k_1$  and  $k_2$  represent the radial distortion parameters, and  $r^2 = x^2 + y^2$  describes the radial distance from the centre.  $x'$  and  $y'$  are the corrected values. Szeliski recommends acquiring an image with straight lines on it and searching manually for the correction parameters. Hartley generalizes this process with

$$\begin{aligned}x' &= x_c + L(r) \cdot (x - x_c) \\y' &= y_c + L(r) \cdot (y - y_c)\end{aligned}\tag{3.13}$$

whereas  $x_c$  and  $y_c$  are the centre of radial distortion.  $L(r)$  is a distortion function with  $r^2 = (x - x_c)^2 + (y - y_c)^2$ . An approximation to an arbitrary correction function "...may be given by a Taylor expansion". The principal point of the lens is often assumed as centre of distortion. Instead of searching for parameters manually, Hartley recommends usage of algorithms which minimize geometric errors for calibration objects such as the Tsai grid [Tsa86].

After correcting the 2D image acquired by the camera and mapping it onto the 3D surface, a last decision regarding colour, transparency and intensity of the resulting surface is necessary. The use of *transparency image fusion* is one possibility. With this approach, pixels of one image are not fully opaque but partially transparent. For example, this would allow the viewer to see the surface of the original 3D image as well as information of the mapped 2D image. Besides the transparency fusion technique, *contrast modulation image fusion* can be applied. Here, one image is normalized and multiplied with the colour values of the other image.

Colour combination is the last step during image fusion. The initial registration ensures that images are aligned. An appropriate projection technique finds corresponding pairs of voxels and pixels. Lens distortion has to be eliminated. Finally, colours of both images are combined. The following section provides examples which deal with multimodal 2D/3D image fusion.

### 3.3 Examples of Multimodal 2D/3D Image Fusion

In non-destructive testing, infrared imaging makes small cracks and other flaws of a workpiece visible. Oswald-Tranta et al. [OT12] perform image fusion of thermographic and geometric data for automated defect detection. Figure 3.14 shows the result. The thermographic image is acquired by an infrared camera. They created the 3D model of the workpiece via light sectioning (details can be found in [SO08]).

Registration of the images is based on intrinsic features. It requires a preprocessing step which segments images. After image segmentation, a binary image of the workpiece is available. The features for image registration are based on the contour of this binary image. Oswald-Tranta et al. have chosen the centre and radius of the inner circle, the direction of the maximum moment of inertia and the maximum length along the direction of inertia as features (see fig. 3.15). The transformation is affine.

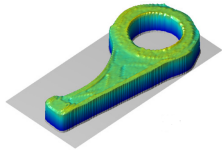


Figure 3.14: 3D model of a workpiece with thermographic data ([OT12])

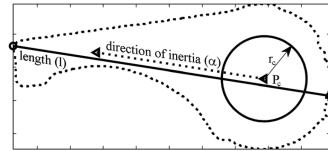


Figure 3.15: Features of the workpiece ([OT12])

Segmentation as well as image registration are based on form and structure of the workpiece. Both do not change. Therefore, it is easy to develop masks for segmentation and feature descriptions. Furthermore, there is a distinct temperature difference between thermographic image and 3D model. This is because the workpiece had been heated up before imaging. This enables the segmentation algorithm to output a precise binary image. Additionally, no movements of the imaging devices are possible. This enables a precise image registration. However, the static feature definition is not possible in many applications because subjects change and move. The authors provided no information about accuracy or complexity but mention necessary future work in order to improve both.

Verney et al. [VAA14] present another related image fusion application for non-destructive testing. They fuse images acquired via a thermographic camera with a 3D scan or a 3D model of a workpiece. Image registration is based on the Hough transform. This is possible because the subject has always the same structure and distinct gradients are visible due to a heating process. The 3D camera provides necessary depth information for image fusion which is based on projective mapping.

Kaczmarek et al. [Kac14] fuse thermographic data with a 3D object model. Their object model is a 3D point cloud acquired by a white-light scanner. They acquire temperature data via active dynamic thermography. Cooling is done via application of a stream of CO<sub>2</sub> and dry air. Image registration starts with a triangulation of the point cloud and the calculation of triangle normals. Registration is based on manual control points selected by an operator in both, the 3D model and the 2D image. The resulting transformation is affine.

Figure 3.16 shows the 3D mesh model and the fused image. Both images show the human chest. The application of Kaczmarek et al. does not perform real-time analysis. The manual registration with control points is prone to errors because the operator might select point pairs which do not correspond.

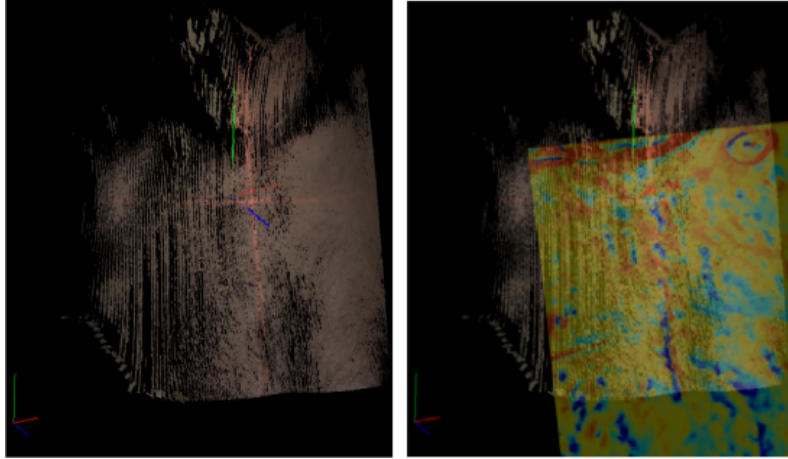


Figure 3.16: Results of Kaczmarek. Left: 3D mesh model. Right: 3D mesh model with merged thermographic data ([Kac14])

Besides that, the imaging device or patient might move and invalidate the point positions. As a solution, they propose the usage of tags which are visible in all modalities and are attached to the patients body throughout it's hospital stay (approximately seven days). The authors do not provide any information about registration accuracy. The overall examination lasts about 15 minutes.

Ayaz et al. [AIP<sup>+</sup>06] perform image fusion of an infrared image acquired via fNIR sensors with a 3D MR image. fNIR measurements are acquired by attaching a sensor array to the patient's skull. The authors place the sensor array "... so that the horizontal symmetry axis (central y-axis) coincides with symmetry axis of the head". Using the 10-20 head marker system ([HHP87]), they place the sensor in alignment with Fp1 and Fp2. Registration process is divided into two main parts. First, the vertical location is determined via Fp1 and Fp2 of the 10-20 system and the sensor array is placed at the mentioned locations at the patient's skull. These locations are known in the MR image which results in corresponding point pairs. Second, the horizontal location is calculated. For this, a 2D image is extracted from the 3D MR image. In detail, the very slice is taken which corresponds to the vertical location found in step one. This slice is transformed into a binary image using thresholding. Then, a Sobel filter is applied. The result is a boundary image of the brain (see fig. 3.17a). Because the geometry information of the sensor array as well as the position on the patients brain is known, it is now possible to find voxels which correspond to the locations of the sensor array (see figure 3.17b).

Interpolation algorithms calculate colour coded surfaces and map them on the surface. The result of registration and transparency-based image fusion using interpolated values is shown in figure 3.17c. Their method is able to provide a real time visualization of the acquired data. One reason for this is, as in previous work, that no feature extraction and matching step is applied. Their method is not prone to patient movement because the sensor array is attached to the skull.

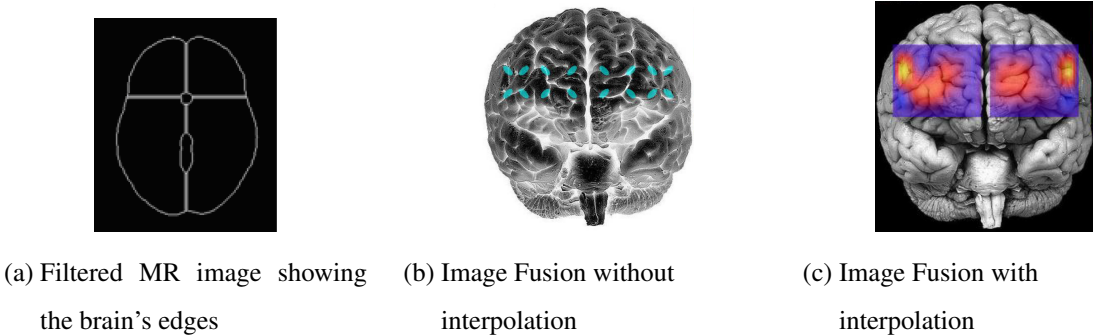


Figure 3.17: Different steps during image fusion developed by Ayaz et al. [AIP<sup>+</sup>06]

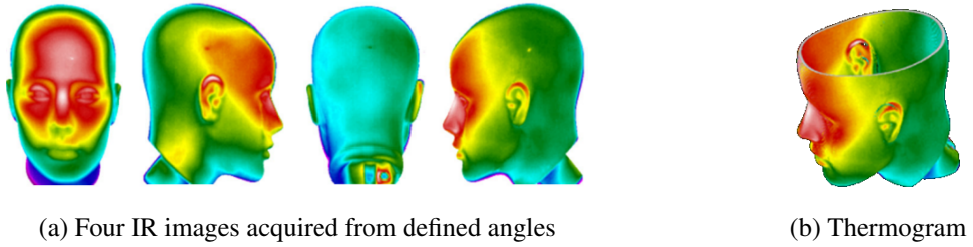


Figure 3.18: Images showing the image fusion of Sanches et al. [SGS<sup>+</sup>13]

Sanches et al. [SGS<sup>+</sup>13] fuse MRI/CT with IR data in order to generate a thermogram. A thermogram is a 3D model where thermographic data is available everywhere. At least four infrared images of the human head are acquired and segmented (fig 3.18a). The MR image is also segmented. In both cases, segmentation results in a boundary of the head. Because the IR images are acquired from known angles, an initial placement of the thermographic images is possible. The final registration is based on the boundary information acquired via segmentation. The temperature data is then mapped onto the MR image via texture mapping. Overlapping data is interpolated (fig 3.18b). The image acquisition process takes about two to three minutes.

## 3.4 Assessment of Registration Techniques

The mentioned applications and examples of image fusion using 2D thermographic images and a form of 3D objects indicate that current work with thermographic data mainly rely on manual landmarks or static and easily detectable features. This is because finding feature correspondences between MR images and thermographic images is an open problem. Distinct features which are visible in thermographic images are vessels at the surface of the brain. However, these vessels are not visible in the MR image. Here, most distinct feature are gyri of the brain. However, identification of those gyri in thermographic images is a problem which has not been solved yet.

Besides that, a major problem arises because of brain shift (see section 2.2). If image registration is based on features extracted from an MR image acquired preoperatively, the accuracy of registration decreases over time because the brain of the patient diverges from the acquired image slightly. In the worst case, a feature-based registration process fails because the application does not find any correspondences. To overcome this problem, the 3D model has to be updated during the surgery.

To our knowledge, no other solution for semi-automatic or automatic registration of thermographic images of the brain to a preoperative MR images is mentioned in literature. The following sections describe and evaluate some possible approaches briefly.

If it is possible to inject a contrast agent prior to acquisition of the MR image, another approach for image registration will be possible. The contrast agent enhances visibility of the brain's blood vessels in the MR image. A suitable segmentation algorithm can extract the vessel structure. A possible algorithm was presented by Wagner et al. [WKM<sup>+</sup>09]. With information about the vessel structure, a feature-based image registration is possible. Lines, curvature or skeletons can act as features. However, feature extraction and matching is still a computational expensive step which makes a real time or near real time image fusion more complicated. Furthermore, the application of a contrast agent is not always possible and without this additional information, this approach fails.

If an algorithm accomplishes an enhancement of the gyris visibility in thermographic images, the structure of the gyri can act as features. Via a description of this structure through lines, curvature, or skeletons, a transformation can be calculated. However, to our knowledge no such algorithm exists.

Another possible solution for the problem of registering IR with MR images would be to use an extrinsic and landmark-based registration algorithm where medical personnel marks distinct pairs of feature points manually, in both, the MR and the IR image. For example, on the computer with a mouse during or before surgery. An algorithm based on a distance metric and iterative closest point approach ([RL01]) could calculate a transformation which aligns the marked points as best as possible.

If the overall set-up includes an additional white-light camera, more possibilities will arise. Because it is easier to extract the gyri from white-light images, a registration from white-light images to MR images is easier. In other words, registration is based on two steps: First, registration of IR images to white-light images. Second, registration of white-light images to MR image. The combined transformation of both registration steps is the final transformation which registers the IR images to the MR image. Registration of white-light and IR images can be done using vessel structure which is visible in TI and white-light imaging. From the vessel structure, points, edges, curvature or skeletons can be extracted and act as features. With them, a transformation for image registration of white-light image and thermographic image can be calculated. Furthermore, statistical features like mutual information or histograms

can help to calculate this transformation. A calibration-based approach is also conceivable: When the positional and directional difference between both imaging devices is known, a static transformation can be applied. This would speed up the registration process because it would eliminate the recalculation of the registration between the thermographic image and the white-light image. However, in order to correct perspective differences between both cameras, a homography is necessary. The registration of the white-light image to the MR image could utilize the structure of the gyri. Here, edges, curvature and skeletons but also statistical features like mutual information can help to determine the transformation and facilitate image registration.

In summary, more possibilities arise when an additional white-light camera is added. Besides the additional data provided by this device, a feature-based registration is possible. However, this approach necessitates two steps of registration. Possibly both based on feature extraction and matching which is computational expensive. Efficient algorithms as well as state-of-the-art hardware is vital.

Because the goal of this thesis is to provide medical personnel with real time or near real time image fusion, a calibration-based image registration was chosen. No additional white-light camera is needed. In addition, the computational expensive step of feature extraction and matching is obsolete. Existence of a neuronavigation system allows a tracking of instruments and registration of the patient. No manual definition of landmarks is necessary. The following chapter describes design and implementation of our approach including set-up, technologies, mathematical methodologies, plug-in architecture and user interface.



## 4 Design and Implementation

The following chapter describes design and implementation of the presented image fusion application. Starting with the development of the imaging phantom, a description of the phantom's development process, its capabilities and the result is provided. Following, architecture and communication mechanisms of the application are presented. Section 4.2.2 describes the registration process. Sections about image update (4.2.3) and image fusion (4.2.4) are next. After that, additional functionality is described in section 4.2.5. The second last section (4.2.6) describes the user interface. This chapter closes with a scenario on how to use the application (section 4.3).

### 4.1 Phantom Development

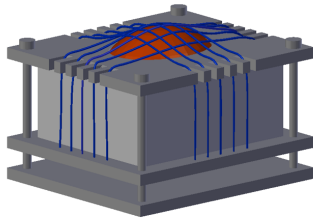
The development of an imaging phantom is necessary to test algorithms during implementation and to evaluate them during and at the end of the development phase. Furthermore, it enables comparison of different algorithms. Functional requirements for the phantom are:

1. Visibility of features in MRI
2. Visibility of features in TI
3. Visibility of features in white-light Imaging
4. Simulation of brain shift
5. Simulation of perfusion
6. Simulation of trepanation

Besides those requirements, it must consist of non-ferromagnetic materials, has to be impermeable to water and should approximate the size of a human head or brain, respectively. The size of the simulated trepanation should resemble a real life trepanation.

The initial prototype, which only exists digitally, fulfils these requirements. Image 4.1a and image 4.1b show the initial prototype. It consists of three sheets and a base body made of plastics (gray). A balloon (red) is located inside the base body and simulates the brain. The top sheet of plastics simulates a trepanation and fixates the tube (blue). The tubes simulate perfusion. Both, tubes and balloon can be

connected to syringes.



(a) Perspective view



(b) Explosion view

Figure 4.1: Early design of the imaging phantom

Several flaws were identified: the fixation of the tubes is not sufficient. Using this design, a repeatable and precise measurement is not possible. Furthermore, the rods as well as the complex internal shape complicate manufacturing. It should be replaced with a better design.

Figure 4.2 shows a prototype of the imaging phantom with a second design. The fixation of the tubes is improved. Their position is now defined via holes in the base body. The exterior design is simplified. The image shows fiducial markers attached to the imaging phantom. With them, registration of the imaging phantom to the BrainLab neuronavigation system is possible.

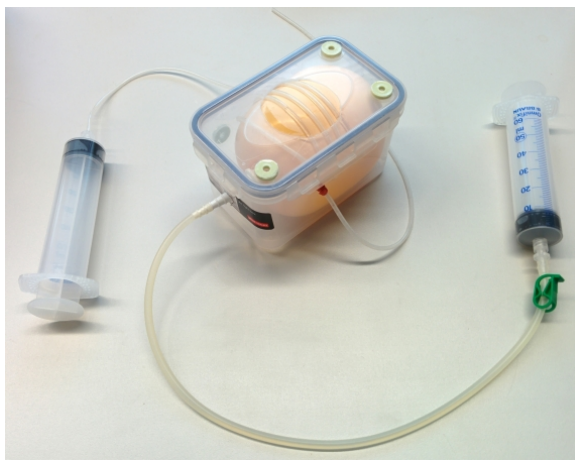


Figure 4.2: Prototype of the imaging phantom

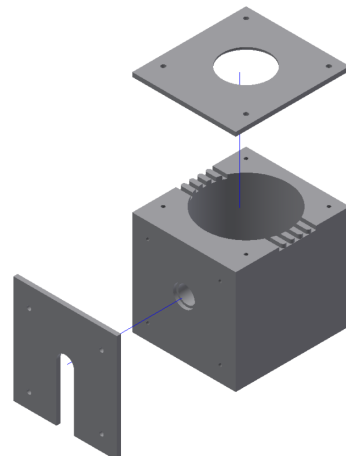


Figure 4.3: Sketch of the final imaging phantom

After several tests with the prototype, the final imaging phantom was developed (see figure 4.3). It consists of three parts of plastics, a balloon, a tube set-up and two syringes as well as necessary connectors. The overall size of the phantom is 104 mm × 119 mm × 100 mm. Its lid has a size of 115 mm × 100 mm × 4 mm. The hole for the simulated trepanation has a diameter of 50 mm. The tube has an external diameter of 3.18 mm and an internal diameter of 1.98 mm. The hardness grade is 50 Shore (A). This is necessary to guarantee that the tube deforms with the expansion of the balloon. All

plastic parts of the casing are made of non-ferromagnetic POM-C. The sheets of plastic are connected to the base body with M4 × 12 mm non-ferromagnetic polyamid screws. The syringes have a filling volume of 60 ml.

The drawings as well as the 3D modelling were done with Autodesk Inventor 2015<sup>1</sup>. Please refer to the appendix (chapter 8) for the drawings. The body parts were manufactured conventionally.

The casing of the imaging phantom simulates a head of a patient. The lid with the circular hole simulates a trepanation. This lid is exchangeable which allows the simulation of different trepanations. The balloon simulates a brain. It is filled with water from the tap. The amount of water in the balloon can be adjusted with one of syringes. With the change of volume, brain shift can be simulated. Here, the balloon extends in the direction of the lid's opening non-linearly. The deformation is bounded by the lid. It can be exchanged and with it, different deformations can be simulated. The attached tube simulates a simple configuration of blood vessels. The body part has five notches on two sides which fixate the position of the tube and prevent dislocation (see fig. 4.5). These notches allow the tube to follow the expansion of the balloon. The notches have no sharp edges in order to prevent a buckling of the tube. If the tube would buckle, simulation of perfusion would not be possible any more. The mentioned hardness grade of 50 Shore (A) helps additionally to prevent buckling. Furthermore, the balloon does not deform because of the tube. It is connected to the other syringe and therefore not in the same hydraulic circle as the balloon. If the tube is perfused with a liquid which has a different temperature than surrounding objects and balloon, a distinct temperature gradient will be visible during thermographic measurements. Furthermore, a cold bolus can be applied.

Fiducial markers are attached to three sides of the imaging phantom. The markers are placed in a way that they are not located in one plane in order to guarantee a good registration accuracy when using a neuronavigation system. The fiducial markers are donut-shaped and visible in MRI and computed tomography. They can be used for initial tests of registration algorithms as well as for the final evaluation.

Figure 4.4 shows the final imaging phantom with balloon, tube and syringes. The opening on the left side is connected to the syringe via a second, bigger tube. It is used for de- and inflation of the balloon with liquid. The sheet of plastic on the front fixates a part which connects the balloon with the tube. It is attached to the body with four screws. The openings at the top of the body part under the top sheet of plastic indicate the openings for the tube which simulates blood vessels. It is laid s-shaped as shown in figure 4.5. The top lid fixates the tube. It is attached to the body part with four screws.

The imaging phantom was imaged with the following MRI techniques: T2-weighted image, fluid-attenuated inversion recovery (FLAIR), magnetization-prepared rapid acquisition with gradient echo

<sup>1</sup><http://www.autodesk.de>

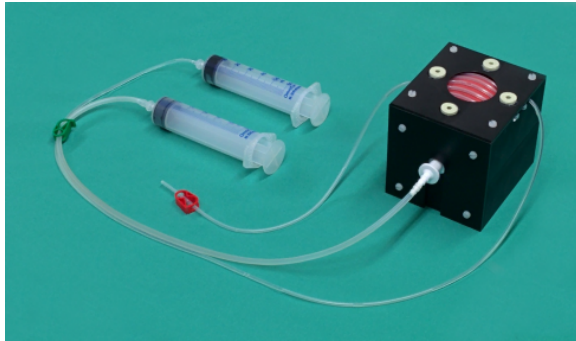


Figure 4.4: Final imaging phantom with connected syringes



Figure 4.5: Top view with removed lid and tube visible

(MP-RAGE). Measurements were performed twice. During the first measurement, the balloon was filled with 500 ml of water. During the second measurement, additional 25 ml of water had been added to simulate brain shift. Figures 4.6, 4.7 and 4.8 show the different images acquired with these techniques.

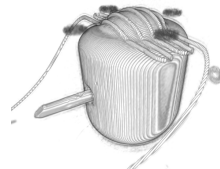
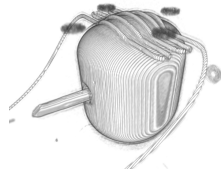


Figure 4.6: MR image of the imaging phantom: T2-weighted (left: default. Right: inflated)



Figure 4.7: MR image of the imaging phantom: MP-RAGE (left: default. Right: inflated)



Figure 4.8: MR image of the imaging phantom: FLAIR (left: default. Right: inflated)

The different images of the imaging phantom show that all desired features are visible: fiducial markers, the tube as well as the balloon. MP-RAGE achieves the best visualisation of the fiducial markers. The water inside the balloon and the tube is visible best in images acquired via T2-weighted and FLAIR. Different properties of water and the material of the fiducial markers prevent MRI from displaying the markers and the water sharp and clear in one single image. This is because water produces a good signal

using T2-weighted techniques like T2-weighted imaging and FLAIR but the fiducial markers can be measured very good with techniques based on T1 relaxation time like MP-RAGE.

Figure 4.9 shows a thermographic image of the phantom. The fiducial markers as well as the tube are visible clearly. A drop of water inside the donut shape leads to a distinct temperature gradient at the fiducial markers. The distinct gradient between tube and balloon results from the inserted water which has another temperature than the surrounding objects

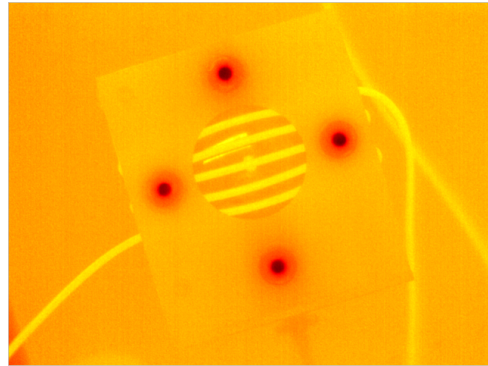


Figure 4.9: Infrared image of the imaging phantom with fiducial markers (black) and tube (yellow) visible

The final imaging phantom fulfils all functional requirements mentioned at the beginning of this section. It is visible in MRI and TI as well as white-light imaging. All parts are non-ferromagnetic. Simulation of brain shift, trepanation and perfusion is possible. Form and structure are similar to the part of the human head which is important during neurosurgery. With these properties, the imaging phantom can be used to test and evaluate image registration and image fusion algorithms.

A part of this chapter is also available in [FMS14].

## 4.2 Amira Plug-In Development

Development of the imaging phantom was one main task. The second main task is the development of an Amira plug-in which performs image fusion of intraoperative thermographic images and preoperative MR image. Figure 4.10 schematically shows the involved devices.

The neuronavigation system (A) tracks the position of the camera (D) via the instrument adapter (C) with respect to the subject (B). The infrared camera acquires images from a region of interest. Both devices are connected to Amira (E). In Amira, a 3D model of the subject and a 2D image representing the IR image exist. Both are, at the beginning, not related. Using the presented plug-in, image registration, image update and image fusion is performed. The result is an image which combines the information from

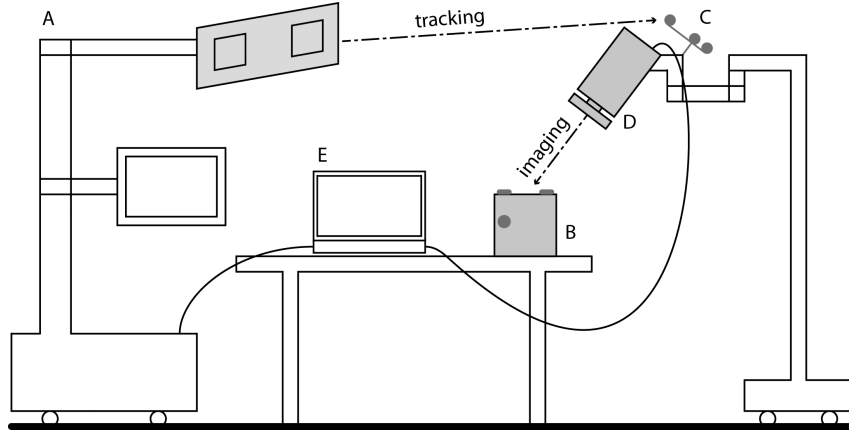


Figure 4.10: Schematic view for intraoperative image fusion. A: neuronavigation system. B: imaging phantom with fiducial markers. C: instrument adapter. D: infrared camera. E: notebook running Amira and receiving tracking and image data.

both modalities. The following sections provide information about the Amira plug-in. Main functional requirements of the image fusion plug-in are:

1. Establishing a connection to BrainLab and receive tracking data
2. Establishing a connection to infrared camera and receive image data
3. Perform image registration of 2D infrared images and 3D MR model
4. Update the 2D image
5. Perform image fusion of 2D infrared images and 3D MR model

Besides these functionalities, the user interface of the plug-in should be intuitive. The default user is not a computer scientist. The architecture should allow extensibility and a later adaptation of the behaviour. During the development process, several additional and necessary functionalities were implemented. Following this agenda, the next section describes the architecture and connection mechanisms. Then sections about image registration (4.2.2), image update (4.2.3) and image fusion (4.2.4) follow. After these sections, additional functionalities (4.2.5) and the user interface (4.2.6) are described. Finally, a typical use case scenario is outlined in section 4.3 to describe the overall usage of the plug-in with all involved components.

#### 4.2.1 Architecture and Connection

As mentioned in section 2.4.1, Amira is based on a modular architecture. Developers are able to extend the software by programming modules. The granularity of those modules is up to the developer. The presented image fusion application is encapsulated in one single module in order to minimize the time

and effort which is necessary to set up image fusion. Furthermore, concurrency errors are minimized because the data is encapsulated. The core architecture of our component is shown in figure 4.11.

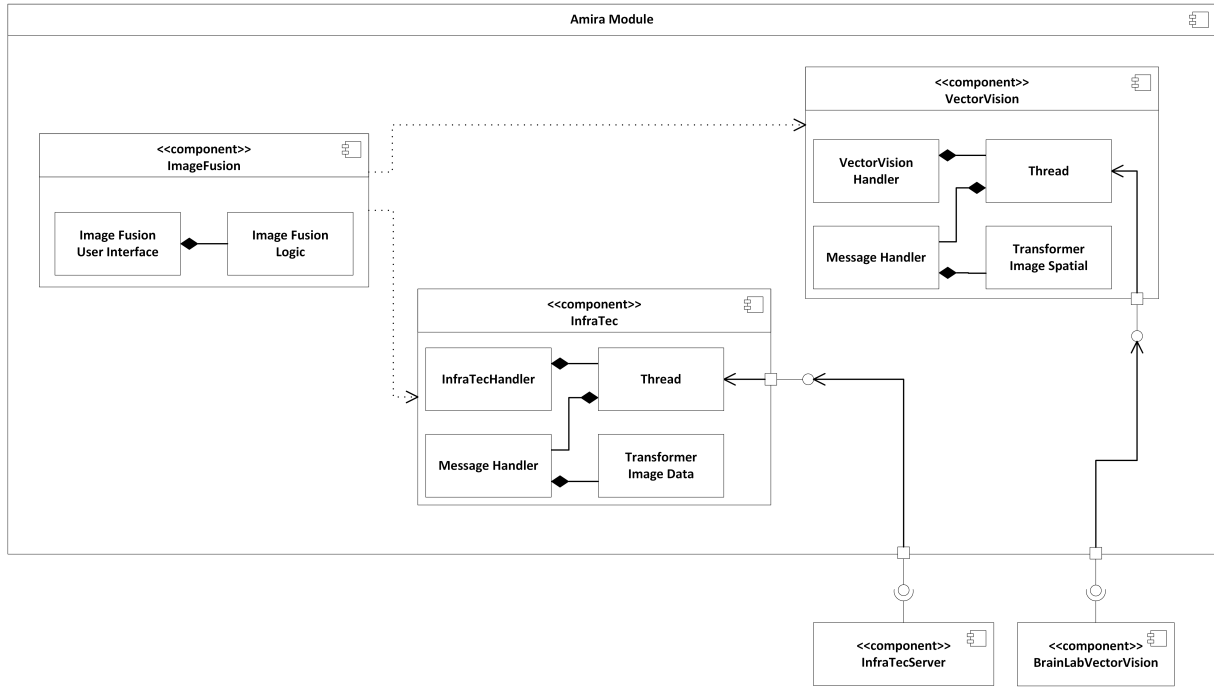


Figure 4.11: Component diagram of the plug-in

The wrapper for the developed software is a module called *Amira Module*. Three main components are identifiable: *Image Fusion*, *VectorVision* and *InfraTec*. Component *ImageFusion* incorporates the user interface elements as well as the application logic. Component *VectorVision* handles the connection to the neuronavigation system, receives and sends messages and updates the spatial data of the 2D image. The component *InfraTec* handles the connection to the infrared camera, receives the image data as well as information about the focal point. The components *BrainLabVectorVision* and *InfraTecServer* represent the software *BrainLab Vector Vision cranial 2.1.1* and the *InfraTecServer*. Both components send data to Amira.

The developed plug-in is multi-threaded. The connections to the infrared camera and the neuronavigation system run in different threads. This allows the system to receive and process spatial and image data concurrently. Furthermore, it is possible to connect to only one device. It is not necessary that both devices send data. Each of the components *VectorVision* and *InfraTec* runs in its own thread. They have a similar internal structure. Figure 4.12 depicts the abstract structure with core methods of these components. *AbstractHandler* is responsible for the global control of the component. It starts and stops the thread *m\_thread*. *AbstractThread* connects and disconnects to a device (neuronavigation system or infrared camera) via OpenIGTLLink. It starts or stops processing of data. If no connection is established, the thread will not run. The method *processMessage()* in *AbstractMessageHandler* is invoked each

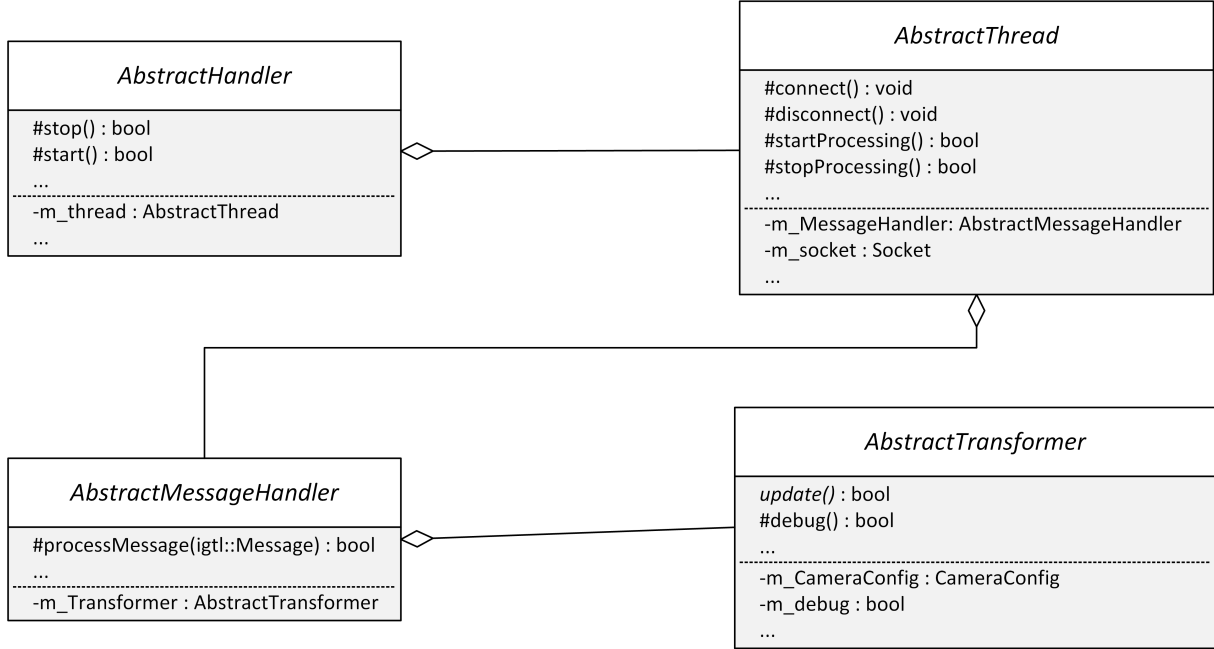


Figure 4.12: Class diagram of one component (VectorVision or InfraTec)

time a message arrives. From here, `update()` or `debug()` in *AbstractTransformer* is called. This class actually changes data and properties of the 2D image. The 3D image is not changed at all during image fusion. As shown in figure 4.11, there are currently two types transformers: *Transformer Image Data* and *Transformer Image Spatial*. The former is responsible for updating colour values of the 2D image. The latter changes position, size and orientation of the 2D image. *m\_CameraConfig* provides information about the infrared camera and the attached lens. Please see section 4.2.5.3 for more information about camera configuration.

Figure 4.13 shows a sequence diagram of the involved threads and how they update the model of the 2D image. When the user starts Amira, makes necessary configuration and starts image fusion, both threads are started. *VectorVision:Thread* tries to establish a connection to BrainLab Vector Vision cranial 2.1.1. The *InfraTec:Thread* is responsible for establishing a connection to the *InfraTec:Server*. After the connections have been established, the threads receive messages and process them. They update the 2D image represented by *2DImage*. The *VectorVision:Thread* controls the spatial data and performs image registration. The *InfraTec:Thread* controls the image data and performs image update and the main thread, represented by *Amira:Thread*, updates the viewer periodically. This is realised with a mechanism called *time-out method* provided by Amira. A time-out method is executed periodically by Amira. Using this mechanism, `refreshViewer()` is executed periodically. During update, the *2DImage* is accessed and the viewer is updated with the gathered data. If, for any reason, the connection to the neuronavigation system or to the infrared camera fails, the responsible thread will be stopped. The same will happen if the

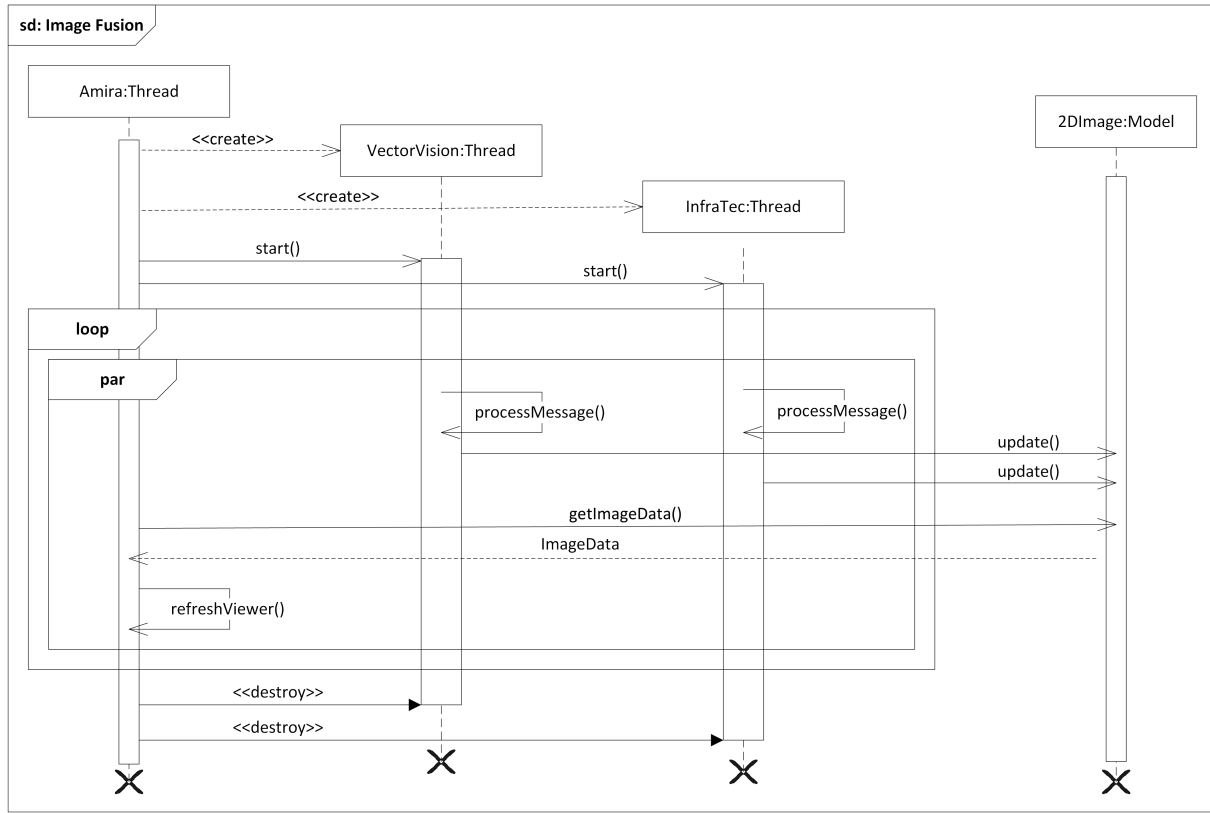


Figure 4.13: Simplified sequence diagram showing the life-cycle of the image fusion plug-in

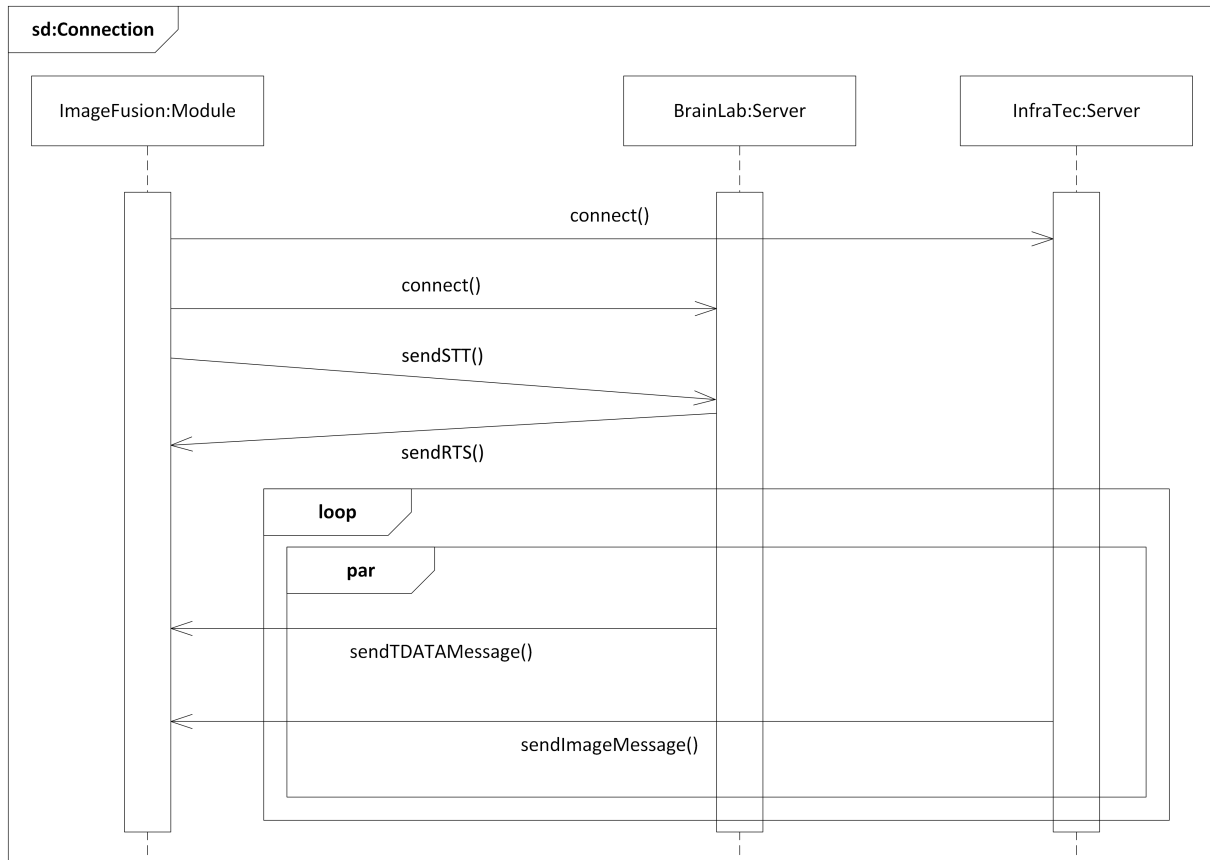


Figure 4.14: Messages during image fusion

user stops image fusion. However, both threads can work independently and can be started and stopped without affecting the other one.

The connection between the Amira plug-in, the neuronavigation and the infrared camera is based on OpenIGTLink. A brief description of the core concept of OpenIGTLink is provided in section 2.4.3. Communication of OpenIGTLink is based on messages and sockets. The framework provides some custom messages which are sufficient for most cases. A single message in OpenIGTLink consists of a header and a body. The header contains metadata about the device which has sent the data, the size of the body and the type of message. For example, the data send by the neuronavigation system uses a predefined format for tracking data called *TDATA*<sup>2</sup>. *TDATA* messages provide names and transformation matrices of all tracked instruments. OpenIGTLink also provides a default message format for images, called *IMAGE*<sup>3</sup>. The header of this message type contains the name of the imaging device as well as information about size and data type of the attached image. The actual image data is stored in the body. For the developed application, an additional field was necessary. *MYIMAGE* message was created which extends the *IMAGE* message. A field called *focusValue* was added. This focus value is necessary to perform image registration.

The overall communication scheme is described by figure 4.14. After the connections have been established, the *InfraTecServer* component starts to send messages immediately. *BrainLab VectorVision cranial 2.1.1* however does not start sending messages until a special *STT* messages was sent to the server by the client. This message is confirmed via a *RTS* message. This allows the user to stop streaming but keeps the connection alive. Unfortunately, this mechanism is not provided by the *InfraTecServer*.

This implemented communication mechanism enables the user to start and stop streaming of spatial data. More important, it provides a mechanism to change the transmission frequency. Because the *InfraTecServer* component lacks this functionality, it is not possible to change the transmission frequency without terminating the connection. The architecture of the plug-in makes it easy to adapt the InfraTec component in a way that it supports this behaviour. In general, the modular architecture enables developers to extend and change the functionality of the image fusion plug-in easily. For example, a server which sends an RGBA image instead of an array of scalar values can be integrated easily by changing the *TransformerImageData*. The usage of OpenIGTLink, an open-source protocol designed for medical applications like BrainLab, ensures that it is as easy as possible to connect the application with other components. Hence, the introduction of yet another protocol has been avoided. The design of the

---

<sup>2</sup><http://www.na-mic.org/Wiki/index.php/OpenIGTLink/ProtocolV2>Type/TrackingData>,

last accessed: 2014-11-03

<sup>3</sup><http://www.na-mic.org/Wiki/index.php/OpenIGTLink/ProtocolV2>Type/Image>,

last accessed: 2014-11-03

components with *AbstractHandler*, *AbstractThread*, *AbstractMessageHandler* and *AbstractTransformer* applies the concepts *separation of concerns* as well as *divide and conquer*. This makes it easy to extend and change behaviour. With the knowledge of communication and architecture, the following chapter describes the process of image registration.

### 4.2.2 Image Registration

With the knowledge and information about the architecture and components, it is now possible to describe the image registration algorithm. The Amira plug-in connects to the BrainLab VectorVision neuronavigation system. This device tracks position and orientation of the IA. The IA is attached to the camera. Therefore, data of the IA can be seen as data from the camera. Image registration also uses some data sent by the thermographic camera. Figure 4.15 describes the nature of our method according to the presented

| Registration Methods |                              |                          |                          |                |                         |                     |              |                     |
|----------------------|------------------------------|--------------------------|--------------------------|----------------|-------------------------|---------------------|--------------|---------------------|
| Dimension            | Nature of Registration Basis | Nature of Transformation | Domain of Transformation | Interaction    | Optimization Procedure  | Involved Modalities | Subject      | Object              |
| Spatial and temporal | Extrinsic                    | Rigid                    | Local                    | Interactive    | Parameters computed     | Monomodal           | Intrasubject | Head                |
| Spatial only         | Intrinsic                    | Affine                   | Global                   | Semi-automatic | Parameters searched for | Multimodal          | Intersubject | Thorax              |
|                      | Non-image based              | Projective               |                          | Automatic      |                         | Modality to model   | Atlas        | Abdomen             |
|                      |                              | Curved                   |                          |                |                         | Patient to model    |              | Pelvis and perineum |
|                      |                              | Non-rigid                |                          |                |                         |                     |              | Limbs               |
|                      |                              |                          |                          |                |                         |                     |              | Spine and vertebrea |

Figure 4.15: Classification of the presented registration scheme according to the taxonomy introduced in section 3.2.2.1

taxonomy. The implemented image registration algorithm deals with temporal and spatial data. It is calibration-based and therefore non-image based. Furthermore, it uses an affine transformation. In other words, involved transformations are rotation, translation and scaling. The image is transformed globally and semi-automatic. Semi-automatic does not only mean that the user has to start and stop registration, but he is also able to adjust registration. The transformation parameters are computed from the camera parameters and data from the neuronavigation system. The algorithm registers multimodal data: the 3D MR model and the IR image. Both datasets are from the same patient and show the brain or a part of the brain, respectively.

Figure 4.16 shows the data objects in Amira without any modifications. Both images are located at the

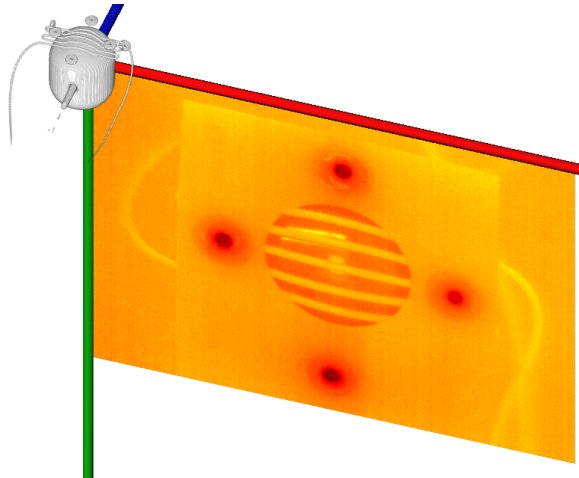


Figure 4.16: Amira screenshot with unmodified data object: 3D image of the phantom, the 2D infrared image and the world coordinate system

origin of the world coordinate system. The size of the 3D image is in mm and provided by the DICOM<sup>4</sup> data. However, the 2D image has not the correct size.

To perform image registration in Amira, two preliminary steps are necessary: First, the calibration of

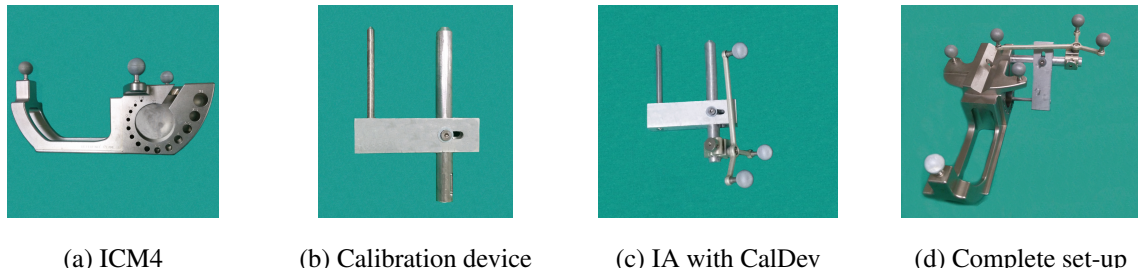


Figure 4.17: Necessary devices for the calibration of the instrument adapter.

the IA to the neuronavigation system. This is necessary because the neuronavigation system needs to know a reference point of the IA. The calibration is performed with the BrainLab *ICM4* calibration tool (see figure 4.17a) and an additional calibration device (CalDev, see figure 4.17b). CalDev has especially been developed for this purpose during development of the application. The registration process starts automatically when the IA is exposed to the neuronavigation system. Then, the IA has to be attached to the CalDev (see fig. 4.17c) which has to be attached to the *ICM4* (see fig. 4.17d). BrainLab VectorVision performs calibration of the IA autonomously when the *ICM4* does not move. After a successful calibration, the IA has to be attached to the IR camera.

Second, registration of the subject to the neuronavigation system. In order to do this, the data set has to be imported into the neuronavigation system and positions of the fiducial markers have to be defined.

<sup>4</sup><http://dicom.nema.org/>, last accessed: 2014-11-04

This is done with *iPlanNet 3.0* (please see section 2.4.2 for more information). After the positions of the markers are known to the neuronavigation system, the registration process can be performed by touching every fiducial marker of the subject with the pointer. BrainLab VectorVision automatically recognizes a marker configuration. After every fiducial marker has been touched, the subject is registered. All spatial data which arrives from the neuronavigation system is now in the coordinate system of the subject. This includes information send via *TDATA* messages.

After calibration of the IA and registration of the subject, all necessary prerequisites for the calibration-based image registration in Amira are fulfilled. Please note that "calibration-based" does not refer to the calibration of the IA but to the calibration matrix  $M_c$  explained in the following paragraphs. To perform registration, the Amira image fusion plug-in connects to the neuronavigation system and receives spatial data of the tracked instruments. The objective is to transform the 2D image to the position and orientation of the infrared camera's sensor array. This step is represented by  $I'_m = T \cdot I_m$  where

$$T = M_a \cdot M_c \cdot M_{BrainLab} \quad (4.1)$$

The matrix  $T$  represents the final transformation and is composed of  $M_{BrainLab}$ ,  $M_c$ ,  $M_a$ .  $M_c$  represents the calibration and  $M_a$  additional transformations.  $M_{BrainLab}$  consists of the position and direction of the IA delivered by the neuronavigation system. Using only this matrix, the image would have the same position and orientation as the reference point of the IA attached to the thermographic camera (see figure 4.18). Because there is a difference between the location and orientation of the IA  $\vec{v}$  and the position

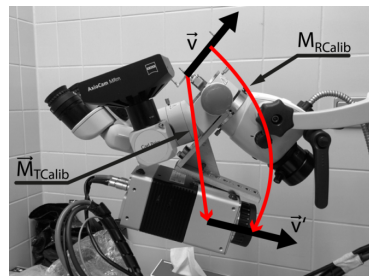


Figure 4.18: Spatial difference between IA and camera.

and orientation of the sensor array  $\vec{v}'$ , a calibration is necessary. This calibration is represented by  $M_c$ :

$$M_c = M_{TCalib} \cdot M_{RCalib} \quad (4.2)$$

The calibration parameters are determined using the following steps: *Calibration: Rotation* and *Calibration: Translation*. They are explained in the following paragraphs.

**Calibration: Rotation** To determine rotational parameters, two steps are necessary. First, the infrared camera has to be positioned in such a way, that it points vertically downwards. The correct

orientation can be ensured by controlling the coordinates of three point pairs at the infrared camera. The point pairs are indicated in figure 4.19. If the x-coordinates of point pairs  $P_1$  and  $P_3$  as well as

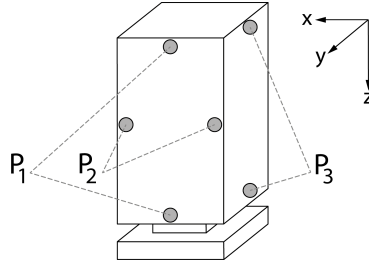


Figure 4.19: The indicated point pairs are touched with the pointer and their coordinates are used to assess the orientation of the infrared camera.

the y-coordinates of  $P_1$ ,  $P_2$  and  $P_3$  are the same (within the pairs), the infrared camera points vertically downwards. In the second step, the 2D infrared image visible in Amira was transformed manually so that the image normal points vertically downwards. The result are rotation parameters which specify the directional difference between the axis of the IA and the surface normal of the image sensor whereas  $\alpha = 64.1728$ ,  $\beta = -0.0657634$  and  $\gamma = 0.66133$  are the euler angles for the x-, y- and z-axis. The final matrix is outlined in equation 4.3.

$$M_{RCalib} = \begin{pmatrix} 1 & 0 & 0 \\ 0 & \cos\alpha & -\sin\alpha \\ 0 & \sin\alpha & \cos\alpha \end{pmatrix} \begin{pmatrix} \cos\beta & 0 & \sin\beta \\ 0 & 1 & 0 \\ -\sin\beta & 0 & \cos\beta \end{pmatrix} \begin{pmatrix} \cos\gamma & -\sin\gamma & 0 \\ \sin\gamma & \cos\gamma & 0 \\ 0 & 0 & 1 \end{pmatrix} \quad (4.3)$$

**Calibration: Translation** The translation parameters were determined using the following technique: The infrared camera has to be positioned so that it shows the imaging phantom. The image shows the fiducial markers as well as the tube of the imaging phantom. Both are visible in the MR image. After the rotational difference has been eliminated, it is possible to translate the image so that the features of the infrared image and the MR model overlay perfectly:

$$M_{TCalib} = (0, -148, -255)^T \quad (4.4)$$

With  $M_{TCalib}$  and  $M_{RCalib}$ , the calibration procedure is complete and the reference point of the IA is transformed to the position of the camera's sensor array. To ensure that the calibration is precise, it is necessary to be very careful during the calibration procedure. Neglectfulness during the mentioned steps results in an inaccurate image registration and image fusion. The calibration parameters can be adjusted via the user interface while the application runs to compensate errors.

**Scaling** After the calibration has been applied to the image, the orientation and position is correct. Next, scaling is necessary. The infrared camera is able to adjust its focus by changing the distance between the sensor array and the lens via a step motor. The position of the camera does not change but only the position of the focal point. If the position of the camera would change, the distance between camera and subject could be calculated with spatial data delivered by the neuronavigation system. To get the distance and with it the size of the image, the application utilizes the *focus value FE*. The *InfraTecServer* sends the focus value. With *FE*, it is possible to calculate the distance of the focal point and with it the distance between sensor array and subject. The correlation between focal point and distance is described by equation 4.5 whereas  $f(FE)$  is the distance in cm.  $f(FE)$  is based on the rational function  $\frac{1}{x}$ . With a measurement which delivered distances in cm to the according focus value, parameters  $HH = 1.46$ ,  $FAC = 123570$  and  $INF = 2000$  were determined via linear least squares [LH95] by another research group.  $INF$  represents the maximum observable distance,  $HH$  is an approximation of the lens' front principal point.  $FAC$  has no physical representation.

$$f(FE) = HH + \left( \frac{FAC}{FE} - INF \right) \quad (4.5)$$

Figure 4.20 shows the correlation between the focus value and the distance. The correlation is almost linear for distances smaller 30 cm. If the distance between subject and camera is greater than 30 cm, the correlation is non-linear. With the distance between subject and camera, calculation of the image size is

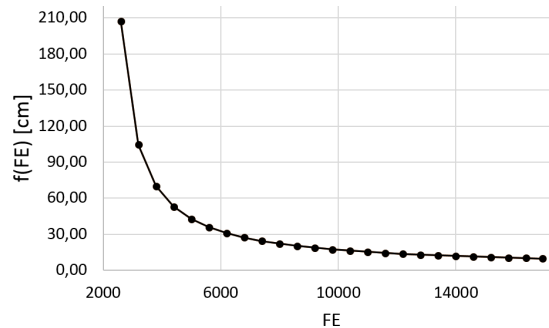


Figure 4.20: Correlation between focus value *FE* and distance  $f(FE)$  for the InfraTec *VarioCAM HD head 680 S / 30mm \*\*\*MEDICAL \*\*\**

possible. To do this, the field of view is necessary. The field of view describes the vertical and horizontal opening angles of the camera's area of inspection. The field of view depends on the applied lens. For the *VarioCAM HD head 680 S / 30mm \*\*\*MEDICAL \*\*\** and the default lens, the horizontal value is  $FOV_H = 29.9^\circ$  and the vertical value is  $FOV_V = 22.6^\circ$ . Using this values, the extends of the acquired image can be calculated with

$$d_h = 2 \times \sin(FOV_H) \times f(FE) \quad (4.6)$$

$$d_v = 2 \times \sin(FOV_V) \times f(FE) \quad (4.7)$$

where  $d_v$  and  $d_h$  are the extents of the observed area and therefore the 2D IR image. With the results from equation 4.6 and 4.7 it is possible to calculate a scaling factor for the transformation. For this, it is necessary to know that the image in Amira has a default pixel size of 1 mm. In other words, the image delivered by the infrared camera has width of  $640 \times 1 \text{ mm} = 640 \text{ mm}$  and a height of  $480 \times 1 \text{ mm} = 480 \text{ mm}$ . With these values, a scaling matrix can be defined as shown in equation 4.8

$$M_{Scale} = \begin{pmatrix} \frac{d_h}{640 \text{ mm}} & 0 & 0 & 0 \\ 0 & \frac{d_v}{480 \text{ mm}} & 0 & 0 \\ 0 & 0 & 1 & 0 \\ 0 & 0 & 0 & 0 \end{pmatrix} \quad (4.8)$$

**Coordinate transformation** The application uses two additional transformations to ease handling of the 2D image. They are combined in  $M_a$ . First,  $M_{TranslateCenter}$  translates the origin of the image from the corner to its centre. After this translation, the centre of scaling and rotation is at the centre of the image. Second, the image is rotated  $180^\circ$  around the global x and y Axis with a matrix  $M_{RotXY180}$ . This is necessary to align both coordinate systems.

The final necessary transformations are:

- Spatial data:  $M_{BrainLab}$  and  $M_{Scale}$
- Calibration:  $M_{TCalib}$  and  $M_{RCalib}$
- Additional:  $M_{RotXY180}$  and  $M_{TranslateCenter}$

The first two transformations adjust the position according to the spatial data. Calibration compensates the offset between IA and sensor array. The additional transformations adjust the centre of rotation and scaling via a translation and equalize the coordinate systems. These transformations are applied using the following order:

$$T = M_{RotXY180} \cdot M_{TranslateCenter} \cdot M_{Scale} \cdot M_{TCalib} \cdot M_{RCalib} \cdot M_{BrainLab} \quad (4.9)$$

The calculation and application of  $T$  is performed in *TransformerPosition* of the *VectorVision* component. Please note that the distance between camera and subject can be calculated but not the distance between focal point and camera. Therefore, the scale factor can not be calculated. Without the correct focus value  $FE$ , a correct image registration is impossible. In other words, it is necessary to have a connection to the infrared camera as well as the neuronavigation system. To overcome this flaw, a user interface element allows the manual specification of the focus value.

The transformation of the 2D image with  $T$  places the infrared image in Amira at the very location where the sensor array of the thermographic camera is located in the real world. The result is shown in the left image of figure 4.21. This allows image fusion as indicated in the right image.

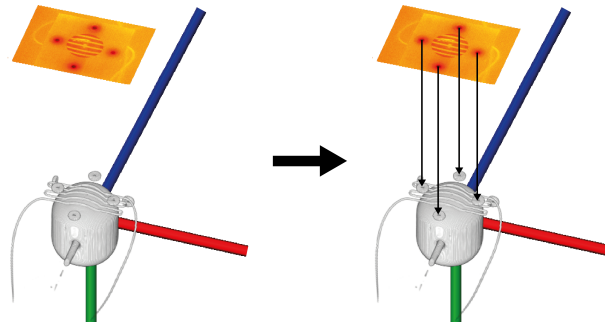


Figure 4.21: Amira view with modified data objects (image of the phantom, transformed 2D infrared image and coordinate system) indicating the result of the registration

### 4.2.3 Image Update

Not only the position and orientation of the 2D image need to be updated but also the content of the image. To do this, the Amira plug-in is able to connect to the *InfraTecServer* using OpenIGTLLink and receive image data. As mentioned before, this connection also provides the focus value for image registration. The incoming data should be processed in near real time at best but at least with 1 frame per second.

The *InfraTecServer* sends *MYIMAGE* messages and is responsible for controlling the transmission frequency. Each *MYIMAGE* message contains one single image and consists of a header and a body. The header contains, besides other metadata, the dimensions of the image and the data type of the attached data. Images send by the *InfraTecServer* have the dimensions of  $640 \times 480 \times 1$  pixel. Therefore, one image consists of  $640 \times 480 = 307200$  unsigned short integer values. The size of one unsigned short integer is 2 Byte. This results in a body size of  $307200 \times 2 = 600$  kB.

The *InfraTecThread* receives the incoming image messages and invokes the processing in the *InfraTecMessageHandler*. Here, a CRC check is performed and the focus value is updated. Then, the message is forwarded to the *TransformerImageData*.

The body of the message consists of a data array which contains the image. It has the size of  $640 \times 480 = 307200$  values. One value represents the temperature in Kelvin times 100. For example, 29315 is transformed to  $293.15^{\circ}\text{K}$  and finally to  $20^{\circ}\text{C}$ . Every value of the data array is converted to a temperature value in degree Celsius. With these values, the colour is determined. The colour is represented by the structure **COLOUR** which has four values: `struct { double r, g, b, a; } COLOUR;`. Two possible techniques for conversion are provided by the application: `getColorFromFormula()` for using a function for custom conversions and `getColorFromMap()` which uses a lookup table. The first solution allows conversion from temperature values to arbitrary colour values. However, it requires more operations

than the second solution. Here, a simple lookup in a one-dimensional array is performed.



Figure 4.22: Colourmap applied to the incoming data: heated object scale

The colourmap applied in our application is *Heated Object Scale* (or *hot / iron*) shown in figure 4.22. Cold objects appear black. Objects with a higher temperature are more red, yellow or white, respectively. This colourmap is, according to Schumann et al. [SM00], more intuitive than other colourmaps like the rainbow colourmap. The colours are similar to the colours of a black object which has been heated. Furthermore, it is more easy for most users to distinguish hotter from cooler areas. This is not only because of the chosen colours but also because the human eye is very sensitive to differences in the brightness of the colours orange and yellow.

---

**Algorithm 1:** From *value* to COLOUR

---

**Input :** value, min, max, sizeOfColourmap

**Output:** COLOUR

```

begin                                                 1
    result ← value/100 ;                           2
    result ← getDegreesCelsius(result) ;           3
    result = normalize(result, min, max) ;          4
    colorIndex = result * sizeOfColourmap ;        5
    colour = colourmap[colorIndex] ;                6
    colour = colour * 255 ;                         7

```

---

Algorithm 1 shows the conversion of incoming unsigned short integer value to outgoing colours. The incoming value is first divided by 100 than transformed from degree Kelvin to degree Celsius. The resulting temperature value is normalized and multiplied with the size of the colourmap. With this index, the colour for the temperature is retrieved. The values of the colourmap are also normalized. This means that, the red, green and blue values range from zero to one. In order to get values between 0 and 255 a multiplication with 255 is performed. Minimum and maximum values are controlled manually via a user interface element. Transparency of the image can be controlled via a user interface element.

With knowledge on how the colours are calculated, it is now possible to update the image. For each value of the incoming message, a colour is calculated. The values of the colour are then inserted into an unsigned integer array with the size of  $640 \times 480 \times 4 = 1228800$  elements. For each pixel four integer values are stored representing red, green, blue and alpha. The first solution was to simply update

the corresponding data array of the model in serial. This approach proved to be bad because the method *refreshViewer()* accessed a model which has not been updated completely. This led to rendering artefacts. To overcome this issue, a double buffering mechanism was implemented as outlined by algorithm 2. Each time a new *MYIMAGE* message arrives, another buffer is active. This buffer is updated with new

---

**Algorithm 2:** Double buffering for image data
 

---

**Data:** MYIMAGE message with image data

**Result:** Image pointing to the completely updated buffered array

```

if last_buffer_was_a then                                1
    updateImage(buffer_b);                               2
    2DImage ← buffer_b;                                3
    last_buffer_was_a ← false;                           4
else                                                 5
    updateImage(buffer_a);                               6
    2DImage ← buffer_a;                                7
    last_buffer_was_a ← true;                           8
  
```

---

colours. Double buffering ensures that the thread which is responsible for updating the image always uses a complete and up-to-date buffer. Please keep in mind that this very thread is not the thread which updates the buffer.

The current approach does not use a multi-threaded divide-and-conquer approach to update the image but does it serial. Further improvements to speed up the image update can will be achieved if the data array is split up in several parts and the processing is done data-parallel. The calculation of the *COLOUR* is invoked in *TransformerImageData* and performed in a separate class called *ColourMap*. The complete update of the image data is the responsibility of the *InfraTec* component.

The presented algorithms update the image with data from the infrared camera, send by the InfraTec-Server. Images arrive in form of *MYIMAGE* messages consisting of header and body. The body contains an array of temperature values. These temperature values are transformed into colours. The resulting colours are put into a special buffer. When the buffer is completely updated with all new colours, the model is updated. Double buffering prevents rendering artefacts.

#### 4.2.4 Image Fusion

The final task of the plug-in is the actual image fusion. Image registration of the 2D image and the 3D image as well as the update of the 2D image with the streaming data are prerequisites which are

necessary to project the 2D image onto the 3D image. Image fusion merges spatial information of the 3D MR image and temperature information of the infrared image. In section 3.2.3 methods for image fusion have been discussed. The presented application performs image fusion via texture mapping. The texture mapping mechanism is provided by Amira. In order to understand image fusion, it is necessary

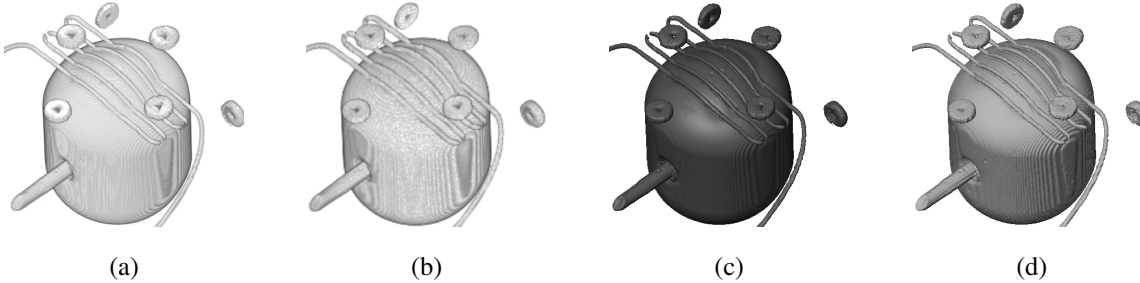


Figure 4.23: Different visualization types provided by Amira.

4.23a: Voltex. 4.23b: Volren. 4.23c: Isosurface. 4.23d: SurfaceView

to dive a little deeper into the principles of Amira. The 3D data object in Amira can be represented with various visualization techniques. First, *Voltex* or *Volren*, which are volume rendering techniques. Second, *Isosurface* and *SurfaceView*, which only visualize the surface of the 3D data model. Figure 4.23 shows different visualization techniques. They have different levels of detail and require a different amount of computational effort. The following paragraphs briefly assesses possibilities of image fusion using these techniques. The approaches are assessed again mesh complexity and rendering quality. Please note that *Volren* and *Voltex* do not possess an inherent mechanism for texture mapping. *Isosurface* and *SurfaceView* offer the possibility to assign a texture or a so-called *Colorfield* or a texture.

**Isosurface, Colorfield** The first solution uses an isosurface from the original 2D data. The Isosurface can have a *Colorfield*. With a *Colorfield*, the 2D image is fused with the 3D image using correct transparency values and without further means. However, the result is not satisfactory. The fused image shows artefacts and the high resolution provided by the infrared camera is lost due to interpolation. Figure 4.24a shows an *Isosurface* of the imaging phantom with the 2D image as *Colorfield*.

**Isosurface, Texture** An improved solution is to use an isosurface with a texture instead of a *Colorfield*. Here, details of the infrared image are not lost and visualization is faster. Set-up does not require more modules or steps as the previous solution using a *Colorfield*. However, this mode does not support transparency. The texture is applied to the whole model despite the actual size of the 2D image. This leads to unsatisfactory results. Figure 4.24b shows an isosurface of the imaging phantom with the 2D image as a texture.

**Isosurface, Texture, Voltex** An improvement of this approach is to use an additional visualization of the 3D model. If the borders of the texture have a single colour and the texture mode is set to *clamp* every pixel of the *Isosurface* which is not covered directly by the texture gets assigned this very colour. Without further means, the structure of the *Isosurface* is lost. However, the introduction of an additional *Voltex* adds structural details of the brain. The set-up is more complex than the other two methods. The introduction of the *Voltex* slows execution of the application down. Figure 4.24c shows an *Isosurface* of the imaging phantom with the 2D image as a texture and an additional *Voltex*.

**SurfaceView, Texture, Isosurface** The first three methods that have been tried and evaluated during the development process do not produce satisfying results. An approach which uses an *Isosurface* with a texture and a *SurfaceView* solves the problems mentioned above. This solution requires the extraction of an *Isosurface* from the MR image. Amira provides a mechanism to extract surface patches from the *Isosurface*. This surface patch can be visualized as a *SurfaceView*. Finally, this *SurfaceView* can have a texture. Amira allows the user to set the rendering mode of the *SurfaceView* to *transparency*. Using this feature, all transparent pixels are drawn with the assigned transparent value. This is important because the *clamp* mode of the texturing algorithm is enabled. This mode can not be disabled. During image update described in section 4.2.3, the border of the image is set to be fully transparent. Using this approach results in the desired solution: the visible *SurfaceView* shows only the infrared image as the texture of the 3D MR image. Figure 4.24d shows an *Isosurface* and a *SurfaceView* of the imaging phantom with the 2D image as a texture of the *SurfaceView*. This solution requires an additional element during set-up but has the best result of all proposed solutions. Besides that, it is possible to display only the *SurfaceView* as well as combine it with a *Voltex* or *Volren*.

This solution provides a fast mechanism which does not decrease level of detail because of interpolation as the *Colorfield* does. Transparent values are visualized correctly. Generation of the *Isosurface* as well as the *SurfaceView* are mandatory for visualization. It can be done preoperatively. The overall set-up from loading data to starting image fusion takes only a few minutes. The final Amira mesh has a structure as shown in figure 4.25. *BrainData* and *ThermoData* are input data objects. The module *ImageFusion* performs registration, update and fusion. *Isosurface* visualizes the subject. *SurfaceView* is extracted from the *Isosurface* and has *ThermoData* as texture. With this configuration, a near real-time image fusion is possible.

Section 3.2.3 mentions the problem of perspective which is introduced by the infrared camera and the fact that it is based on the model of a pinhole camera. To overcome this problem, the plug-in offers the possibility to align the viewport with the sensor array. In other words, the viewing direction of the virtual camera is set to the same direction as the surface normal of the IR camera's sensor array.

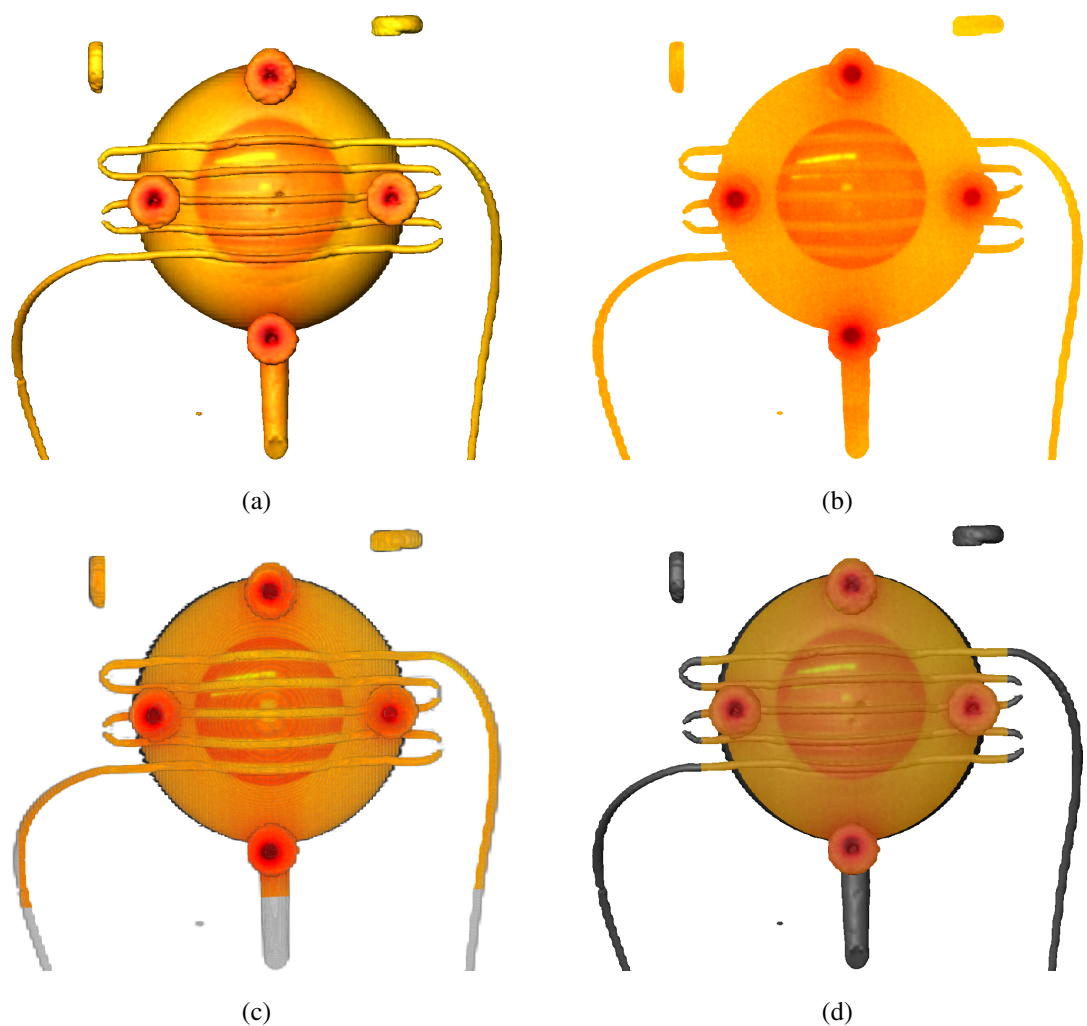


Figure 4.24: Image fusion with the provided visualization and fusion techniques. 4.24a: Isosurface with an attached Colorfield. 4.24b: *Isosurface* with texture. 4.24c: *Isosurface* with texture and additional *Voltex*. 4.24d: *SurfaceView* with texture and *Isosurface*

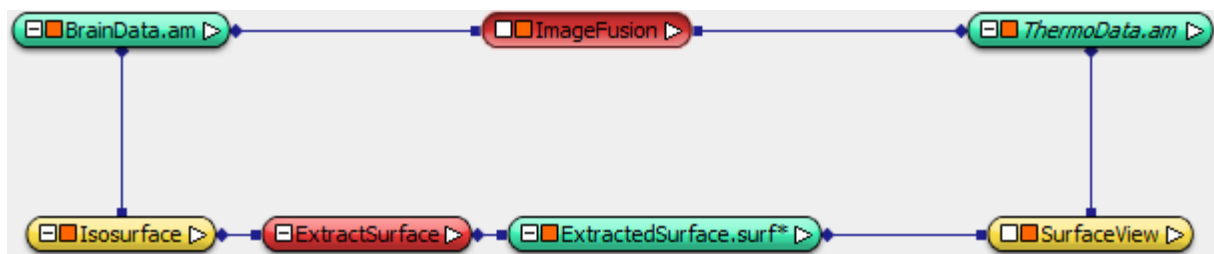


Figure 4.25: Amira mesh showing the necessary elements for image fusion: ThermoData, BrainData, *Isosurface*, *SurfaceView* and *ImageFusion* with the necessary connections.

Besides that, Amira provides the possibility to use an orthogonal virtual camera. Using both approaches, medical personnel is able to analyse temperature distributions at the surface of the brain seeing only minimal interpolated values introduced through texturing and with only small errors introduced through the pinhole model of the camera.

With the proposed approach for image fusion, the required core functionalities have been realized. The connections to the neuronavigation system and the *InfraTecServer* are established by the plug-in. It performs image registration using a calibration-based approach with data from the neuronavigation system. The 2D image in Amira is updated with temperature data arriving via stream from the IR camera. Finally, image fusion merges both images using an *Isosurface* and a *SurfaceView* with a texture. The following sections outline further functionality which is necessary to use and control the plug-in and analyse data.

## 4.2.5 Additional Functionality

### 4.2.5.1 Record and Replay

For evaluation and analysis, all incoming data (images and positions) can be written to a binary file. This file contains the unmodified values, meaning data before image registration and image update. The binary file has two main building blocks. One for image data (see listing 4.1) and one for spatial data (see listing 4.2). File output can be disabled or enabled by the user. A server application based on

|                                |   |
|--------------------------------|---|
| StartImage                     | 1 |
| focusValue                     | 2 |
| timestamp                      | 3 |
| image data in binary format... | 4 |
| EndImage                       | 5 |

Listing 4.1: Structure of an image data block

|  |   |
|--|---|
| StartPosition                                  | 1 |
| timestamp                                      | 2 |
| $M_{BrainLab}$ as a float array (row-order)... | 3 |
| EndPosition                                    | 4 |

Listing 4.2: Structure of spatial data block

OpenIGTLink is able to read these files and resend data to the Amira plug-in. It simulates *BrainLab VectorVision cranial 2.1.1* and *InfraTecServer* using the same connection mechanism. The application offers the possibility to replay either images or spatial data or both. The frame rate can be controlled during start-up. To ease the handling of the acquired data, the incoming data stream is stored in 100 MB

files. This enables developers to test different algorithms with the same data. Furthermore, it enables researchers as well as medical personnel to analyse intraoperative thermographic images postoperatively.

#### 4.2.5.2 Pointer Tracking

The pointing device (see figure 2.6 in section 2.3.1) which comes with the neuronavigation system can help to interact with data. The neuronavigation system tracks the markers attached to the device and calculates the position of the pointer's tip. The position can be accessed via the same connection used for image registration. With the transformation shown in equation 4.10, the position is transformed to the coordinate system of the MR image. Please note that the transformation  $T_{Pointer}$  does not contain the calibration but only the coordinate transform  $M_{RotXY180}$  and the BrainLab tracking data  $M_{BrainLab}$ .

$$T_{Pointer} = M_{RotXY180} \cdot M_{BrainLab} \quad (4.10)$$

The position of the pointer's tip is not only useful for intraoperative data analysis but also for evaluation of image registration algorithms. The Amira plug-in offers the possibility to display a sphere at the position of the pointer's tip. Furthermore, the position can be written to a file for further analysis and later calculations. Figure 4.26 shows the imaging phantom with a grey sphere indicating the position of the tip. A user interface element allows the adjustment of the sphere's size. The update of the position can be stopped if necessary. The coordinates are printed on the screen.

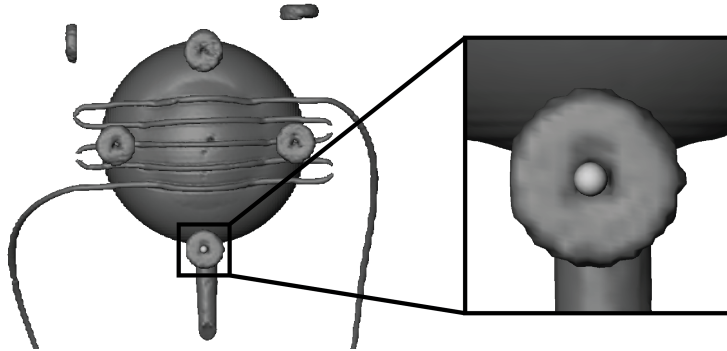


Figure 4.26: Tip of the pointer represented by a sphere.

#### 4.2.5.3 Camera Configuration

As mentioned in section 4.2.2, the plug-in needs some information about the applied infrared camera to perform a correct image registration:  $HH$ ,  $FAC$ ,  $INF$ ,  $FOV_h$ ,  $FOV_v$  as well as image dimensions. This data is necessary for calculating the distance between focal point and camera. It is stored in a configuration file. The configuration file contains data about available cameras and lenses. During start-

up, this configuration file is opened by the plug-in and the data is imported. The specified cameras and lenses are then available to the user via the user interface. Listing 4.3 shows the structure and an example of the configuration file.

```

1 #startCamera
2 #camera name, HH, INF, FAC, dimsX, dimsY
3 #lens name, min. Fokus, IFOV(mrad), FOV_H, FOV_V,
4 #endCamera
5 startCamera,
6 VarioCam hr research, 1.46, 2000, 123570,
7 Lens, Normalobjektiv, 0.5, 0.83, 29.9, 22.6,
8 endCamera,
```

Listing 4.3: Structure and example of the configuration file

The first four lines show the general structure of the configuration file. An infrared camera comes with different lenses. Each available camera is enclosed by *startCamera* and *endCamera*. The next line specifies the name of the camera and necessary parameters. Each lens starts with the keyword *lens* followed by parameters. Line five to eight show the entry of the configuration file for our camera. The configuration file allows the user to add additional cameras and lenses without changing source code.

#### 4.2.5.4 Heightmap

As mentioned before, brain shift can cause inaccuracies during image registration because the acquired 3D MR image does not correspond with the preoperative 3D image. In order to support development of algorithms which compensate brain shift, the presented work offers the possibility to extract a heightmap from a 3D image. A heightmap is a 2D array with values representing an elevation profile of a subject. The heightmap can be calculated for arbitrary directions and especially for the direction of the infrared camera. This results in an oriented heightmap which corresponds to the infrared image. To extract such a heightmap, two steps are necessary: *Alignment* and *Projection*.

**Alignment** This step is encapsulated in the module *AlignInputToOutput*. It has two input ports and has to be connected to the 2D image and the 3D model. With the orientation of the 2D image, the 3D image is transformed. It is rotated and re-sampled within its bounding box so that it corresponds to the surface normal of the 2D image.

**Projection** This module is able to extract heightmaps from the 3D model. The 3D MR image is represented by a 3D grid. The algorithm iterates over the elements of the 3D grid and extracts the heightmap. Algorithm 3 outlines the procedure.

---

**Algorithm 3:** Heightmap extraction

---

**Input :** Reference plane  $e$  of 3D data grid, threshold  $t$ **Output:** Heightmap  $h$ 

```

for each pixel  $p[x][y]$  of  $e$  do           1
     $z = 0$  ;                                2
    while  $p[z] < t$  do                  3
         $z++$ ;                            4
     $h[x][y] = z$ ;                      5

```

---

The user has the possibility to select an exterior surface of the bounding box. This plane is used by the algorithm to extract the heightmap. For each pixel of this reference plane, the algorithm iterates along the direction of the surface normal vector. This vector is perpendicular to the selected plane. It extracts the first pixel which has a value greater than a threshold and assigns its depth to the height map. Then it proceeds with the next pixel of the reference plane. The result is a 2D integer array. The values represent the depth of the first pixels in the 3D image along the direction of surface planes normal vector. To use the projection method, the following steps are necessary:

1. Load data objects (2D and 3D image)
2. Create module *AlignInputToOutput*
3. Connect data objects to module
4. Calculate new transformed 3D model
5. Create module *Project3Dto2D*
6. Calculate desired projections
7. Write desired projections to file

As step seven indicates, it is possible to write the heightmap to disk. The output format can either be plain text or binary. It contains the values as well as information about the 3D image.

This feature enables medical personnel and researches to analyse the surface structure of a 3D image intraoperatively as well as pre- and postoperatively. The examination of brain shift as well as the evaluation of algorithms which try to compensate for brain shift is possible. The implementation of both modules is based on the *Insight Segmentation and Registration Toolkit (ITK)*<sup>5</sup>. They can also be used in stand-alone mode and do not depend on each other.

---

<sup>5</sup><http://www.itk.org/>, last accessed: 2014-11-06

### 4.2.6 User Interface

The complete functionality of the image fusion algorithm is encapsulated into one single module as mentioned in section 4.2.1. This module has certain properties. If the module is selected in the pool, the properties will be accessible via the properties pane of Amira (see section 2.11). All available properties are organized in tabs: *ImageFusion*, *Calibration*, *Thermography*, *Neuronavigation* and *Evaluation*. Some additional settings are organized in tab *Options*. This section outlines all settings briefly.

**ImageFusion** The tab *ImageFusion* (figure 4.27) allows the user to specify the most important options and view the current state of the image fusion. It offers the possibility to adjust the transparency of the 2D image, the refresh rate and the minimum and maximum values for the conversion from temperature values to *COLOUR*. Both threads are started with a click on the button *Start All!*. The lines *Thermography* and *Neuronavigation* indicate the state. The state is 0 when a thread is not running and 1 when a thread has been started. An additional button starts (and stops) the transmission of tracking data from the neuronavigation system. Some of these settings are also visible in other tabs because they are important.

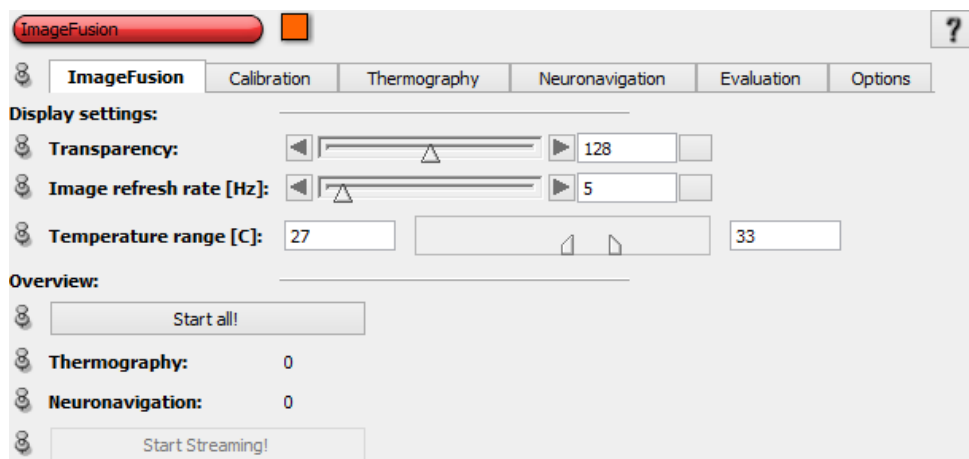


Figure 4.27: Tab *ImageFusion* with control elements

**Calibration** The tab *Calibration*, shown in figure 4.28, provides parameters for the matrix  $M_c$  mentioned in section 4.2.2. If image fusion is not running and the button *Transform!* is clicked, the 2D image will be transformed one time using the specified values. The button *reset all* assigns default values to all parameters. If image fusion is running,  $M_c$  will be calculated with the specified parameters.

**Thermography** The tab *Thermography* (figure 4.29) combines all settings regarding the connection to the infrared camera. In detail, the IP address as well as port of the server, the type of the applied

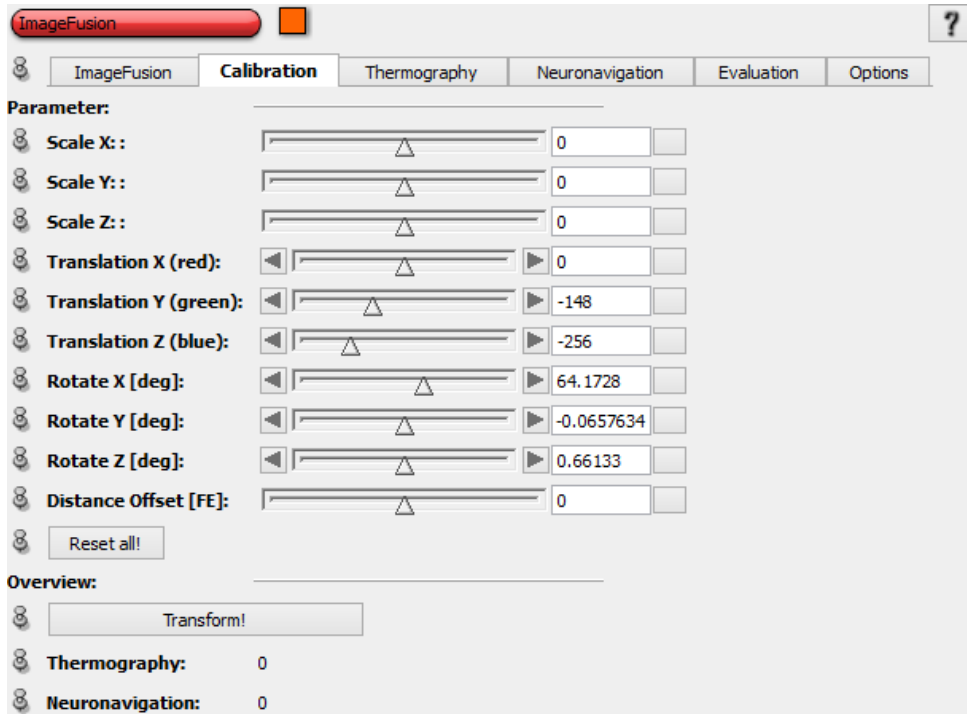
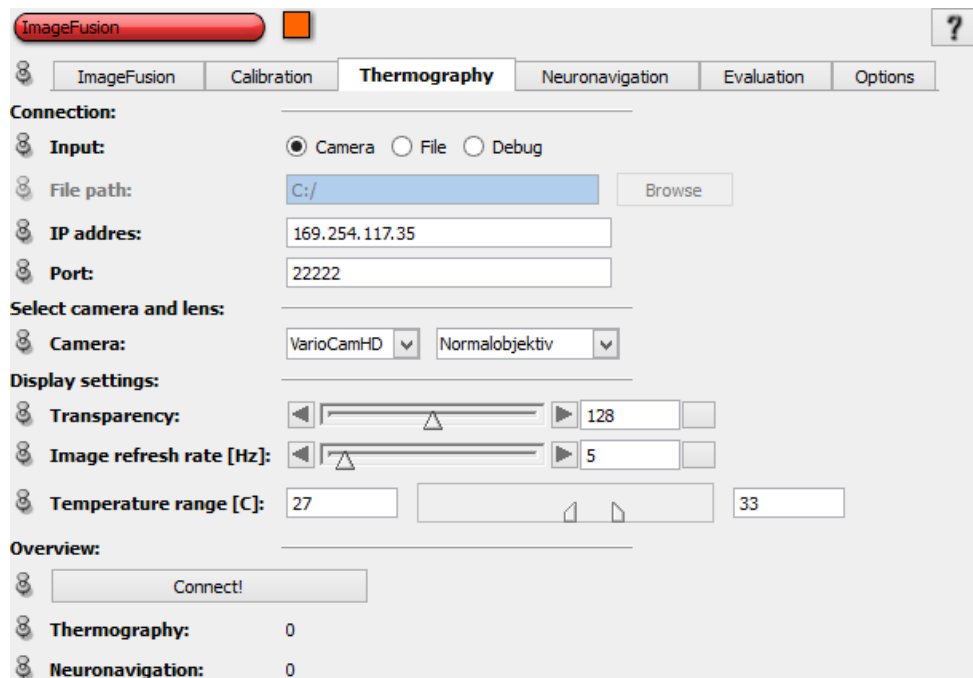
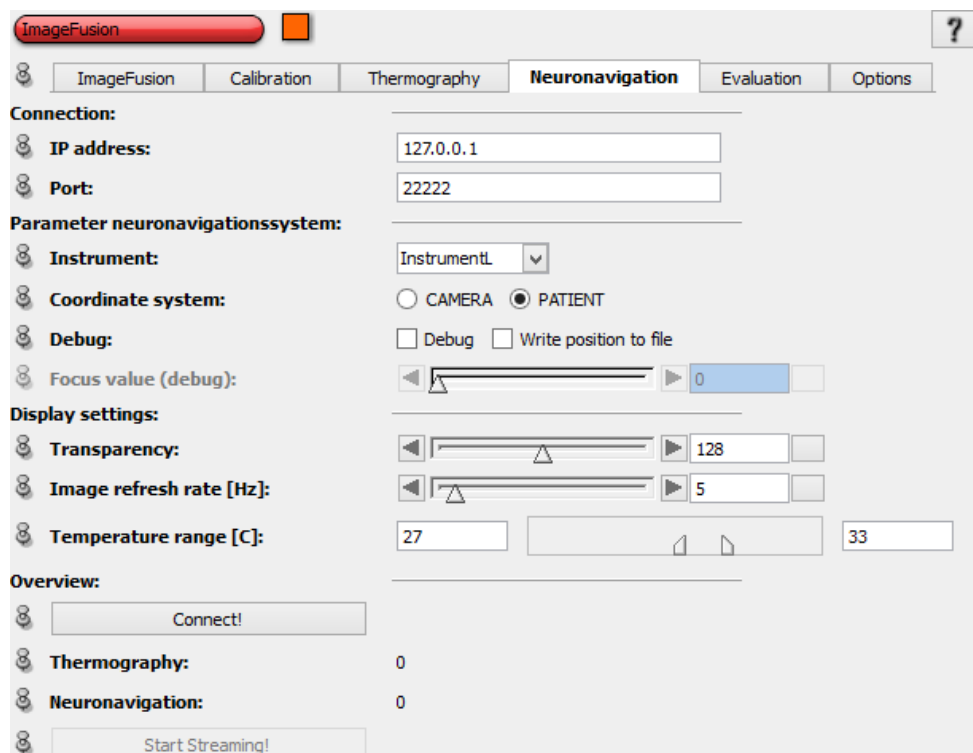


Figure 4.28: Tab *Calibration* with control elements

camera and lens as well as default settings from tab *ImageFusion*. It is possible to connect to a camera, load a custom image or run image update in debug mode. Using the debug mode, the image is updated with random values.

**Neuronavigation** The tab responsible for the settings concerning neuronavigation and image registration properties (see figure 4.30) offers the possibility to specify the IP address and port of *BrainLab VectorVision cranial 2.1.1* server. It is also possible to specify the instrument which is attached to the infrared camera. The tracking data can be in the coordinate system of the patient (or subject) but also in the coordinate system of the camera. Please note that both coordinate systems have different origins. If the debug flag is enabled, it will be possible to simulate a focus value. Furthermore, it is possible to write the final transformation  $T$  to file for further analysis. As in the previous tab, default settings for image fusion are visible. An additional button called *Start Streaming* starts (and stops) the transmission of tracking data.

**Evaluation** The *Evaluation* tab (figure 4.31) offers information and control possibilities regarding the pointer's tip. In the Amira viewer, the tip is visualized as a sphere. The radius of this sphere can be changed. Furthermore, the position of the sphere can be locked. The coordinates of the sphere in the coordinate system of the 3D image are constantly written on screen. The button *Write Pointer Position* writes the current coordinates of the sphere to file.

Figure 4.29: Tab *Thermography* with control elementsFigure 4.30: Tab *Neuronavigation* with control elements

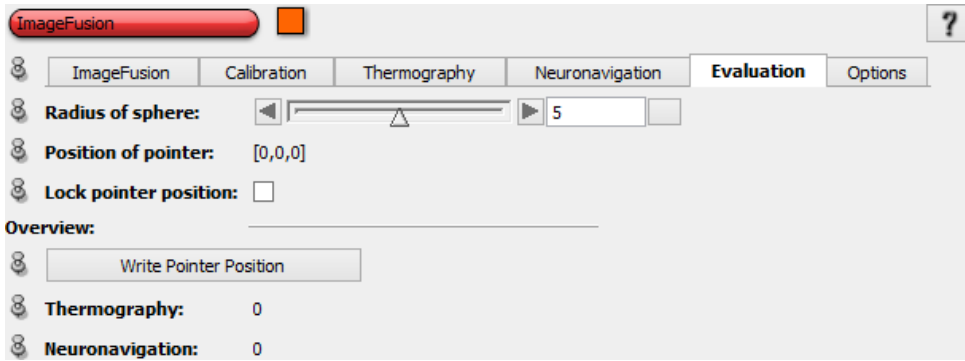


Figure 4.31: Tab *Evaluation* with control elements

**Options** This tab contains additional options (figure 4.32). The checkbox *File output* enables or disables the record mechanism described in section 4.2.5. *Orient camera* sets the camera orientation to the viewing direction of the infrared camera. If *Freeze camera orientation* is checked, the orientation of the camera will be always equal to the orientation of the infrared camera.

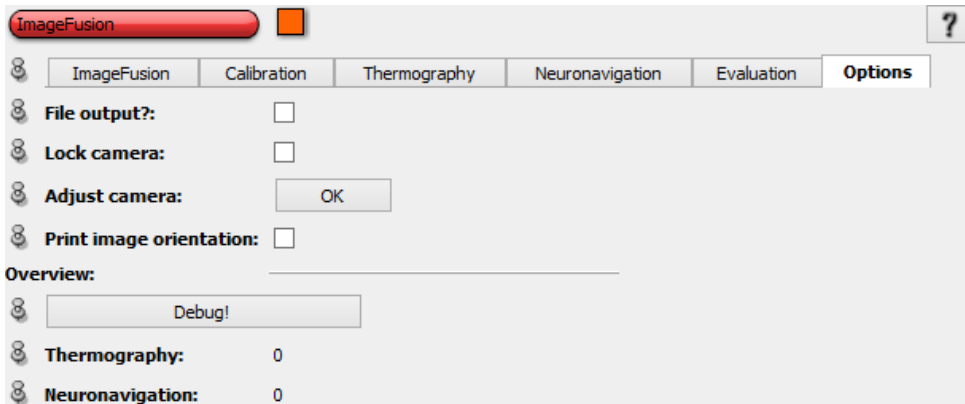


Figure 4.32: Tab *Options* with control elements

This user interface allows researchers as well as medical personnel to specify necessary parameters before and during image fusion. The tabs correspond with involved tasks and devices. Additional options for evaluation and for adjusting the camera have been added. Please note that after the parameters regarding calibration, thermography and neuronavigation have been specified the first time, an Amira mesh can be reused. It is enough to update the MR image, connect it to the *ImageFusion* module and click *Start All!*.

### 4.3 Scenario for Intraoperative Application of the System

This section gives a description of all task which are necessary to use the software. Starting with the preparation of image fusion, the set-up of hard- and software is described briefly. Then, all intraoperative

tasks are mentioned and explained. Finally, possible post-operative tasks are outlined. The scenario is as follows: A patient arrives at the hospital and needs a surgery where intraoperative TI is necessary.

### **Before surgery: outside operating room**

1. Acquire preoperative MR image.
2. Start *Amira*
3. Import MR image into *Amira*
4. Load the prepared *Amira* mesh *ImageFusion.hx* or
  - a) Create *ImageFusion* module
  - b) Create *Isosurface* from MR image
  - c) Create *SurfaceView* from *Isosurface*
  - d) Set *SurfaceView* to transparent
  - e) Adjust region of interest of the *SurfaceView*
  - f) Import an infrared image into Amira
  - g) Connect infrared image to *ImageFusion* module
  - h) Connect infrared image as texture to *SurfaceView*
5. Connect MR image to the *ImageFusion* module.
6. Check the connection settings of the tab *Thermography*
  - Check IP
  - Check Port (default: 22221)
  - Select instrument which is attached to the infrared camera (default: *InstrumentL*)
  - Select *Patient* coordinate system
7. Check the connection settings of the tab *Neuronavigation*
  - Check IP
  - Set port to 22222 (default value for *BrainLab VectorVision*)
  - Select appropriate camera and lens
8. Check file output in tab *Options*
9. Save network
10. Connect to *BrainLab iPlanNet 3.0 cranial*

11. Import the MR image into *BrainLab iPlanNet 3.0 cranial*
12. Define the positions of the fiducial markers in *BrainLab iPlanNet 3.0 cranial*

### **Before surgery: inside operating room**

1. Set up infrared camera: connect to power and to computer running the *InfraTecServer*
2. Start *InfraTecServer*
3. Set transmission frequency in *InfraTecServer*
4. Start computer running *Amira* (if not already running)
5. Start *Amira* with pre-set environment
6. Start *BrainLab VectorVision cranial 2.1.1* and register patient
7. Attach IA on CalDev
8. Attach CalDev to *ICM4*
9. Hold *ICM4* so that the fiducial markers are recognized by the neuronavigation system
10. On the screen of the neuronavigation system: select *Holes*
11. On the screen of the neuronavigation system: select 10mm hole
12. Wait for the calibration to finish
13. Remove *ICM4* from camera field
14. Detach IA and attach it on the camera

Point 6 of this part is the first which involves the patient: The registration of the patient to the neuronavigation system. Steps 7 to 13 can be executed by the surgeon but also by other medical personnel in the operating room.

### **During surgery: start image fusion**

1. Click *Send* in *InfraTecServer*
2. Click *Start All!* in *Amira ImageFusion*
3. Confirm connection in *BrainLab VectorVision*
4. Click *Start Streaming!* in *Amira ImageFusion*
5. Oversee image fusion and analyse data
  - Adjust minimum and maximum values in *Amira ImageFusion*

- Stop and start streaming
- Adjust refresh rate
- Adjust BrainLab VectorVision's transmission rate
- Adjust the camera's position and viewing direction
- Control positions with pointer

These steps outline the actual image fusion and analysis or recording of data respectively. If it is only desired to record data, it will not be necessary to adjust the minimum and maximum values because the original data will be written to file.

### **During surgery: end image fusion**

1. Click *Stop All!*
2. Save *Amira* mesh
3. Close *InfraTecServer*
4. If necessary, disassemble infrared camera and computers.

### **After surgery: outside operating room**

1. Check data files in the output folder of *Amira*
2. Start the *Replay-Server* with desired transmission frequency and input file
3. Open the *Amira* mesh
4. Set IPs in tab *Thermography* and *Thermography* to 127.0.0.1
5. Set *Thermography* port to 22221
6. Set *Neuronavigation* port to 22222
7. Click *Start All!* in *Amira ImageFusion*

If the Amira mesh has been set up previously and the set-up has not changed regarding IP addresses and ports, it will only be necessary to update the MR image. Everything else will be preset. Despite the mentioned 42 steps, most of the work can be done before and after surgery. Therefore, the application should introduce only minor disturbances to medical personnel during surgery. If image fusion is only used for later data analysis, it is not necessary to oversee image fusion but only to start and confirm the transmission of data.

This chapter ends with this description of a typical scenario. It presented the imaging phantom which has visible features in MRI, TI and white-light imaging. These are fiducial markers, a balloon filled with water and a tube filled with water. It is able to simulate brain shift, perfusion and the influence of a trepanation. The form of the trepanation can be changed. Furthermore, this chapter described a calibration-based image registration algorithm with necessary mathematical equations. An algorithm for determining calibration parameters based on the neuronavigation system was described. The algorithms which update the IR image were described in detail, including double buffering and conversion of incoming temperature data to colour values. After these sections, different possibilities for image fusion were assessed. Here, possibilities offered by *Amira* were compared regarding mesh complexity and performance. An *Isosurface* in combination with a *SurfaceView* and a texture is the best solution. Following, additional features of the plug-in were described. These are the record and replay function, the tracking of a pointer, the custom camera configuration and the extraction of an arbitrary heightmap. Second to last, the user interface of the developed plug-in was presented in detail. Finally, a typical scenario was described. The following chapter evaluates image fusion.

## 5 Evaluation

The following evaluation considers not only the algorithms but also analyses other important components of the system. Namely, the 3D model, the registration of the subject to BrainLab, the calibration procedure and the developed algorithms.

To guarantee repeatable measurements, the evaluation is inspired by Jannin et al. [JGM06] who propose a general protocol for validation of medical image processing applications: The image fusion plug-in is used by medical personnel during neurosurgery as well as researchers for data analysis of data acquired intraoperatively. The evaluation assesses accuracy of image fusion. It fuses IR images with an MR image. Objective of the application is to combine spatial information of the MR image with temperature information provided by a stream of IR images. Validation data set consists of acquired MR and IR images of the imaging phantom. A *Magnetom Verio*<sup>1</sup> scanner delivered the 3D images of the imaging phantom. IR images are acquired using the *VarioCAM HD head 680 S / 30mm \*\*\*MEDICAL \*\*\** described in section 2.3.2. Computation of the fused image is performed according to the presented methods. The reference data set is a fused MR-IR image where the distances between visible pairs of features is zero. Features are the coordinates of the fiducial markers' centre points and the tube's borders of the imaging phantom in Amira. All measurements of the geometric distance are performed looking at the imaging phantom perpendicularly from the top. The term *angular error* represents the error with respect to orientation whereas *tip* or the *axial error* represents the error with respect to position. All mean values are calculated using arithmetic mean. Expected results are:

- Model: The MR image and the extracted isosurface introduce slight inaccuracies
- Registration to BrainLab: The definition of the marker's positions and the registration of the subject to the neuronavigation system will introduce only a slight error.
- Instrument adapter: Calibration and attachment of the IA will introduce major error.
- Distance: The setting of the focus value can only introduce an error if not performed correctly
- Angle: The error will correlate with the camera's angle of incidence

---

<sup>1</sup><http://usa.healthcare.siemens.com/magnetic-resonance-imaging/3t-mri-scanner/magnetom-verio>, last accessed: 2014-11-10

**Model** MRI is a precise but still inaccurate imaging technique. The data of the imaging phantom has a resolution of  $160 \times 512 \times 512$  voxel where the size of one voxel is  $1 \text{ mm} \times 0.48828 \text{ mm} \times 0.48828 \text{ mm}$ . This leads to a possible maximum error as shown in table 5.1.

Table 5.1: Maximum error of the MR model

|               | X (mm) | Y (mm)  | Z (mm)  |
|---------------|--------|---------|---------|
| Maximum error | 2      | 0,97656 | 0,97656 |

The maximum error is twice the voxel size because of the quantization error during image acquisition. Please note that the 3D image is stored in a grid with the mentioned size and resolution. During image acquisition, spatial information gets lost. Algorithms and measurements which are based on this model can not be more accurate than the image. MR images with a higher resolution could improve image fusion because structures visible in the infrared image would overlay more precisely. Modern scanners like the INUMAC<sup>2</sup> provide a resolution up to 0.1 mm and could improve accuracy.

**Registration BrainLab** The following measurements analyse the influence of the BrainLab registration procedure where the digital data of the subject, the MR image, is registered to the real subject. For this, two steps are necessary: First, defining the positions of the fiducial markers in BrainLab VectorVision. Second, touching the fiducial markers of the imaging phantom with the pointer.

Registration error is determined by measuring the distance between the pointers tip (indicated by the sphere as mentioned in section 4.2.5.2) and the centre of the markers in the 3D model. Please note that the position of the sphere does not rely on  $M_c$  but only on data delivered by BrainLab. Hence, it depends only on the first registration and not on the calibration-based registration presented in section 4.2.2.

During evaluation, the markers were defined in the digital image of the imaging phantom using *iPlanNet 3.0*. Then, the registration was performed. For this, each marker of the imaging phantom was touched with the pointer until *VectorVision cranial 2.1.1* recognised it. Six markers were defined in *iPlanNet 3.0* and six markers were touched with the pointer. This procedure was repeated three times. Table 5.2 shows the axial error of the coordinates. The real pointer was always on the same position but the coordinates delivered by BrainLab vary.

The maximum axial error introduced by the registration to BrainLab is 0.99 mm in z direction. It is remarkable that this value is nearly two to three times the value of the error in x and y direction. This is because the z direction of the coordinate system was nearly parallel to the viewing direction of the tracking system's cameras. Tracking of depth is not as precise as tracking in the directions perpendicular

---

<sup>2</sup><http://portal.uni-freiburg.de/inumac>, last accessed: 17.11.2014

Table 5.2: Mean error and standard deviation of the registration error introduced by *VectorVision cranial 2.1.1* and *iPlanNet 3.0*

|                    | X (mm) | Y (mm) | Z (mm) |
|--------------------|--------|--------|--------|
| Mean Error         | 0.37   | 0.43   | 0.99   |
| Standard Deviation | 0.31   | 0.31   | 0.79   |

to the viewing direction. The measured maximum distance between the centre of a fiducial marker in the MR model and the delivered coordinate is 2.46 mm. To keep this error as low as possible, it is necessary that medical personnel sets the position of each fiducial marker exactly to the centre of the donut shape. Furthermore, it is important to touch exactly the centre of the fiducial markers of the imaging phantom. Doing so results in a mean error of 0.60 mm with a mean standard deviation of 0.44 mm. Images 5.1a to 5.1c show an exemplary view of the acquired images. The gray sphere indicates the pointer's tip. However, the tip of the real world pointer was always located at the centre of the real world fiducial marker. If not performed correctly, the registration will introduce a major error.

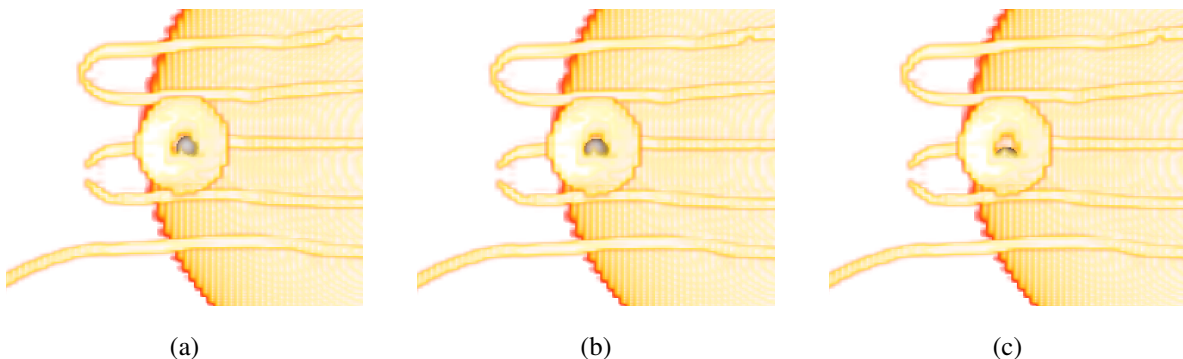


Figure 5.1: Three images showing the position of the pointer's tip for three different registrations.

**Calibration** The IA needs to be calibrated in order to work with the neuronavigation system. For this, the calibration device *ICM4* from BrainLab as well as the calibration device, called CalDev, is necessary. The IA is attached to the CalDev which is then attached to the *ICM4* (see section 4.2.2). Calibration starts as soon as the fiducial markers of the IA are visible to the neuronavigation system's cameras. *VectorVision cranial 2.1.1* provides the angular and axial error of the calibration. For the evaluation, calibration was performed ten times. Mean axial and angular error and standard deviation are shown in table 5.3.

Deviations in the tip's position do not influence registration quality significantly. However, the angular error translates to a major error in the image fusion. This is because the orientation of the instrument

Table 5.3: Axial and angular error introduced by the calibration of the instrument adapter.

|                    | Angle (°) | Tip (mm) |
|--------------------|-----------|----------|
| Mean               | 0,2       | 0,1      |
| Standard Deviation | 0,1       | 0,1      |

adapter influences the determination of the calibration parameters and with it image registration. The mean error is  $0.2^\circ$ . The maximum error is  $0.3^\circ$ . Attaching the IA on the camera leads to another error. As mentioned before, it is essential that the IA is attached to the camera so that it has always the same position. To do this, the IA is attached to an existing body part (see figure 5.2a). This part was especially designed for this purpose by another research group. Figure 5.2b shows the body part with attached IA.



Figure 5.2: Special-purpose body part without (5.2a) and with (5.2b) instrument adapter attached

During testing and evaluation of the image fusion algorithms, it became clear that the body part still introduces slight inaccuracies, both angular and axial. In order to assess these inaccuracies, the IA was attached ten times to the body part. The camera was not moved during those measurements. The results are shown in table 5.4.

Table 5.4: Standard deviation of the orientation and position of the IA when attaching the instrument adapter.

|                    | Angle (°) | Tip (mm) |
|--------------------|-----------|----------|
| Mean               | 96        | 479.4    |
| Standard Deviation | 0.5       | 0.4      |

For a defined position of the camera, the standard deviation of the orientation of the instrument adapter's axis is  $0.5^\circ$ . This leads to an inaccurate image fusion. The small value translates to an axial offset depending on the distance between the IA and the subject. The maximum deviation is  $0.7^\circ$ . Attachment

led to a maximum error of 0.9 mm. The errors caused by calibrating and attaching the IA result in a major error in image fusion because image registration relies on a precise orientation and position of the IA. To measure this error, the IA was placed in two extreme positions:  $-\phi$  and  $+\phi$ .  $-\phi$  refers to the position where the IA is tilted to the left.  $+\phi$  refers to the position where it is tilted to the right. Please note that the IA was attached with great care and within parameters but not purposely wrong. However, the mechanism which fixates the IA on the body part has a slight tolerance and can be moved or tilted respectively. Results are shown in table 5.5.

Table 5.5: Error in the final image resulting from attaching the instrument adapter.

|                    | $-\phi$ (mm) | $+\phi$ (mm) |
|--------------------|--------------|--------------|
| Mean               | 7.94         | 10.06        |
| Standard Deviation | 0.52         | 0.68         |

The average of the mean errors is 9 mm. The measured maximum error is 11.32 mm. This displacement shows that attaching the instrument adapter is a crucial step during image fusion and can falsify results greatly.

Calibration of the instrument adapter with the *ICM4* and the calibration device is an important cause of failure. Tools which are more precise could help to minimize or eliminate this error. Another issue concerning the instrument adapter is the attachment of the device to the infrared camera or microscope stand, respectively. The body part which has been designed to guarantee a precise position does not fulfil its task appropriately.

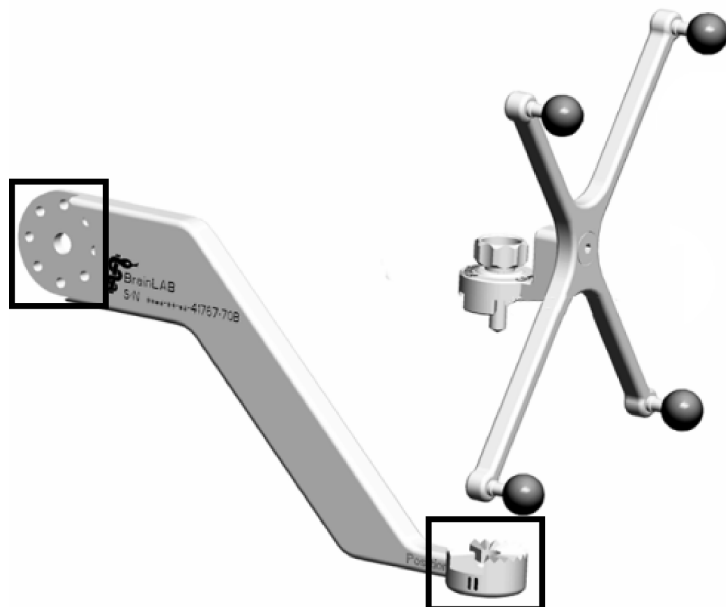


Figure 5.3: Alternative to the current IA and body part.

An improved and more suitable body part and IA could help to overcome this issue. A possible solution is the *BrainLab microscope adapter* set shown in figure 5.3. It consists of a body part (left) and an IA (right). The body part's position is defined by holes on the left side. The position of the IA is defined by the toothed end of the body part (lower right). This device ensures a precise positioning of the IA. An alternative calibration device based on these features could decrease the error introduced by instrument calibration.

Previous measurements assessed the error introduced by the magnetic resonance scanner, the neuronavigation system and the calibration procedure. The following measurements were performed using a single registration and calibration with the same MR image of the imaging phantom. All measurements have the objective to assess the overall error during image fusion in Amira as well as quality of the calibration parameters determined in section 4.2.2.

**Distance Function** The distance of the infrared camera to the neuronavigation system influences image fusion because scaling depends on it. The focus value, which represents the distance, is set by the medical personnel manually. However, the focus value for one position of the camera can vary. The following measurement assesses the influence of a varying focus value. The infrared camera was positioned approximately 30 cm away from the subject, clamped and defocused. Please note that a distance of approximately 30 cm is the typical distance during an intraoperative scenario where an additional white-light camera focusses the subject. After setting the distance, the focus value was adjusted. This was done 10 times. The results lead to an average focus value of 6573 with a standard deviation of  $\pm 112$ . This translates to distances between 27,84 cm and 29,16 cm. As mentioned in section 4.2.2, the focus value is used for calculating the scaling factor. For this measurement, the image size varies from a minimum of 14.36 mm  $\times$  10.91 mm to a maximum of 15.05 mm  $\times$  11.43 mm. This leads to a horizontal error of 0.69 mm and to a vertical error of 0.52 mm. Overall, the error introduced by the focus value is small but measurable. A working autofocus could overcome this error.

**Angle of Incidence** For this set of measurements, the angle of the camera was changed from  $0^\circ$  to  $30^\circ$  and  $60^\circ$ . In other words, the normal vector of the camera's sensor array points vertically downwards ( $0^\circ$ ) and is then tilted to  $30^\circ$  and  $60^\circ$ . For each angle, measurements at three distances were performed. To measure mean error and standard deviation, the positions of the spheres' centre in the MR image were determined one time. These positions are used as a reference for the following measurements. Using the *SurfaceView*, which is enriched with infrared data, the centres of the four top markers were determined. The distance between corresponding centres was measured and the mean of all distances was calculated. It should be zero ideally. The actual value is a measure for accuracy of image fusion. It is expected that

the error increases with an increasing angle.

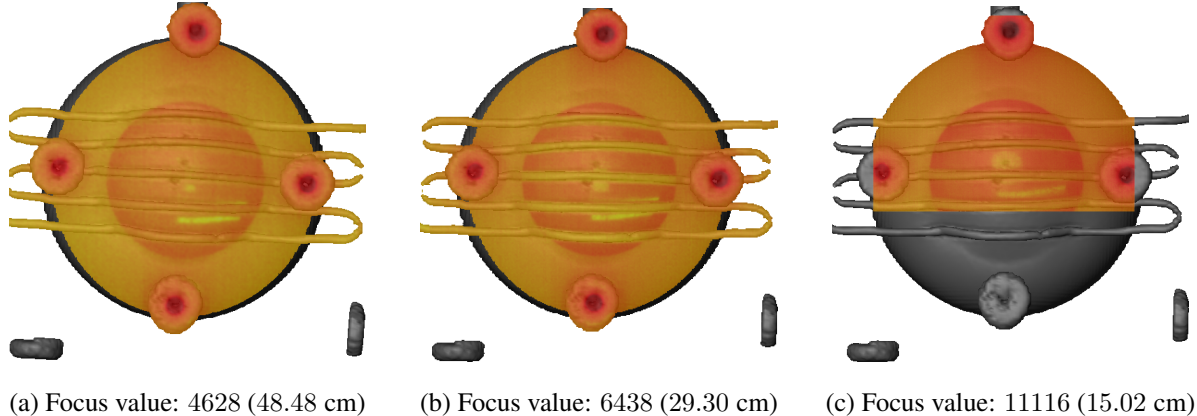


Figure 5.4: Image fusion result using a camera angle of  $0^\circ$

Images acquired during the first set of measurements are shown in figure 5.4. During these measurements, the camera pointed vertically downwards. The orientation of the shown images is perpendicular to the direction of the camera or imaging sensor, respectively. The dark red or black dots represent the markers in the image acquired by thermographic imaging. They overlay with the markers visible in the MR model. The tube, indicated by yellow lines in the infrared image, overlay with the tube in the MR image. Please note that the yellow line and dot in the middle of the IR image is a caused by reflection.

Table 5.6: Mean error and standard deviation for a camera angle of  $0^\circ$

| Distance (cm)           | 48.48 | 29.30 | 15.02 |
|-------------------------|-------|-------|-------|
| Mean error (mm)         | 0.62  | 0.52  | 0.64  |
| Standard deviation (mm) | 0.16  | 0.26  | 0.08  |

Table 5.6 shows the results of the measurements. The measured mean error is for all distances below 1 mm. Considering the standard deviation, the error is still below 1 mm. Given the previous measured errors, the quality of image fusion is good. The high accuracy also results from the fact, that the calibration parameter mentioned in section 4.2.2 were determined with a camera angle of  $0^\circ$ .

Figure 5.5 shows the images acquired during the  $30^\circ$  measurements. The dark red or black dots, indicating the fiducial markers, do not overlay perfectly with the MR model. There are obvious inaccuracies. Besides that, the displacement is not the same for every dot. This is the result of inaccurate calibration parameters, the error introduced by calibration and attachment of the IA as well as perspective distortion. In other words, the infrared image is slightly tilted regarding the position of the imaging sensor. Comparing these images with the images acquired during the  $0^\circ$  measurements shows significant differences in accuracy.

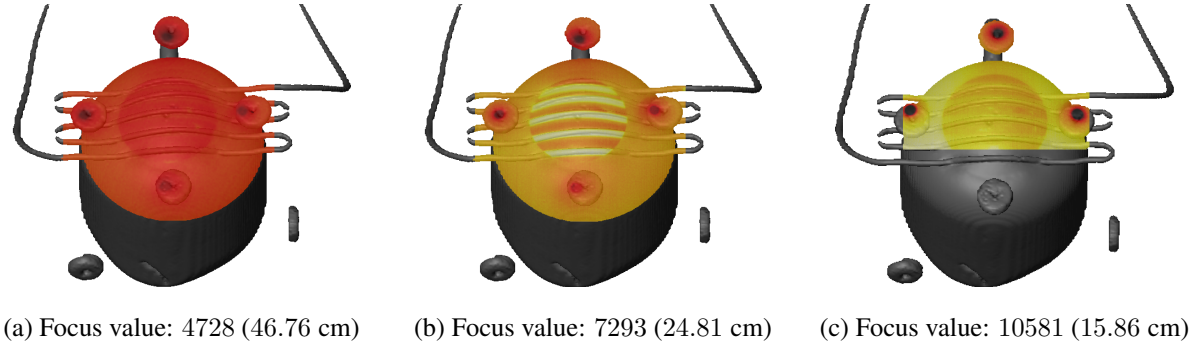


Figure 5.5: Image fusion result using a camera angle of  $30^\circ$

The results of the  $30^\circ$  measurements are listed in table 5.7. Please note that the measurements were performed in the coronal view where the viewing direction of the virtual camera is  $0^\circ$ . The measured mean errors in each direction as well as the average error increase significantly. The maximum error observed during measurement was 3.7 mm for the displacement of one single marker. The average error of 0.59 mm increases to 2.89 mm. This is because the calibration parameters were measured manually which introduces a slight inaccuracy. Furthermore, the mentioned errors during registration, calibration and attachment contribute to inaccuracy. In addition to that, the chosen projection method (texture mapping) introduces an error because it uses an orthogonal rather than a perspective projection.

Table 5.7: Mean error and standard deviation for a camera angle of  $30^\circ$

| Distance (cm)           | 46.76 | 24.81 | 15.86 |
|-------------------------|-------|-------|-------|
| Mean error (mm)         | 2.71  | 2.84  | 2.09  |
| Standard Deviation (mm) | 0.08  | 1.36  | 1.27  |

The figures 5.6a to 5.6c show images acquired during the  $60^\circ$  measurements. The black dots are farther away from the centre of the fiducial markers in the MR image. Furthermore, the yellow lines in the infrared image, which indicate the tube of the imaging phantom, show the axial distortion introduced by calibration, attachment and registration. However, the perceived error does not much differ from the error in the  $30^\circ$  measurements.

Table 5.8 shows the results of the  $60^\circ$  measurement. The maximum error observed during measurement was 4.8 mm for a single displacement of one marker. The mean error increases to 3.89 mm. This is caused by calibration and attachment of the IA, inaccurate calibration parameters but also because of texture mapping which uses an orthogonal projection instead of a perspective.

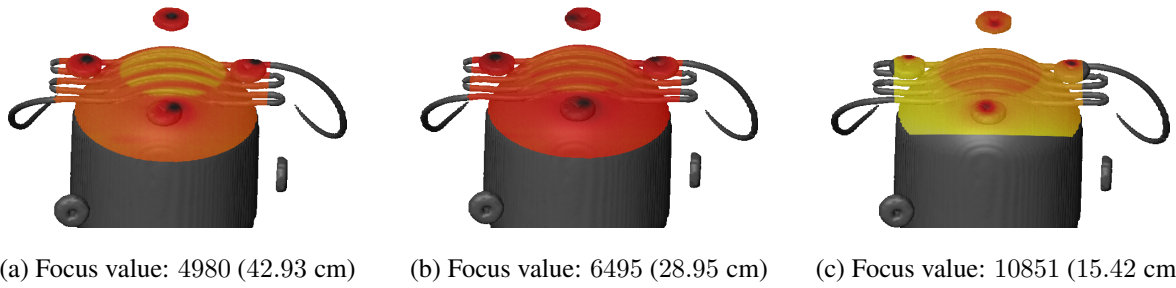


Figure 5.6: Image fusion result using a camera angle of  $60^\circ$

Table 5.8: Mean error and standard deviation for a camera angle of  $60^\circ$

| Distance (cm)           | 42.93 | 28.95 | 15.42 |
|-------------------------|-------|-------|-------|
| Mean (mm)               | 3.58  | 3.80  | 4.30  |
| Standard Deviation (mm) | 0.90  | 0.50  | 1.54  |

**Summary** The measurements show that an image fusion with a mean error 2.46 mm is possible with the presented algorithms and hardware. The errors introduced by the MR model can be influenced hardly by the user. However, a high-resolution MR image from a scanner like the mentioned INUMAC could improve image fusion. The error introduced by the registration of the subject to the neuronavigation system can be decreased by performing the registration with great care. The evaluation showed, that calibrating and attaching the IA is a major cause of failure which has to be solved before intraoperative application. Table 5.9 summarizes the results of the  $0^\circ$ ,  $30^\circ$  and  $60^\circ$  measurements.

Table 5.9: Average errors for the  $0^\circ$ ,  $30^\circ$  and  $60^\circ$  measurements with the overall average error.

| Angle of incidence | $0^\circ$ | $30^\circ$ | $60^\circ$ | AVG  |
|--------------------|-----------|------------|------------|------|
| Mean (mm)          | 0.59      | 2.89       | 3.89       | 2,46 |

The mean error is 0.59 mm but increases with a changing angle of incidence. It is caused by inaccurate calibration parameters as well as orthogonal projection. Inaccurate calibration parameters are the result of the calibration procedure described in section 4.2.2. This procedure depends on two factors: First, the user performing the calibration. If the user does not work precise and with great care, the calibration parameters will not be as accurate as they should be. Second, the quality of the tracking data. Errors during the registration of the MR image to the neuronavigation system, touching the fiducial markers with the pointer at wrong positions or faulty predefined marker positions inflict the quality of the tracking data. This leads to wrong calibration parameters. In other words, if the infrared camera points not vertically downwards during determination of the calibration parameter, the parameters will be faulty and will lead to an inaccurate image fusion. To achieve this, calibration and attachment of the IA have to be precise.

Otherwise, calibration parameters can hardly be re-used.

All measurements except one (see table 5.5) indicate that there is no direct correlation between object distance and error. However, this error was expected during preparation of the measurements. It is not present because the measurements were performed using a single calibration and attachment of the IA. The influence of the distance corresponds to the inaccuracy introduced by calibration and attachment of the instrument adapter to the portable stand or infrared camera respectively. With the current set-up, it is necessary that the calibration parameters are determined or corrected each time the instrument adapter is calibrated and attached or the IA has to be calibrated and attached with great care. If calibration parameters are reused and calibration and attachment is not accurate, the average mean error increases to 9.00 mm.

Image fusion and multimodal image registration is crucial because it is hard to determine features in both images. At the beginning of the procedure, a global optimization problem has to be solved in order to find corresponding features. The presented calibration-based approach provides image registration with a mean error of 2.46 mm. A simple extension of the presented approach which would improve accuracy of image fusion is to use the user interface for adjusting the image fusion during surgery. With the use of the pointer, which is visible in Amira and in the infrared image, the user has the possibility to adjust the position of the 2D image so that the tip and the sphere overlay. However, this would introduce additional interaction. This could disrupt intraoperative procedures and with it, surgery. Besides that, a function which compensates the error via interpolation could overcome this increasing inaccuracy. To use this approach, the calibration procedure has to be done for several orientations of the camera. With these sets of calibration parameters, it is possible to calculate new calibration parameters for a current camera position with respect to the camera angle. Besides that, ray casting or a perspective correct texture mapping approach could eliminate the error caused by the texture mapping. Yet another approach is to use alternative hardware for attaching the instrument adapter. This hardware should be more precise so that the calibration parameters (or the set of calibration parameters) does not become invalid each time the instrument adapter is demounted from the portable stand. The proposed microscope adapter set could help to overcome this issue.

## 6 Summary

Thermography is a technology which can support medical personnel during neurosurgery. Temperature information provided by an infrared camera enables the user to analyse cortical perfusion, morphological features and neuronal activity of the observed area. This is especially important for the analysis of patients with tumours, epilepsy or strokes. However, looking only at an infrared image aggravates an effective analysis. This is because an infrared image does not possess enough spatial information. In other words, the user needs additional mental effort to relate temperature values of infrared images to the observed area. Image Fusion helps to reduce this mental effort. Here, an infrared image is fused with an image representing the observed area. The result is an enriched image with spatial and temperature information.

This thesis presented an Amira plug-in performing image fusion of a stream of two-dimensional IR images and a three-dimensional MR image of the brain. It combines temperature information of intraoperative TI with spatial information of preoperative MRI. To do this, a neuronavigation system tracks the position of an instrument adapter and provides the plug-in with position and orientation of it with respect to the observed subject. The instrument adapter is attached to the infrared camera. However, spatial data provided by the neuronavigation system is not exactly the position and orientation of the infrared camera. With the help of the presented calibration-based image registration algorithm, the position and orientation is transformed in a way that it corresponds with the position and orientation of the infrared camera's sensor array. To do this, a method on how to perform calibration and how find calibration parameters was presented. Furthermore, a calibration device was developed and produced. This calibration device makes it possible to calibrate the instrument adapter so that it is recognized by the neuronavigation system. With the calibration parameters and the calibration device, image registration is performed.

Besides image registration, the plug-in performs the update of image data. For this, it receives a data stream from the infrared camera. This provides the user with a near real-time image. The user has the possibility to adjust the colourmap to achieve the best visualisation. Double buffering prevents Amira from displaying scattered and distorted images.

The connections to the infrared camera as well as the neuronavigation system are realized using the open source framework OpenIGTLink. The plug-in provides the possibility to run image registration

and image update in parallel or just one of the tasks. They operate independently. The user interface provides many options to control the plug-in like adjusting the refresh rate, or setting the position of the virtual camera so that it corresponds with the viewing direction of the infrared camera. Furthermore, it is possible to track an instrument belonging to the neuronavigation system: the pointer. The tip of the pointer is indicated as a sphere in the viewer of Amira. For further evaluations, an additional Amira module was developed which extracts arbitrary heightmaps. If the user wants to store the intraoperative acquired data, a record-and-replay mechanism is available.

Different possibilities of combining both images provided by Amira were assessed and compared regarding effort and performance. It was found that a combination of *Isosurface*, *SurfaceView* and texture mapping delivers the best results regarding mesh complexity and speed.

For testing and evaluation of the developed algorithms, an imaging phantom was designed. It has features visible in MRI, TI and white-light imaging. The phantom allows simulation of brain shift, trepanation and perfusion. It allows repeatable and controlled measurements. During evaluation, several measurements were performed. Results show that the proposed image fusion plug-in will deliver a fused image with a mean error of 2.46 mm if the set-up is appropriate. An appropriate set-up means that calibration and attachment of the instrument adapter have been performed with great care. Furthermore, the calibration parameters which transform the position and orientation of the instrument adapter delivered by the neuronavigation system have to be precise. The observed maximum mean error is 10.06 mm.

The presented Amira plug-in for image fusion of intraoperative TI with MRI in neurosurgery allows medical personnel an intraoperative as well as a postoperative analysis of the combined data. Though it does not achieve a perfect overlay, it provides the user with a fused image showing temperature data at a position which corresponds to the origin of the data. With this fused image, the mental effort which is necessary to analyse the infrared image is reduced.

## 7 Future Work

### 7.1 Phantom

The presented imaging phantom allows evaluating and testing of image registration and image fusion algorithms. With the simulation of brain shift, it also provides the possibility to assess non-linear image registration algorithms. A more complex set-up and different materials of the tube could allow a more sophisticated analysis of these algorithms because the deformation becomes more complex. The more complex set-up of the tube also provides means for an assessment of the effect of perfusion, flushings and the application of cold boluses in TI. Furthermore, the balloon can be replaced by a PVA-C model. This model could resemble a human brain in form, behaviour and structure even more and could allow a more realistic image fusion and deformation. Furthermore, it would enable the usage of ultrasonic imaging devices. An internal structure which simulates a tumour could further enhance analysis possibilities. Besides that, the syringes could be replaced by a motorised pump for an easier handling of perfusion and inflation or deflation of the balloon, respectively. The imaging phantom is designed to have features in MRI, white-light imaging and TI. It should also provide features visible in computed tomography but the quality and visibility still has to be verified.

### 7.2 Image Processing

The presented application provides image fusion with a mean arithmetic error of 2.46 mm. To further improve image fusion, several enhancements have been proposed throughout this thesis. In detail, a compensation function for the error of the calibration parameters, using the user interface in order to correct inaccuracies as well as replacing the current IA with a more accurate device like the *BrainLab microscope adapter*. Besides these means, a combination with an additional feature-based registration algorithm could improve image fusion. Here, the presented calibration-based approach decreases search space for a feature-based image registration algorithm. Then, the vessel-structure as well as the structure of the gyri could provide necessary features in form of lines, points or skeletons. To enhance visibility of these structures, an additional white-light camera as well as a contrast agent could be applied. Further-

more, the pointer's tip could act as a feature. The expected position of the tip is available and indicated by the sphere. The real position is visible in the IR image. A segmentation algorithm could extract the tip from the IR image and use it for a feature-based point pattern matching algorithm.

A problem which is not considered by the presented image fusion algorithm is brain shift. The surface of the brain during surgery is not completely similar to the preoperative brain image. To compensate brain shift, the 3D MR image has to be updated. The application of two white-light cameras with epipolar geometry could provide the new surface. Furthermore, dedicated stereo cameras similar to the Microsoft Kinect<sup>1</sup> could deliver the surface of the brain after the skull has been opened by the surgeon. Another alternative is the usage of light-field cameras [THMR13]. Besides that, algorithms based on visual clues could update the 3D image.

Visualisation of temperature data can be improved. Ray casting could eliminate errors introduced by orthogonal projection of the texture mapping approach. This is because ray casting is able to perform perspective projection. Furthermore, ray casting does not interpolate temperature data. Therefore, only these pixels get assigned a colour value where the IR camera has actually measured temperature. Besdiest that, perspective correct texture mapping could minimize this error. An additional improvement is the capability to change the colourmap during image fusion.

An alternative or additional visualization technique is to project the acquired infrared image onto the brain of the subject directly. This would minimize the mental effort which is necessary to relate the temperature data to its place of origin. Furthermore, a video see-through display could act as a magic lens (see Preim et al. [PC14]). A neuronavigation system could track the position of a display and update the view accordingly. The display would show a live video of the brain with the infrared image as an overlay. A head-mounted display could also provide fused information (see Cutolo et al. [CPF14]). Additional information like predefined objects or trajectories could enhance visualisation.

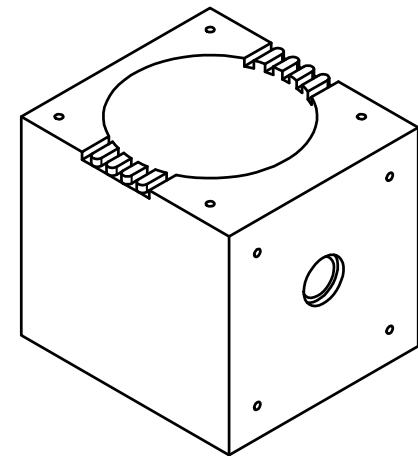
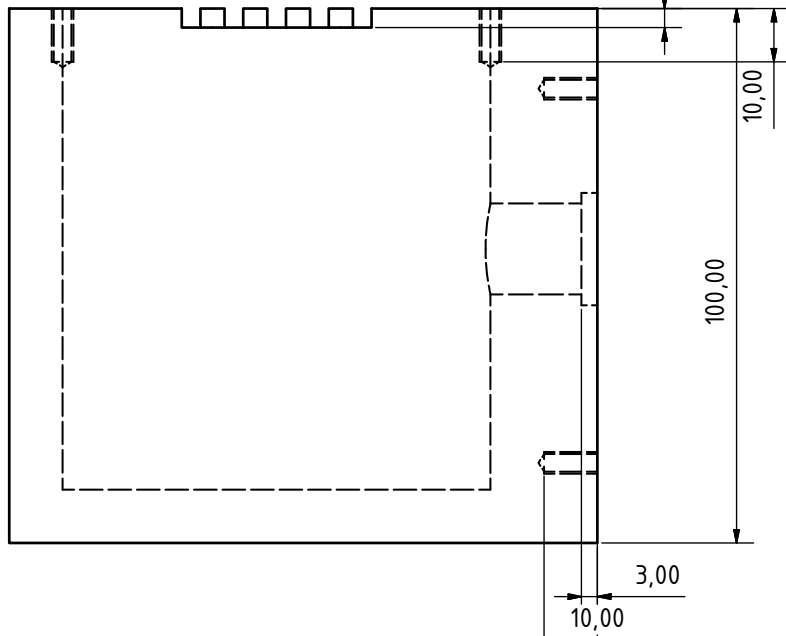
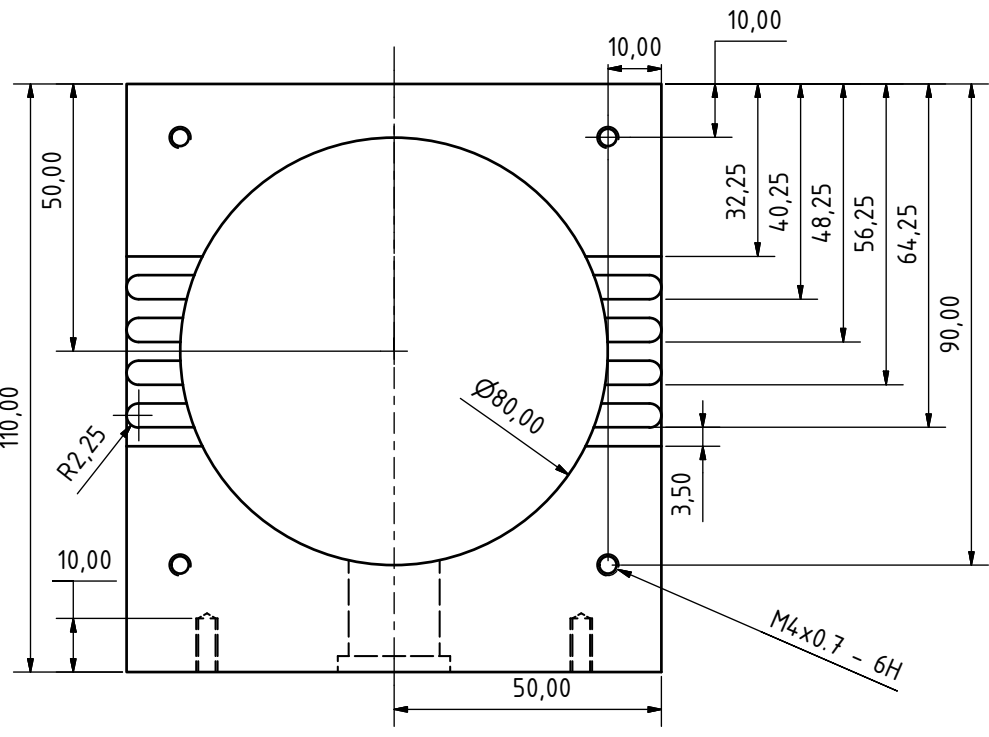
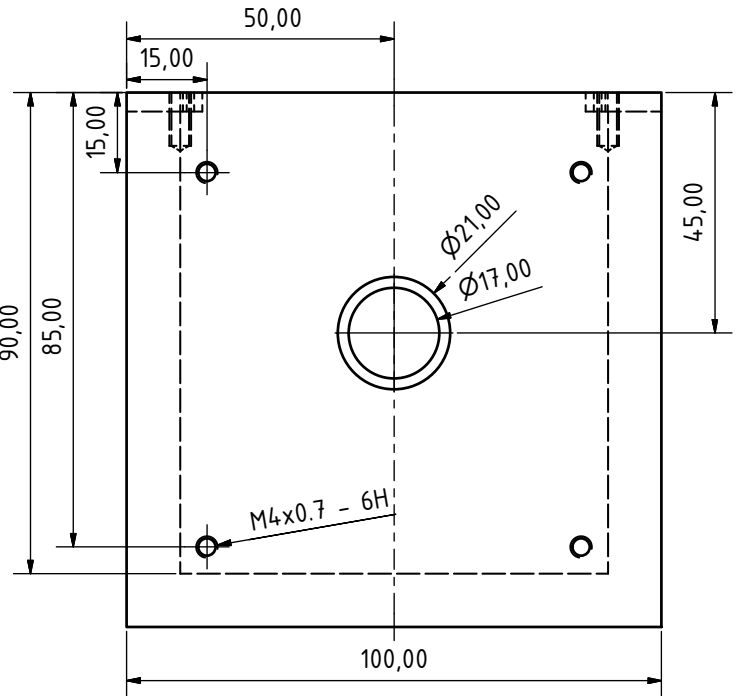
Furthermore, additional image processing algorithms could improve analysis capabilities of the image fusion application. Combination with classification, segmentation, restoration and feature extraction algorithms can improve the usage of TI and the image fusion application ([RA12]). Execution of the image update as well as the proposed ray casting algorithm could be performed on dedicated hardware like GPUs or Cellular Neural Networks (CNN, see [CY88]) which could improve performance of the application. An additional configuration file for calibration parameter would increase usability. Intraoperative efficiency and suitability has to be verified with further measurements. For this, the errors introduced by the calibration and attachment of the instrument adapter should have been minimized or eliminated, respectively.

---

<sup>1</sup><http://www.microsoft.com/en-us/kinectforwindows/>, last accessed: 2014-11-18

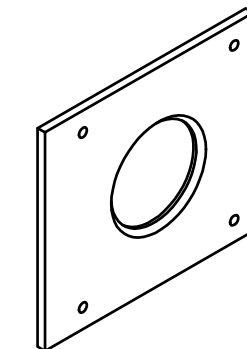
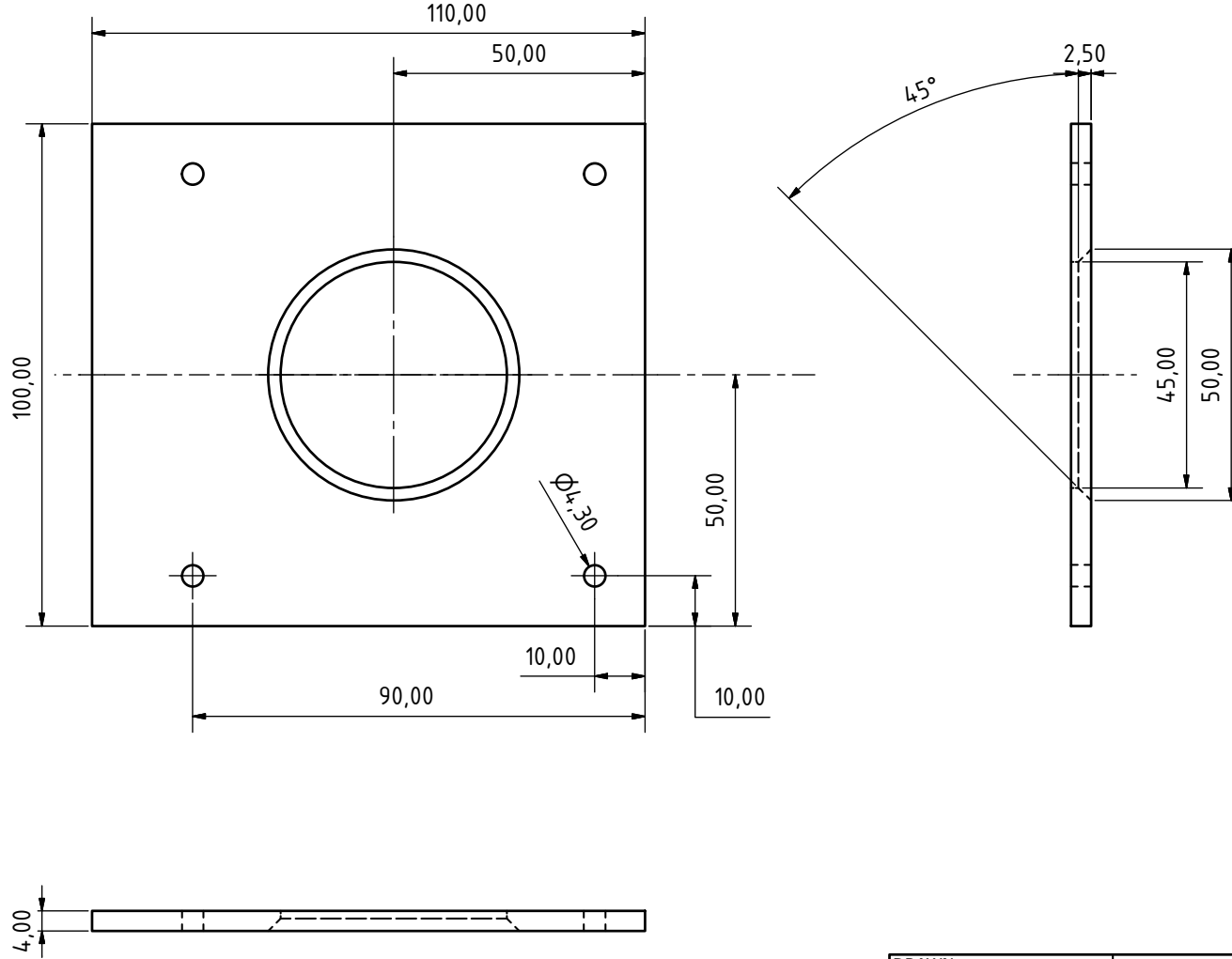
## 8 Appendix

1. Drawing of the imaging phantom's body: *Phantom - phantom\_main*
2. Drawing of the imaging phantom's lid: *Deckel für Phantom - phantom\_deckel*
3. Drawing of the imaging phantom's front: *Seitenteil für Phantom - phantom\_seite*
4. Drawing of the imaging phantom: *Phantom - phantom\_total*

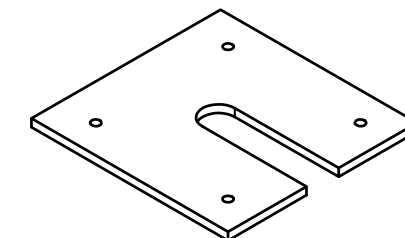
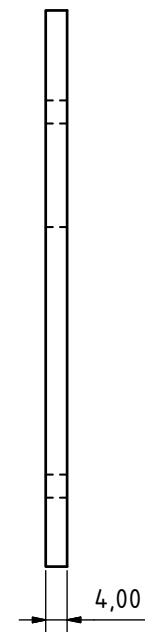
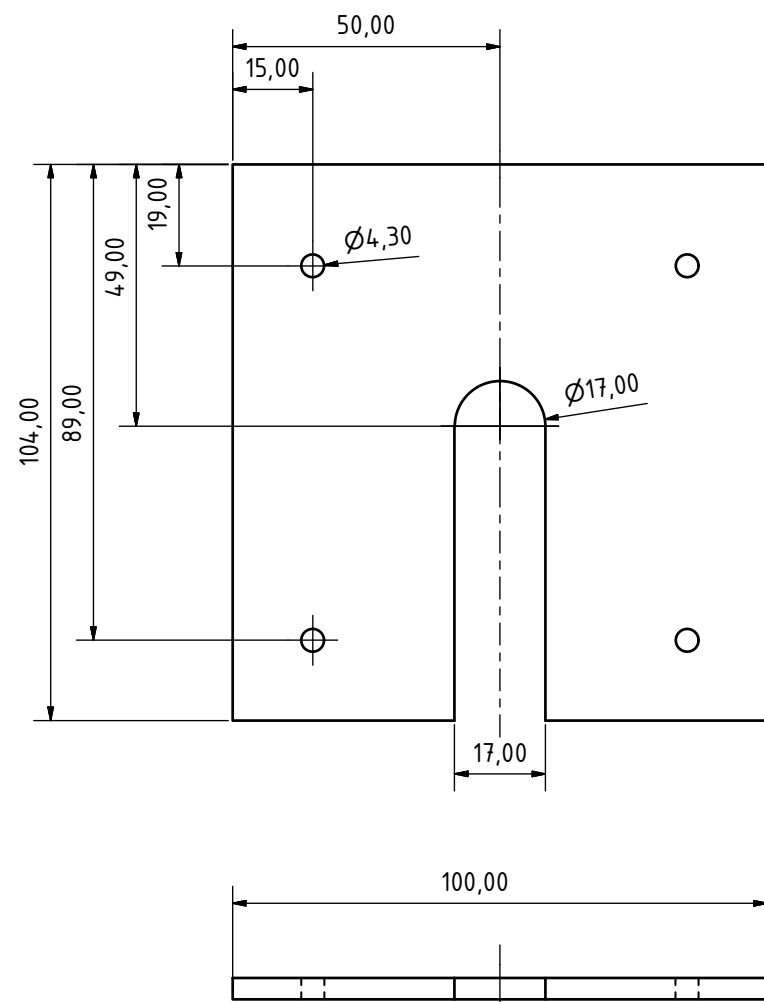


|                          |            |                                     |  |              |  |              |
|--------------------------|------------|-------------------------------------|--|--------------|--|--------------|
| DRAWN<br>Florian Weidner | 27.08.2014 | Info: Alle scharfen Kanten brechen. |  |              |  |              |
| CHECKED                  |            | TITLE<br><br>Phantom                |  |              |  |              |
| QA                       |            |                                     |  |              |  |              |
| MFG                      |            |                                     |  |              |  |              |
| APPROVED                 |            | SIZE                                |  | DWG NO       |  | REV          |
| INFO                     |            |                                     |  | phantom_main |  |              |
|                          |            | SCALE                               |  |              |  | SHEET 1 OF 1 |

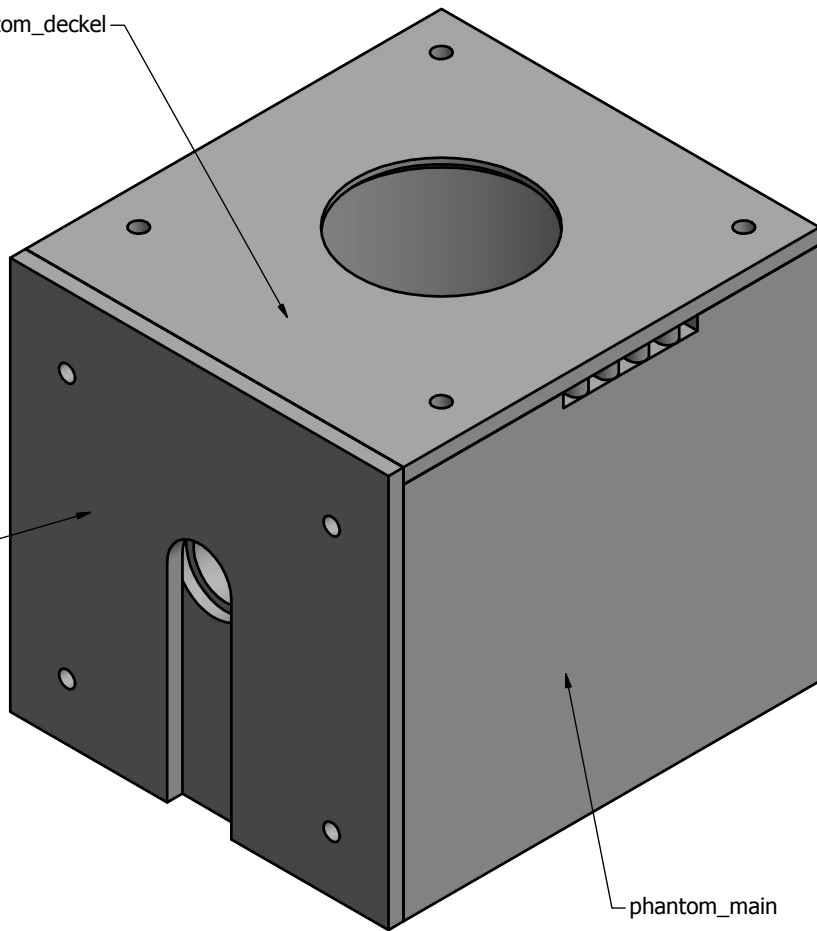
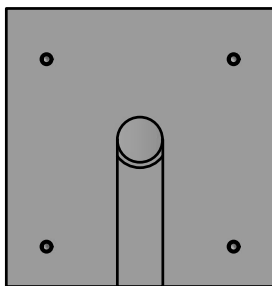
6 1 5 4 3 2 1



|                          |            |                                     |        |     |
|--------------------------|------------|-------------------------------------|--------|-----|
| DRAWN<br>Florian Weidner | 27.08.2014 | Info: Alle scharfen Kanten brechen. |        |     |
| CHECKED                  |            | TITLE                               |        |     |
| QA                       |            | Deckel für Phantom                  |        |     |
| MFG                      |            |                                     |        |     |
| APPROVED                 |            |                                     |        |     |
| INFO                     |            | SIZE                                | DWG NO | REV |
|                          |            | phantom_deckel                      |        |     |
|                          |            | SCALE                               |        |     |
|                          |            | SHEET 1 OF 1                        |        |     |



|          |                 |            |                                     |        |     |
|----------|-----------------|------------|-------------------------------------|--------|-----|
| DRAWN    | Florian Weidner | 27.08.2014 | Info: Alle scharfen Kanten brechen. |        |     |
| CHECKED  |                 |            |                                     |        |     |
| QA       |                 |            | TITLE                               |        |     |
| MFG      |                 |            | Seitenteil für Phantom              |        |     |
| APPROVED |                 |            |                                     |        |     |
| INFO     |                 |            | SIZE                                | DWG NO | REV |
|          |                 |            | phantom_seite                       |        |     |
|          |                 |            | SCALE                               |        |     |
|          |                 |            | SHEET 1 OF 1                        |        |     |



|          |                 |            |         |        |              |
|----------|-----------------|------------|---------|--------|--------------|
| DRAWN    | Florian Weidner | 02.09.2014 |         |        |              |
| CHECKED  |                 |            |         |        |              |
| QA       |                 |            | TITLE   |        |              |
| MFG      |                 |            | Phantom |        |              |
| APPROVED |                 |            | SIZE    | DWG NO | REV          |
|          |                 |            |         |        |              |
|          |                 | SCALE      |         |        | SHEET 1 OF 1 |



## Bibliography

- [AIP<sup>+</sup>06] Hasan Ayaz, Meltem Izzetoglu, Steven M Platek, Scott Bunce, Kurtulus Izzetoglu, Kambiz Pourrezaei, and Banu Onaral. Registering fNIR data to brain surface image using MRI templates. *Annual International Conference of the IEEE Engineering in Medicine and Biology - Proceedings*, 1:2671–4, January 2006.
- [BL06] Rick S. Blum and Zheng Liu, editors. *Multi-Sensor Image Fusion and Its Application*. CRC Press, Boca Raton, FL, 2006.
- [Bol84] Ludwig Boltzmann. Ableitung des Stefan'schen Gesetzes, betreffend die Abhangigkeit der Warmestrahlung von der Temperatur aus der electromagnetischen Lichttheorie. *Annalen der Physik*, 258(6):291–294, 1884.
- [BYTM97] Richard D. Bucholz, David D. Yeh, Jason Trobaugh, and Leslie L. Mcdurmont. The Correction of Stereotactic Inaccuracy Caused by Brain Shift Using an Intraoperative Ultrasound Device. In Ralph Troccaz, Jocelyne and Grimson, Eric and Mosges, editor, *CVRMed-MRCAS'97*, pages 459–466. Springer Berlin Heidelberg, 1997.
- [Can86] J Canny. A computational approach to edge detection. *IEEE transactions on pattern analysis and machine intelligence*, 8(6):679–98, June 1986.
- [Cat74] Edwin Earl Catmull. *A subdivision algorithm for computer display of curved surfaces*. Dissertation, University of Utah, 1974.
- [CCC10] Christophe Collet, Jocelyn Chanussot, and Kacem Chehdi, editors. *Multivariate Image Processing*. ISTE Ltd. and John Wiley & Sons, Inc., London, 2010.
- [CHG<sup>+</sup>10] Sean Jy-Shyang Chen, Pierre Hellier, Jean-Yves Gauvrit, Maud Marchal, Xavier Morandi, and D Louis Collins. An anthropomorphic polyvinyl alcohol triple-modality brain phantom based on Colin27. *Lecture Notes in Computer Science (including subseries Lecture Notes in Artificial Intelligence and Lecture Notes in Bioinformatics)*, 13(Pt 2):92–100, January 2010.
- [Co.14] SKS Sibley Co. El Segundo, CA, USA, 2014.

- [CPF14] Fabrizio Cutolo, Paolo Domenico Parchi, and Vincenzo Ferrari. Video See Through AR Head-Mounted Display for Medical Procedures. *Mixed and Augmented Reality (ISMAR), 2014 IEEE International Symposium on*, (September):393–396, 2014.
- [CY88] Leon O. Chua and Lin Yang. Cellular Neural Networks - Theory. *IEEE Transaction on Circuits and Systems*, 35(10), 1988.
- [DAV<sup>+</sup>98] N. L. Dorward, O. Alberti, B. Velani, F. A. Gerritsen, W. F. Harkness, N. D. Kitchen, and D. G. Thomas. Postimaging brain distortion: magnitude, correlates, and impact on neuronavigation. *Journal of neurosurgery*, 88(4):656–62, April 1998.
- [Dav12] E. R. Davies. *Computer & Machine Vision: Theory, Algorithms & Practicalities*. Elsevier Inc., fourth edition, 2012.
- [DF08] Wolfgang Drexler and James G. Fujimoto, editors. *Optical Coherence Tomography. Biological and Medical Physics, Biomedical Engineering*. Springer Berlin Heidelberg, Berlin, Heidelberg, 2008.
- [DK82] Pierre A. Devyver and Josef Kittler. *Pattern Recognition: A Statistical Approach*. Prentice-Hall, 1982.
- [DTSM06] Prashanth Dumpuri, Reid C. Thompson, Tuhin K. Sinha, and Michael I. Miga. Automated Brain Shift Correction Using A Pre-computed Deformation Atlas. *Progress in biomedical optics and imaging*, 7(27):61411F–61411F–8, March 2006.
- [Dub09] Elan Dubrofsky. Homography Estimation. (March):32, 2009.
- [Ec12] Muhammed Elmaoğlu and Azim Çelik. *MRI Handbook*. Springer, 2012.
- [FG06] Laliberte France and Langis Gagnon. Studies on Registration and Fusion of Retinal Images. In Rick S. Blum and Zheng Liu, editors, *Multi-Sensor Image Fusion and Its Application*, chapter 3, pages 57–106. CRC Press, Boca Raton, FL, 1 edition, 2006.
- [FMS14] Reports on Biomedical Engineering 2014. Prof. Hagen Malberg, 2014.
- [FSTL05] W. Gordon Frankle, Mark Slifstein, Peter S. Talbot, and Marc Laruelle. A review on brain-imaging applications of SPECT. *International review of neurobiology*, 67:385–440, January 2005.
- [GHK<sup>+</sup>03] Alexander M. Gorbach, John Heiss, Conrad Kufta, Susumo Sato, Paul Fedio, William A. Kammerer, Jeffrey Solomon, and Edward H. Oldfield. Intraoperative infrared functional imaging of human brain. *Annals of neurology*, 54(3):297–309, September 2003.
- [GHKO04] Alexander M Gorbach, John D Heiss, Leonid Kopylev, and Edward H Oldfield. Intraoper-

- ative infrared imaging of brain tumors. *Journal of neurosurgery*, 101(6):960–9, December 2004.
- [GIK03] Abdul Ghafoor, R. N. Iqbal, and S. A. Khan. Modified chamfer matching algorithm. *Intelligent Data Engineering and Automated Learning*, pages 1102–1106, 2003.
- [Gos05] A. A. Goshtasby. *2-D And 3-D Image Registration for Medical, Remote Sensing, and Industrial Applications*. John Wiley & Sons, Inc., Hoboken, New Jersey, 1 edition, 2005.
- [Gos12] A. A. Goshtasby. *Image Registration - Principles, Tools and Methods*. Springer-Verlag, London, xviii edition, 2012.
- [HHC<sup>+</sup>98] Colin J. Holmes, Rick Hoge, Louis Collins, Roger Woods, Arthur W. Toga, and Alan C. Evans. Enhancement of MR Images Using Registration for Signal Averaging. *Journal of Computer Assisted Tomography*, 22(2):324–333, 1998.
- [HHP87] Richard W. Homan, John Herman, and Phillip Purdy. Cerebral location of international 10–20 system electrode placement. *Electroencephalography and clinical neurophysiology*, 66(4):376–382, 1987.
- [HHS<sup>+</sup>14] Nico Hoffmann, Julia Hollmach, Christian Schnabel, Yordan Radev, Matthias Kirsch, Uwe Petersohn, Edmund Koch, and Gerald Steiner. Image Analysis and Recognition. 8815:411–420, 2014.
- [HMM<sup>+</sup>98] D. L. Hill, C. R. Maurer, R. J. Maciunas, J. A. Barwise, J. M. Fitzpatrick, and M. Y. Wang. Measurement of intraoperative brain surface deformation under a craniotomy. *Neurosurgery*, 43(3):514–26; discussion 527–8, September 1998.
- [Hou62] Paul V. C. Hough. A method and means for recognizing complex patterns, 1962.
- [HS88] C. Harris and M. Stephens. A Combined Corner and Edge Detector. *Proceedings of the Alvey Vision Conference 1988*, pages 23.1–23.6, 1988.
- [HS93] Paul Haeblerli and Mark Segal. Texture mapping as a fundamental drawing primitive. *Fourth Eurographics Workshop on Rendering*, pages 1–12, 1993.
- [HSH<sup>+</sup>14] Julia Hollmach, Christian Schnabel, Nico Hoffmann, Yordan Radev, Stephan Sobottka, Matthias Kirsch, Gabriele Schackert, Edmund Koch, and Gerald Steiner. Intraoperative imaging of cortical perfusion by time-resolved thermography using cold bolus approach. *Medical Imaging 2014: Image-Guided Procedures, Robotic Interventions, and Modeling*, 9036:903627, March 2014.
- [Hsi09] Jiang Hsieh. *Computed Tomography, Second Edition*. SPIE, 1000 20th Street, Bellingham,

WA 98227-0010 USA, October 2009.

- [HZ03] R. Hartley and A. Zisserman. *Multiple view geometry in computer vision*. Cambridge University Press, New York, 2nd edition, 2003.
- [IBH11] Nicusor Iftimia, William R. Brugge, and Daniel X. Hammer, editors. *Advances in Optical Imaging for Clinical Medicine*. John Wiley & Sons, Inc., Hoboken, NJ, USA, January 2011.
- [JGM06] Pierre Jannin, Christophe Grova, and Calvin R. Maurer. Model for defining and reporting reference-based validation protocols in medical image processing. *International Journal of Computer Assisted Radiology and Surgery*, 1(2):63–73, July 2006.
- [KAA<sup>+</sup>09] Arno Klein, Jesper Andersson, Babak A. Ardekani, John Ashburner, Brian Avants, Ming-Chang Chiang, Gary E Christensen, D Louis Collins, James Gee, Pierre Hellier, Joo Hyun Song, Mark Jenkinson, Claude Lepage, Daniel Rueckert, Paul Thompson, Tom Vercauteren, Roger P. Woods, John J. Mann, and Ramin V. Parsey. Evaluation of 14 nonlinear deformation algorithms applied to human brain MRI registration. *NeuroImage*, 46(3):786–802, July 2009.
- [Kac14] M Kaczmarek. Integration of thermographic data with the 3D object model. *The 12th International conference on Quantitative InfraRed Thermography (QIRT 2014)*, 2014.
- [KT09] Sergios Koutroumbas and Konstantinos Theodoridis. *Pattern Recognition (Fourth Edition)*. Academic Press, Boston, 2009.
- [KvD87] J. J. Koenderink and A. J. van Doorn. Representation of local geometry in the visual system. *Biological cybernetics*, 36:2375, 1987.
- [KWT88] M. Kass, A. Witkin, and D. Terzopoulos. Snakes: Active contour models. *International journal of computer vision*, 1988.
- [KYY<sup>+</sup>09] Babak Kateb, Vicky Yamamoto, Cheng Yu, Warren Grundfest, and John Peter Gruen. Infrared thermal imaging: a review of the literature and case report. *NeuroImage*, 47 Suppl:T154–62, August 2009.
- [LH95] Charles L. Lawson and Richard J. Hanson. *Solving Least Squares Problems*. Society for Industrial and Applied Mathematics, January 1995.
- [Low99] D.G. Lowe. Object recognition from local scale-invariant features. *Proceedings of the Seventh IEEE International Conference on Computer Vision*, pages 1150–1157 vol.2, 1999.
- [MA13] V. R. S. Mani and S. Arivazhagan. Survey of Medical Image Registration. *Journal of*

- Biomedical Engineering and Technology*, 1(2):8–25, 2013.
- [MH80] D. Marr and E. Hildreth. Theory of edge detection. *Proceedings of the Royal Society of London. Series B, Containing papers of a Biological character. Royal Society (Great Britain)*, 207(1167):187–217, February 1980.
- [MML<sup>+</sup>11] Uroš Mitrović, Primož Markelj, Boštjan Likar, Zoran Milošević, and Franjo Pernuš. Gradient-based 3D-2D registration of cerebral angiograms. *Proc. SPIE*, 7962(0):79621P–79621P–8, March 2011.
- [Mod04] Jan Modersitzki. *Numerical Methods For Image Registration*. Oxford University Press Inc., New York, 1 edition, 2004.
- [Moo08] Theo Moons. 3D Reconstruction from Multiple Images Part 1: Principles. *Foundations and Trends® in Computer Graphics and Vision*, 4(4):287–404, 2008.
- [MTLP12] P. Markelj, D. Tomažević, B. Likar, and F. Pernuš. A review of 3D/2D registration methods for image-guided interventions. *Medical image analysis*, 16(3):642–61, April 2012.
- [MV98] J. B. Antoine Maintz and Max A. Viergever. A survey of medical image registration. *Medical Image Analysis*, 2(1):1–36, 1998.
- [NA12] M. Nixon and A S. Aguado. *Feature extraction & image processing for computer vision*. Elsevier Ltd., 3 edition, 2012.
- [OKT94] H. Okudera, S. Kobayashi, and T. Toriyama. Intraoperative regional and functional thermography during resection of cerebral arteriovenous malformation. *Neurosurgery*, 36(4):1065–1067, 1994.
- [OT12] Beata Oswald-Tranta. Fusion of geometric and thermographic data for automated defect detection. *Journal of Electronic Imaging*, 21(2):021108, May 2012.
- [PC14] Bernhard Preim and Botha Charl, editors. *Visual Computing for Medicine*. Morgan Kaufmann Publishers Inc., Boston, 2nd edition, 2014.
- [PIK92] J. Princen, J. Illingworth, and J. Kittler. A Formal Definition of the Hough Transform : Properties and Relationships. *Journal of Mathematical Imaging and Vision*, 1(2):153–168, July 1992.
- [PP14] Brian W Pogue and Michael S Patterson. Review of tissue simulating phantoms for optical spectroscopy, imaging and dosimetry. *Journal of biomedical optics*, 11(4):041102, 2014.
- [PR92] Richard J Prokop and Anthony P Reeves. A survey of moment-based techniques for unoccluded object representation and recognition. *CVGIP: Graphical Models and Image Processing*, 54(3):209–234, September 1992.

- Processing*, 54(5):438–460, September 1992.
- [RA12] E. F. J. Ring and K. Ammer. Infrared thermal imaging in medicine. *Physiological measurement*, 33(3):R33–46, March 2012.
- [RC06] I. Reinertsen and D. L. Collins. A realistic phantom for brain-shift simulations. *Medical Physics*, 33(9):3234, 2006.
- [Red14] RedEye. TangoPlus, 2014.
- [RKY13] Q. R. Razlighi, N. Kehtarnavaz, and S. Yousefi. Evaluating Similarity Measures for Brain Image Registration. *Journal of visual communication and image representation*, 24(7):977–987, October 2013.
- [RL01] Szymon Rusinkiewicz and M. Levoy. Efficient variants of the ICP algorithm. In *Proceedings Third International Conference on 3-D Digital Imaging and Modeling*, pages 145–152. IEEE Comput. Soc, 2001.
- [RNK<sup>+</sup>04] M. H. T. Reinges, H.-H. Nguyen, T. Krings, B.-O. Hütter, V. Rohde, and J. M. Gilsbach. Course of brain shift during microsurgical resection of supratentorial cerebral lesions: limits of conventional neuronavigation. *Acta neurochirurgica*, 146(4):369–77; discussion 377, April 2004.
- [Rui10] D. S. A. Ruijters. *Multi-modal image fusion during minimally invasive treatment*. Dissertation, Technische Universiteit Eindhoven, 2010.
- [Sch06] Otmar Scherzer, editor. *Mathematical Models for Registration and Applications to Medical Imaging*, volume 10 of *Mathematics in industry*. Springer Berlin Heidelberg, Berlin, Heidelberg, 2006.
- [SDP13] Aristeidis Sotiras, Christos Davatzikos, and Nikos Paragios. Deformable medical image registration: a survey. *IEEE transactions on medical imaging*, 32(7):1153–90, July 2013.
- [SGS<sup>+</sup>13] Ionildo José Sanches, Humberto Remigio Gamba, Mauren Abreu De Souza, Eduardo Borba Neves, and Percy Nohama. Artigo Original Fusão 3D de imagens de MRI / CT e termografia. *Revista Brasileira de Engenharia Biomedica (2013)*, 29:298–308, 2013.
- [SKS13] James Shackleford, Nagarajan Kandasamy, and Gregory Sharp. *High-Performance Deformable Image Registration For Manycore Processors*. Morgan Kaufmann Publishers Inc., San Francisco, CA, USA, 1 edition, 2013.
- [SM00] Heidrun Schumann and Wolfgang Müller. *Visualisierung: Grundlagen und allgemeine Methoden*. Springer-Verlag, Berlin Heidelberg New York, 2000.

- [SO08] P. Schalk and P. O’Leary. Measuring and analyzing cross-sectional profiles of rotating objects using light sectioning. *IEEE Transactions on Instrumentation and Measurements*, 57(10):2329–2338, October 2008.
- [Sob70] Irwin Edward Sobel. *Camera Models and Machine Perception*. PhD thesis, Stanford University, 1970.
- [SSN07] Ashutosh Saxena, Jamie Schulte, and AY Ng. Depth Estimation Using Monocular and Stereo Cues. *IJCAI*, 2007.
- [SSS14] Jasjit S. Suri, S. Kamaledin Setarehdan, and Sameer Singh, editors. *Diagnostic Ultrasound Imaging: Inside Out*. Elsevier, London, 2014.
- [Ste79] J. Stefan. Über die Beziehung zwischen der Wärmestrahlung und der Temperatur. *Sitzungsberichte der mathematisch-naturwissenschaftlichen Classe der kaiserlichen Akademie der Wissenschaften*, 79:391–428, 1879.
- [SUS<sup>+</sup>06] O. Sergeeva, F. Uhlemann, G. Schackert, C. Hergeth, U. Morgenstern, and R. Steinmeier. Integration of intraoperative 3D-ultrasound in a commercial navigation system. *Zentralblatt für Neurochirurgie*, 67(4):197–203, November 2006.
- [Sze06] Richard Szeliski. Image Alignment and Stitching: A Tutorial. *Foundations and Trends® in Computer Graphics and Vision*, 2(1):1–104, 2006.
- [TDAJ06] Sovira Tan, Jason Dale, Andrew Anderson, and Alan Johnston. Inverse perspective mapping and optic flow: A calibration method and a quantitative analysis. *Image and Vision Computing*, 24(2):153–165, February 2006.
- [tFSV94] Bart M. ter Haar Romeny, Luc M. J. Florack, Alfons H. Salden, and Max A. Viergever. Higher order differential structure of images. *Image and Vision Computing*, 12(6):317–325, July 1994.
- [THMR13] Michael W. Tao, Sunil Hadap, Jitendra Malik, and Ravi Ramamoorthi. Depth from Combining Defocus and Correspondence Using Light-Field Cameras. *IEEE International Conference on Computer Vision*, 2:673–680, December 2013.
- [Tsa86] R. Y. Tsai. An efficient and accurate camera calibration technique for 3D Machine Vision. *Proc. IEEE Conf. on Computer Vision and Pattern Recognition*, 1986.
- [UK14] Cancer Research UK. Brain, other CNS and intracranial tumours incidence statistics - Cancer Research UK, 2014.
- [VAA14] B. Verney, M. Akhloufi, and O. Aubreton. Multimodal fusion system for NDT and Metrol-

- ogy. *The 12th International conference on Quantitative InfraRed Thermography (QIRT 2014)*, 2014.
- [VBO12] Alvaro Valencia, Benjamin Blas, and Jaime H. Ortega. Modeling of Brain Shift Phenomenon for Different Craniotomies and Solid Models. *Journal of Applied Mathematics*, 2012:1–20, 2012.
- [WKM<sup>+</sup>09] Stefan Wagner, Julia Kuss, Tobias Meyer, Matthias Kirsch, and Ute Morgenstern. An integrated tool for automated visualization of subdural electrodes in epilepsy surgery evaluation. *International journal of computer assisted radiology and surgery*, 4(6):609–16, November 2009.
- [Wol94] George Wolberg. *Digital Image Warping*. IEEE Computer Society Press, Los Alamitos, CA, USA, 1st edition, 1994.
- [Yui91] A. L. Yuille. Deformable templates for face recognition. *Journal of cognitive neuroscience*, 3(1):59–70, January 1991.

## List of Figures

|      |  |    |
|------|--|----|
| 2.1  | Illustration of the nuclear spin showing protons aligned parallel and anti-parallel to a magnetic field . . . . .  | 6  |
| 2.2  | Illustration of the spin-lattice relaxation. 2.2a: Spin after the tilting impulse. 2.2b, 2.2c and 2.2d: magnetization in the original state . . . . .                  | 6  |
| 2.3  | Illustration of the spin-spin relaxation. 2.3a: Spin before the tilting impulse. 2.3b: spin after the tilting impulse. 2.3c: de-phasing 2.3d: re-phased spin . . . . . | 7  |
| 2.4  | Electromagnetic spectrum with outlined infrared spectra . . . . .  | 8  |
| 2.5  | Neuronavigation system <i>BrainLab VectorVision</i> showing the computer, the view screen and the infrared cameras . . . . .   | 10 |
| 2.6  | Pointer . . . . .  | 11 |
| 2.7  | Instrument adapter . . . . .   | 11 |
| 2.8  | Fiducial marker . . . . .  | 11 |
| 2.9  | InfraTec <i>VarioCAM HD head 680 S / 30mm ***MEDICAL ***</i> . . . . .   | 11 |
| 2.10 | Thermographic camera (A) with the attached IA (B) . . . . .  | 12 |
| 2.11 | Screenshot of the Amira user interface showing a mesh with three modules and one connection . . . . .  | 13 |
| 3.1  | Imaging Phantom by Chen et al. [CHG <sup>+</sup> 10] . . . . .   | 16 |
| 3.2  | Imaging Phantom by Reinertsen et al. [RC06] . . . . .  | 16 |
| 3.3  | Basic steps during image fusion . . . . .  | 17 |
| 3.4  | Features based on pixel intensities . . . . .  | 18 |
| 3.5  | Features based on shapes . . . . .   | 20 |
| 3.6  | Taxonomy of medical image registration according to Maintz et al. [MV98] . . . . .   | 24 |
| 3.7  | Pipeline of image registration using features . . . . .  | 27 |
| 3.8  | Calibration-based image registration . . . . .   | 29 |
| 3.9  | Coordinate system with two objects $I_m$ and $I_{ref}$ in the world coordinate system $cs_w$ . . . . .   | 30 |
| 3.10 | Comparison of both camera models. Using the projective model, the size of the objects $x$ on the projection plane depends on the focal length $f$ . . . . .            | 33 |

---

|      |  |    |
|------|--|----|
| 3.11 | Rays, starting at the eye, going through pixels of an image and hitting an object or not. . . . .  | 34 |
| 3.12 | Texture mapping described for one face of a tetrahedron . . . . .  | 35 |
| 3.13 | Example for lens distortion. The lens distorts the square object slightly . . . . .  | 35 |
| 3.14 | 3D model of a workpiece with thermographic data ([OT12]) . . . . .   | 37 |
| 3.15 | Features of the workpiece ([OT12]) . . . . .   | 37 |
| 3.16 | Results of Kaczmarek. Left: 3D mesh model. Right: 3D mesh model with merged thermographic data ([Kac14]) . . . . .   | 38 |
| 3.17 | Different steps during image fusion developed by Ayaz et al. [AIP <sup>+</sup> 06] . . . . .   | 39 |
| 3.18 | Images showing the image fusion of Sanches et al. [SGS <sup>+</sup> 13] . . . . .  | 39 |
| 4.1  | Early design of the imaging phantom . . . . .  | 44 |
| 4.2  | Prototype of the imaging phantom . . . . .   | 44 |
| 4.3  | Sketch of the final imaging phantom . . . . .  | 44 |
| 4.4  | Final imaging phantom with connected syringes . . . . .  | 46 |
| 4.5  | Top view with removed lid and tube visible . . . . .   | 46 |
| 4.6  | MR image of the imaging phantom: T2-weighted (left: default. Right: inflated) . . . . .  | 46 |
| 4.7  | MR image of the imaging phantom: MP-RAGE (left: default. Right: inflated) . . . . .  | 46 |
| 4.8  | MR image of the imaging phantom: FLAIR (left: default. Right: inflated) . . . . .  | 46 |
| 4.9  | Infrared image of the imaging phantom with fiducial markers (black) and tube (yellow) visible . . . . .  | 47 |
| 4.10 | Schematic view for intraoperative image fusion. A: neuronavigation system. B: imaging phantom with fiducial markers. C: instrument adapter. D: infrared camera. E: notebook running Amira and receiving tracking and image data. . . . . | 48 |
| 4.11 | Component diagram of the plug-in . . . . .   | 49 |
| 4.12 | Class diagram of one component (VectorVision or InfraTec) . . . . .  | 50 |
| 4.13 | Simplified sequence diagram showing the life-cycle of the image fusion plug-in . . . . .   | 51 |
| 4.14 | Messages during image fusion . . . . .   | 51 |
| 4.15 | Classification of the presented registration scheme according to the taxonomy introduced in section 3.2.2.1 . . . . .  | 53 |
| 4.16 | Amira screenshot with unmodified data object: 3D image of the phantom, the 2D infrared image and the world coordinate system . . . . .   | 54 |
| 4.17 | Necessary devices for the calibration of the instrument adapter. . . . .   | 54 |
| 4.18 | Spatial difference between IA and camera. . . . .  | 55 |
| 4.19 | The indicated point pairs are touched with the pointer and their coordinates are used to assess the orientation of the infrared camera. . . . .  | 56 |

|   |    |
|---|----|
| 4.20 Correlation between focus value <i>FE</i> and distance $f(FE)$ for the InfraTec <i>VarioCAM HD head 680 S / 30mm ***MEDICAL***</i> . . . . .   | 57 |
| 4.21 Amira view with modified data objects (image of the phantom, transformed 2D infrared image and coordinate system) indicating the result of the registration . . . . .  | 59 |
| 4.22 Colourmap applied to the incoming data: heated object scale . . . . .  | 60 |
| 4.23 Different visualization types provided by Amira. 4.23a: <i>Voltex</i> . 4.23b: <i>Volren</i> . 4.23c: <i>Isosurface</i> . 4.23d: <i>SurfaceView</i> . . . . .  | 62 |
| 4.24 Image fusion with the provided visualization and fusion techniques. 4.24a: <i>Isosurface</i> with an attached Colorfield. 4.24b: <i>Isosurface</i> with texture. 4.24c: <i>Isosurface</i> with texture and additional <i>Voltex</i> . 4.24d: <i>SurfaceView</i> with texture and <i>Isosurface</i> . . . . . | 64 |
| 4.25 Amira mesh showing the necessary elements for image fusion: ThermoData, BrainData, <i>Isosurface</i> , <i>SurfaceView</i> and <i>ImageFusion</i> with the necessary connections. . . . .   | 64 |
| 4.26 Tip of the pointer represented by a sphere. . . . .  | 66 |
| 4.27 Tab <i>ImageFusion</i> with control elements . . . . .   | 69 |
| 4.28 Tab <i>Calibration</i> with control elements . . . . .   | 70 |
| 4.29 Tab <i>Thermography</i> with control elements . . . . .  | 71 |
| 4.30 Tab <i>Neuronavigation</i> with control elements . . . . .   | 71 |
| 4.31 Tab <i>Evaluation</i> with control elements . . . . .  | 72 |
| 4.32 Tab <i>Options</i> with control elements . . . . .   | 72 |
| 5.1 Three images showing the position of the pointer's tip for three different registrations. . . . .   | 79 |
| 5.2 Special-purpose body part without (5.2a) and with (5.2b) instrument adapter attached . . . . .  | 80 |
| 5.3 Alternative to the current IA and body part. . . . .  | 81 |
| 5.4 Image fusion result using a camera angle of $0^\circ$ . . . . .   | 83 |
| 5.5 Image fusion result using a camera angle of $30^\circ$ . . . . .  | 84 |
| 5.6 Image fusion result using a camera angle of $60^\circ$ . . . . .  | 85 |



## List of Tables

|     |   |    |
|-----|---|----|
| 3.1 | Natures of the Transformation . . . . .   | 25 |
| 5.1 | Maximum error of the MR model . . . . .   | 78 |
| 5.2 | Mean error and standard deviation of the registration error introduced by <i>VectorVision cranial 2.1.1</i> and <i>iPlanNet 3.0</i> . . . . . | 79 |
| 5.3 | Axial and angular error introduced by the calibration of the instrument adapter. . . . .  | 80 |
| 5.4 | Standard deviation of the orientation and position of the IA when attaching the instrument adapter. . . . .                                   | 80 |
| 5.5 | Error in the final image resulting from attaching the instrument adapter. . . . .   | 81 |
| 5.6 | Mean error and standard deviation for a camera angle of 0° . . . . .  | 83 |
| 5.7 | Mean error and standard deviation for a camera angle of 30° . . . . .   | 84 |
| 5.8 | Mean error and standard deviation for a camera angle of 60° . . . . .   | 85 |
| 5.9 | Average errors for the 0°, 30° and 60° measurements with the overall average error. . . . .   | 85 |



## Acknowledgments

Apart from the efforts of myself, the success of any project depends largely on the encouragement and guidelines of many others. I am using this opportunity to express my gratitude to everyone who supported me throughout the course of this thesis. I am thankful for their aspiring guidance, invaluable constructive criticism and friendly advice during the project work. I am sincerely grateful to them for sharing their truthful and illuminating views on a number of issues related to the project.

I would like to express my special appreciation and thanks to my advisors Mr. Nico Hoffmann and Mr. Peter Urban for the useful comments, remarks and engagement through the learning process of this master thesis.

In addition, a thank you to Mr. Mirko Mehner and Mr. Christian Schnabel for their support during the development of the imaging phantom.

Furthermore, I would also like to acknowledge the role of the department of Neurosurgery at the University Hospital Carl Gustav Carus Dresden, who gave the permission to use the required equipment and the necessary materials.

I would also like to thank the department of Clinical Sensing and Monitoring at Technische Universität Dresden for the opportunity to carry out my thesis and for providing a wonderful working atmosphere.

Finally, I owe more than thanks to my family members for their encouragement throughout my life. Without their support it would have been impossible for me to finish my study seamlessly.

Live long and prosper.



## Copyright Information

**OpenIGTLink** is distributed under the new BSD License

(<http://opensource.org/licenses/bsd-license.php>, last accessed: 2014-11-28)

**Boost** is distributed under the Boost Software License, Version 1.0.

([http://www.boost.org/LICENSE\\_1\\_0.txt](http://www.boost.org/LICENSE_1_0.txt), last accessed: 2014-11-28)

**Qt** is licensed under a commercial and open source licenses (GNU General Public License version 3 and GNU Lesser General Public License version 2.1).

**Insight Visualization Toolkit (ITK)** “ITK is copyrighted by the Insight Software Consortium, a non-profit alliance of organizations and individuals interested in supporting ITK. The software is distributed as open source under an OSI-approved license. Starting with ITK 4.0, the Apache 2.0 license is used. For versions prior and including 3.20, the new and simplified BSD license is used. Before 3.6, a variation of the BSD license is used.” (<http://www.itk.org/ITK/project/license.html>, last accessed: 2014-11-28)

**Amira & OpenInventor** Copyright 1999-2014 FEI, SAS; Copyright 1995-2014, ZIB Berlin; ALL RIGHTS RESERVED. amira(R) is a registered trademark of ZIB. amira(R) is being jointly developed by Zuse Institute Berlin and FEI, SAS. Avizo® is a registered trademark of FEI, SAS. HardCopy, MeshViz, VolumeViz, TerrainViz are marks of FEI, SAS. FEI, SAS is a source licensee of OpenGL®, Open Inventor® from Silicon Graphics, Inc. OpenGL® and Open Inventor® are registered trademark of Silicon Graphics, Inc. All other products and company names are trademarks or registered trademarks of their respective companies.

